Laser-interferometric dilatometry

Vom Fachbereich Produktionstechnik
der
UNIVERSITÄT BREMEN

zur Erlangung des Grades
Doktor-Ingenieur
genehmigte

Dissertation

von
M.Eng., Ruven Spannagel

Gutachter:	Prof. Dr. rer. nat. Claus Braxmaier
	Prof. Dr.-Ing. Andreas Rittweger

Tag der mündlichen Prüfung: 04.10.2017

Zusammenfassung

Sowohl hoch dimensional stabile Materialien in erdgebundenen optischen Systemen, wie höchstgenaue optische Uhren, als auch Materialien und Strukturen mit hervorragender dimensionaler Stabilität gepaart mit geringem Gewicht für Raumfahrtanwendungen wie Teleskope, optische Bänke und optische Resonatoren, sind von hohem Interesse. Verbindungstechnologien mit höchster dimensionaler Stabilität zwischen Materialien mit unterschiedlichen thermischen Eigenschaften sind eine große Herausforderung. Glaskeramiken und Verbundmaterialien können im Herstellungsprozess so beeinflusst werden, dass ein minimaler thermischer Ausdehnungskoeffizient (CTE) bei einer spezifischen Temperatur erreicht werden kann. Die genaue Bestimmung solch geringer CTEs erfordert hochstabile Messgeräte.

In dieser Arbeit wurden Dilatometer zur Bestimmung von CTEs rohrförmiger Proben in einem Temperaturbereich von 140 K bis 333 K konstruiert, realisiert und durch Messungen an Glaskeramiken verifiziert. Durch unsere speziell konstruierten Spiegelhalter kann jegliches Material untersucht werden.

Das optische System basiert auf einem heterodynen Interferometer mit einer Auflösung im sub-nanometer Bereich zur Messung der Probenexpansion, welche durch eine kontrollierte Temperaturänderungen herbeigeführt wird. Eine Probe aus kohlenstofffaserverstärktem Kunststoff (CFRP) wurde von 140 K bis 250 K im Bereich von $10^{-8}\,\mathrm{K}^{-1}$ mit einer detaillierten Analyse der Messunsicherheit charakterisiert.

Das verifizierte Dilatometer wurde an eine Thermalkammer für die CTE-Bestimmung von größeren Strukturen angepasst und eine 0.5 m lange CFRP Struktur mit Zerodur Endfittings vermessen. Dabei wurden repräsentative Verbindungstechnologien als Technologiedemonstration für die Satellitenmission GRACE Follow-On bei 302 K untersucht.

Abstract

Highly dimensionally stable materials and structures are particularly needed in optical systems such as ultra precise optical clocks, as well as materials with excellent dimensional stability and light weight properties for space applications such as telescopes, optical benches, and optical resonators. Also, the dimensional stability of mounting technologies of materials with different properties is of high interest for such applications. Glass ceramics and composite materials can be tuned to reach a very low coefficient of thermal expansion (CTE) at different temperatures, enabling best stability in the operating temperature for certain applications. In order to determine the CTE of such highly stable materials, very accurate set-ups are needed.

In this thesis, metrology set-ups to measure the CTE of a large variety of material samples are designed, realized and verified, measuring dimensionally stable glass ceramics. The set-ups are able to characterize tube shaped samples at a temperature range of 140 K to 333 K. Due to our unique mirror mount design all kind of materials can be characterized.

The optical dilatometer set-ups are based on a heterodyne interferometer with a displacement sensitivity at the sub-nanometer level. This instrument is used to measure the expansion of a sample when applying controlled small amplitude temperature signals. A carbon fiber reinforced polymer (CFRP) sample was characterized where CTE levels of $10^{-8}\,\mathrm{K}^{-1}$ from 140 K to 250 K were measured and a detailed uncertainty analysis was performed.

The verified metrology set-up for tube shaped samples was adapted for CTE measurements of larger structures. Therefore, a large thermal chamber was set up and a 0.5 m CFRP spacer with Zerodur endfittings as a representative joint technology demonstrator for the GRACE Follow-On space mission at 302 K was investigated.

Contents

1. Introduction

In all kind of applications and increasingly in space based instruments, materials with special characteristics are needed. There is no ideal material that meets every need, e.g. light weight, dimensional stability, thermal lifetime (aging), strength or stiffness, costs, outgassing properties and magnetic moments. For each application, an adequate trade-off of possible materials has to be considered. For space applications, there is an increasing need of materials with light weight characteristics to reduce launch costs, that also provide dimensional and thermal stability to enable precise measurements. A major goal for researchers is to utilize light weight and dimensionally stable materials, particularly for earth observation and scientific space missions. While the field of material research continuous to be highly dynamic, precise characterization of dimensionally stable materials remain challenging. The objective of this doctoral thesis is to address some of these challenges related to the precise measurement of low coefficient of thermal expansion (CTE).

1.1. Relevance of dimensional stability

Optical instruments for space based applications are often limited by the dimensional stability of their materials. Current and future missions require, among others, telescopes, optical benches, optical resonators. exhibiting dimensional and thermal properties resulting in nanometer and picometer range stabilities. Consequently, highly thermally stable environments together with low CTE and light weight materials are needed.

One example is the proposed scientific space mission LISA (Laser Interferometer Space Antenna) [1], which is a gravitational wave observatory and consists of three spacecraft separated by approximately $3 \cdot 10^6$ km, flying in a equilateral triangle formation, following the earth, in a heliocentric orbit. This mission is one of the most challenging space missions, with regard to its technical challenges: its telescope and optical benches must exhibit picometer stability over thousands of seconds. In addition, the absolute temperature ranges are predicted to be from 203 K [2, 3] for the telescope to 300 K for the optical bench [4].

Another space mission of interest with the aim to measure the gravitational field of the earth and its fluctuations is called GRACE (Gravity Recovery and Climate Experiment). The second generation of this mission, GRACE Follow-On (to be launched in 2018) includes a laser ranging instrument (LRI) as a technological demonstrator [5] to measure optically the distance change between two spacecraft. A key subsystem for the LRI is a large retroreflector that must be stable to the nanometer level in the milli-Hertz observation bandwidth [6].

Highly stable optical resonators are also key for future tests of fundamental physics like, BOOST [7, 8], a proposed Kennedy-Thorndike experiment in space. In this proposed mission, the frequency changes of two different clocks, a resonator where the frequency is depending on the speed of light (c), and an atom clock where the frequency depends on molecular transition, will be compared to test the velocity dependance of c as a postulate of the special relativity. Due to the higher velocity and higher velocity changes of the satellite compared to ground based laboratories a significant improvement of the science case is expected. [9]

The above mentioned missions are just a few examples for many satellite missions where precise measurements, and therefore highly stable materials are needed to reach the mission goal. The predictions of the stability of structures combining two or more different materials assembled together is very challenging and tests of their dimensional stability behavior are crucial.

Also experiments in laboratories have the need of dimensionally stable materials. Optical benches, resonators [10] or ground based telescopes [11] can achieve ultra high accuracy when such materials are used, in order to test fundamental physics like special or general relativity [12].

1.2. Dimensional stability and coefficient of thermal expansion

The dimensional stability in materials can change due to variations in stress, temperature (coefficient of thermal expansion), absorbed moisture (CME, coefficient of moisture expansion), aging (e.g. relaxation process in glass ceramics), or radiation.

In this thesis, dedicated test facilities were built to accurately measure the coefficient of thermal expansion (CTE) of thermally stable samples and structures. Radiation, aging and stress were not addressed in these investigations. Moisture release, on the contrary, has been observed with our measurement system. However, these observations are more time intensive than a CTE measurement, and become evident as an exponential trend during evacuation. Dedicated investigations for these effects were not within the scope of this thesis.

Instruments to determine the CTE are also called dilatometers. To determine the CTE of a material, the expansion of a sample has to be measured as a function of temperature and its dimensions. The linear CTE is the thermal expansion in one dimension and is defined as [13]

$$\alpha(T) = \frac{1}{\ell(T)}\frac{d\ell}{dT} \simeq \frac{1}{\ell(T)}\frac{\Delta\ell}{\Delta T}, \tag{1.1}$$

where ℓ and T are the length and temperature of the sample, respectively. The derivatives can be approximated by differences for small temperature ranges in linear CTEs. From Equation (1.1) it is clear that an accurate CTE determination requires precise length and temperature measurements. In our case, we perform the CTE measurement at specific temperatures by measuring first the absolute length, ℓ, and secondly by measuring, $\Delta\ell/\Delta T$ modulating ΔT and observing both ΔT and $\Delta\ell$.

Another definition of the CTE is the volumetric expansion coefficient (β). For isotropic materials the volumetric CTE can be calculated as

$$\beta(T) = \frac{1}{V(T)}\frac{dV}{dT} \simeq \frac{1}{V(T)}\frac{\Delta V}{\Delta T}, \tag{1.2}$$

where V is the volume of the sample and ΔV the volumetric expansion of the sample.

In this thesis, the CTE is only determined in one dimension (α). Most materials are not isotropic and the CTE can have different values along different axes. For such materials and structures, α has to be determined in the direction of interest.

1.3. CTE measurement methods

There are different methods to determine the dimensional expansion of a sample. The most common can be categorized into two different types, mechanical and optical. In both categories, a wide variety of dilatometers have been designed such that they are able to detect length variations ($\Delta\ell$) below the micrometer level. The biggest advantage of the optical dilatometer is the non-contact property, where no significant force is applied to the sample, compared to a mechanical measurement device. These two types of dilatometers are described in more detail in the following sections.

1.3.1. Mechanical dilatometer

The push-rod dilatometer is the most common mechanical dilatometer and is based on a precise capacitance measurement that is proportional to the expansion of the sample (see Figure 1.1). The loaded push-rod is in contact with the sample and transfers the expansion or contraction to the sensor. The expansion of the push-rod is subtracted from the measurement data due to the calibration process. This measurement method is very reliable due to its very simple set-up as long as the force of the push-rod does not influence the dimensional changes of the sample [14]. Different variation of push-rod dilatometers are commercially available using captive sensors or optical encoders to reach a resolution in the nanometer range.

A similar technique to the push-rod dilatometer is a method where the sample changes the separation between capacitive sensor blades. A sample is mounted in a Fused Silica cell, such that the expanding sample pushes against

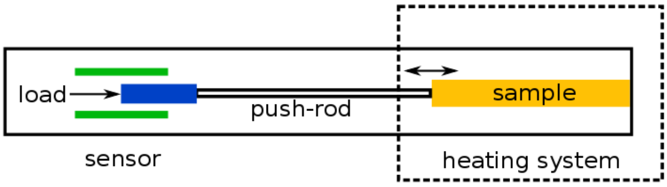

Figure 1.1.: Measurement principle of a mechanical dilatometer, called push-rod dilatometer.

two metallized capacitor plates, thus changing their separation, and providing an electrical signal proportional to the expansion. [15]

1.3.2. Optical dilatometer

An optical dilatometer uses a light beam to detect changes in one or more dimensions of a sample in a contactless way. The simplest optical dilatometer works such that the sample is mounted along an optical beam pointing on a detector. The beam is collimated to a size larger than the sample, and blocks some of the light. If the sample expands, a CCD camera detects proportionally less light and this signal is used to determine the $\Delta\ell$ of the sample. With a well calibrated system also absolute measurements can be conducted, in one or more dimensions e.g. $\ell_x \cdot \ell_y$. Such dilatometers detect dimensional changes in the sub-micrometer range and are commercially available, for example, from the company TA Instruments.

A more complex, but also more reliable optical read-out is based on laser interferometry. Here, a monochromatic light source is used to measure path-length changes of a measurement beam whose phase is compared to a reference. This optical measurement system is such that the resolution of a fraction of the wavelength of the light source in the order of nanometers or better can be obtained.

A simple interferometer design is the so called Michelson interferometer (see Figure 1.2 (i)). This homodyne interferometer splits a laser beam into two beams with the same frequency at a beam splitter (BS); a measurement beam and a reference beam are reflected off of two different mirrors (measurement

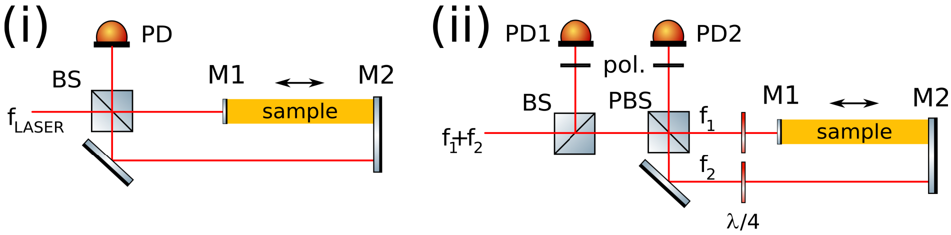

Figure 1.2.: (i) Measurement principle of a homodyne interferometer based dilatometer, (ii) a dilatometer based on a simple heterodyne interferometer. BS = beam splitter, PBS = polarization beam splitter, pol. = polarizer, PD = photodetector, $\lambda/4$ = quarter waveplate, f = frequency of the laser beam, M1 and M2 are mirrors reflecting the beam on both sides of the sample.

mirror (M1) and reference mirror (M2)) and overlapped again to generate the interference pattern. The local intensity of the interference depends on the phase difference between the two beams $\Delta\phi$. If the pathlength of the measurement beam changes with respect to the pathlength of the reference beam, a DC photodetector (PD) can measure intensity changes corresponding to the expansion of the sample. The biggest disadvantage of this method is the sensitivity of the variation to the intensity of the light source. It is not possible to discern the relevant pathlength driven intensity changes from intrinsic laser intensity noise. [16, 17, 18]

In most optical dilatometers more complex interferometers are used and they are often based on the Michelson interferometer concept to improve the measurement accuracy. A different approach is the heterodyne interferometer which enables measurements of optical pathlength changes from the phase information of a sinusoid signal down to the picometer level. One picometer is approximately 2 to 3 orders of magnitudes smaller than a Hydrogen atom. Compared to the homodyne interferometer, this method is less susceptible to DC power noise of the laser source and has a better long term stability. In Figure 1.2 (ii) a simple heterodyne interferometer is shown, where the two laser beams with different frequencies, f_1 and f_2 are superimposed with orthogonal polarization. At the beam splitter (BS) a part of the laser beam is reflected off to a detector PD1, where a polarizer with a 45° angle enables interference between the two frequencies and provides a reference heterodyne frequency, $f_{het} = |f_1 - f_2|$. At the polarization beam splitter (PBS), the superimposed frequencies are divided and reflected back of the mirrors M1 and M2, passing twice through a quarter waveplate ($\lambda/4$) where the phase of the polarized beams is changed by 90° to interfere again at the detector PD2. The two AC detectors measure phase differences of the heterodyne frequency, which is equivalent to the relative phase difference between the laser beams. If the sample expands the phase of the heterodyne frequency measured at PD2 compared to PD1 will change and a corresponding distance can be computed. [16]

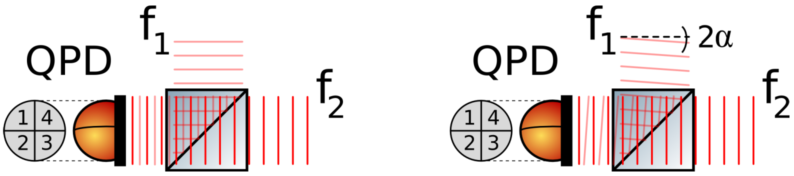

Figure 1.3.: Schematic of the differential wavefront sensing (DWS) method. Left: without tilt of the wavefront; right: tilt of the wavefront of 2α.

By using quadrant photodetectors (QPD), it is possible to compute the relative phase difference between QPD segments, thus obtaining information about the relative wavefront angle and its change. This technique is known as differential wavefront sensing (DWS) [19, 20]. With this method, noise levels in the tilt measurement of nanoradian levels can be achieved. One nanoradian corresponds to angle change when the height of a imaginary line at a distance of 1000 m changes of 1 µm. If, for example, the measurement mirror of the interferometer tilts, the wavefront of the laser beam f_1 tilts accordingly (schematic seen in Figure 1.3). After superimposing the beam with the tilted wavefront, f_1 with f_2, the tilt can be detected by split photodetectors with four segments, QPDs, and can be calculated as:

$$\phi \approx \frac{16\omega_0}{3\lambda} \cdot 2\alpha, \tag{1.3}$$

where ω_0 is the radius of the laser beam, λ the wavelength and 2α the tilt of the wavefront and respectively α the angle of the corresponding tilted mirror. [21]

A big variety of interferometer set-ups are used, e.g. Fabry-Pérot interferometer [22], Fizeau interferometer [23], where the resolution in the picometer level or higher can be achieved. In our set-up, a two-beam heterodyne interferometer is used. The motivation for using heterodyne interferometry is explained in Section 2.1.

1.4. CTE measurement facilities and achievements

Different institutes around the world focus on CTE measurements of ultra stable materials. National metrology institutes (NMI) have the goal to measure standards with the highest accuracy and reliability as the highest national authority in terms of metrology. The PTB (Physikalisch-Technische Bundesanstalt) is the NMI of Germany and achieves CTE uncertainties in the range of $2 \cdot 10^{-9}\,\mathrm{K}^{-1}$ from $7\,\mathrm{K}$ to $293\,\mathrm{K}$ using an ultra precise instrument based on a Twyman-Green interferometer that provides absolute length measurements [24, 25]. However, it requires samples with parallel end faces, capable of reflecting the laser beams.

At the National Research Laboratory of Metrology in Japan, an optical heterodyne interferometer enables measurements in a temperature range from $6\,\mathrm{K}$ to $273\,\mathrm{K}$ [26, 27] reaching uncertainties around $10^{-8}\,\mathrm{K}^{-1}$.

In Reference [28] several institutes characterized CTEs of different materials in a wide temperature range in a round robin test. Uncertainties better than $5 \cdot 10^{-8}\,\mathrm{K}^{-1}$ between $20\,\mathrm{K}$ and $300\,\mathrm{K}$ are reported. The measurement systems are Michelson interferometers (PMIC, Precision Measurement and Instruments Corporation and ATK, Alliant Techsystems Inc.), capacitance cell dilatometers (FZK, Forschungszentrum Karlsruhe) and focus distance measurement dilatometers (MELCO, Mitsubishi Electric Corporation). However, most of the set-ups require samples with polished-lapped surfaces on both sides.

The dilatometer for tube shaped samples described in this thesis overcomes these limitation and allows CTE measurements of samples with a maximum length of $120\,\mathrm{mm}$ and an inner diameter of $20\,\mathrm{mm}$. The dimensional constrains are given by the mechanical set-up. A big variety of materials can be investigated: mono crystalline materials, Silicon Carbide, glass ceramics or other composite materials like CFRP (Carbon fiber reinforced polymer).

1.5. Candidate materials for low CTE measurements

For each space mission and application, materials with special characteristics are needed. The focus here is on materials used in optical instruments with a low CTE or light weight characteristics. A list of materials with these properties is given in Table 1.1.

Table 1.1.: Selection of materials with low CTE and often used in space applications. (*) several suppliers available.

material	supplier	CTE [10^{-6} K^{-1}]	temperature range [°C]
ULE 7972	Corning	±0.01	5 – 35
Zerodur	Schott	±0.007	0 – 50
Clearceram	Ohara	±0.02	0 – 50
SiC	(*)	≈ 3.8	25
CeSiC	ECM	0 – 2.74	-250 – 120
Invar36	(*)	≈1.6	30 – 100
Titanium	(*)	≈9	20 – 100
Fused Silica	(*)	0.51	0 – 100

Materials with CTEs $< 10^{-8}$ K^{-1} are rare. Most of these materials are developed such that its minimum CTE is reached around room temperature [29]. Some manufacturers also provide materials with adjusted CTE for other temperatures, e.g. Corning and Schott.

Corning offers a Titania Silicate glass, 7972 ULE (Ultra-Low Expansion Glass) with a CTE of 10^{-8} K^{-1} from 5°C to 35°C at their premium quality grade and offers a very good long term stability.

Glass ceramics can also have the property of high dimensional stability. Schott's Zerodur class 0 extreme has a CTE of $7 \cdot 10^{-9}$ K^{-1} from 0°C to 50°C. Zerodur shows a long-term shrinking, also called aging of the material which was examined by the PTB [30]. Zerodur can also show CTE hysteretic effects due to thermal cycling. Heating up Zerodur components to ≈ 700°C, changes its low expansion properties. An additional effect is that at temperatures around 130°C to 320°C, the dimensions as well as the zero crossing of the CTE of Zerodur can change. This effect can be very critical for mirror coatings [31]. A similar glass ceramic is produced by Ohara and is called Clearceram-Z with a slightly higher CTE.

SiC (Silicon Carbide) [32] and CFRP are increasingly used in applications where high dimensional stability and light weight structures are required. Silicon Carbide is composed of tetrahedra bonded atoms of Silicon and Carbon and has properties of high strength, hardness, and also low thermal expansion. The high thermal conductivity and the low density are properties which are strongly needed in many space applications [33].

Another isotropic ceramic material produced by ECM (Engineered Ceramic Materials GmbH) is Carbon-fiber reinforced Silicon Carbide, CeSiC type MF, where the SiC is additionally reinforced by microscopic Carbon fibers to improve the properties of the SiC, which lowers the CTE at cryogenic temperatures. ECM, the supplier of CeSiC gives CTE values of $0.00 \cdot 10^{-6}\,\mathrm{K}^{-1}$ from 20 K to 85 K up to $2.74 \cdot 10^{-6}\,\mathrm{K}^{-1}$ at 313 K to 393 K. [34, 35]

For CFRP a lot variables can be changed to tune the CTE of the material, e.g. fiber volume ratio, type of epoxy or angle of laminated layers. The positive CTE of the epoxy can be compensated by the slightly negative CTE of the Carbon fibers. In theory, a CTE value of zero can be achieved at least in one direction, but due to the manufacturing tolerances CTE values of about $10^{-6}\,\mathrm{K}^{-1}$ are realistic. A big disadvantage of CFRP is the shrinking due to moisture release. [36, 37, 38]

There are a lot of different Invar alloys. The most common is Invar36, which is known as (Fe-36Ni). Its CTE varies due to the production process from $0.8 \cdot 10^{-6}\mathrm{K}^{-1}$ to $1.6 \cdot 10^{-6}\mathrm{K}^{-1}$ over a temperature range of 30°C to 100°C. Invar is mainly used in applications, where the dimensional stability has to be rather low in combination with the ability of good mechanical machining. The manufacturing process of Invar is complicated and the method varies between manufacturers. Due to different manufacturing processes, the variation in the

CTE values are set and the reliability of the material is not as good as other low CTE materials. [39]

Titanium is very often used in space applications due to its physical properties, such as its non-magnetic behavior, light weight (≈50% lighter than steel with approximately its same strength) and it has the property of being corrosion resistant. The linear coefficient of thermal expansion is given with $5 \cdot 10^{-6}\ \mathrm{K}^{-1}$ at $-150°\mathrm{C}$ up to $\approx 9 \cdot 10^{-6}$ at 20°C – 100°C. [40]

Fused Silica, SiO_2, is a noncrystalline glass made of quartz. This glass is very common in optical systems due to its of low thermal expansion coefficient ($0.51 \cdot 10^{-6}\,\mathrm{K}^{-1}$ at 0°C – 100°C), transparency over the complete visible spectrum, and it can be machined e.g. polished or lapped to reach very homogenic and flat surfaces for optical components. [41]

Figure 1.4.: Photograph of a selection of material sample tubes. (1) a samples of Clearceram, (2) a sample of Zerodur, (3) a sample of ULE, and (4) a sample of CFRP.

A selection of samples tubes of different materials for the use in our CTE metrology system are shown in Figure 1.4. Beginning with highly stable glass ceramics: (1) a samples of Clearceram, (2) a sample of Zerodur, (3) a sample of ULE, and (4) a sample of CFRP. All samples have approximately the same dimensions of 120 mm length, a inner diameter of 20 mm, and the outer diameter can variate up to 40 mm.

2. Motivation and roadmap of this thesis

2.1. Motivation for this system design

Due to the increasing need of highly dimensionally stable structures in space applications a CTE metrology facility was designed and built in cooperation with the German Aerospace Center (DLR), the Center of Applied Space Technology and Microgravity (ZARM) at the University of Bremen, and Airbus DS GmbH in Friedrichshafen. The goal was to determine material samples and structures at their operating temperature of specific space missions at a wide temperature range from 140 K to 333 K. The design of a two beam heterodyne interferometer was selected and realized due to very low noise displacement measurements (picometer level) demonstrated in the proposed LISA mission concept. With this technique, an accuracy of $< 10^{-8}\,\mathrm{K}^{-1}$ was achieved, considering the measured tilt of the sample. This factor is part of the uncertainty budget due to the tilt-to-length coupling, and contributes an error of $< 10^{-9}\,\mathrm{K}^{-1}$. The tilt-to-length coupling is the biggest uncertainty of the system, this effect occurs due to the parallel beam design of the set-up. An additional factor considered in the development of this test bed is the capability of measuring all kind of materials without concerns on their surface roughness, or if they are monolithic or composite materials. This was realized by specially designed mirror mounts which can be used in all tube shaped materials.

This technique is also crucial to determine the dimensional stability of structures for space applications and their joint technologies between different materials with different CTEs. In this thesis the dimensional expansion of a

0.5 m long CFRP tube with Zerodur endfittings was investigated. The dimensional stability of this structure was of interest where Zerodur parts are assembled with a dedicated process to lower CTE materials, by using adhesive to compensate the stress caused by the unequal thermal expansion.

2.2. Thesis roadmap

This section outlines a roadmap that explains the structure of the experimental systems design, realization and verification. Together with the two introductory chapters, this thesis has three additional chapters containing descriptions and results of the metrology system:

- Chapter 3: CTE metrology system design and realization
  - Set-up (**A**): CTE measurements at room temperature
  - Set-up (**B**): CTE measurements at room temperature and at low temperatures
- Chapter 4: CTE metrology system verification and uncertainty analysis
- Chapter 5: Application for space structures

In Chapter 3 ”CTE metrology system design and realization” the principle of the system design are explained as well as the two different set-ups realized:

The first set-up called ”set-up (**A**)” was built up at Airbus DS GmbH in Friedrichshafen and first CTE measurements at room temperature of tube shaped samples were taken to verify the system.

A second set-up ”set-up (**B**)” was built at the DLR in Bremen with the possibility to measure the dimensional stability of sample tubes at room temperatures as well as at lower temperatures. Some subsystems are carried over from set-up (**A**), but most subsystems were completely new designed and optimized to the new target temperature range of 140 K to 250 K.

In Chapter 4 ”CTE metrology system verification and uncertainty analysis” both set-ups are verified and a detailed uncertainty analysis is presented.

In Chapter 5 "Application for space structures" the verified metrology system "set-up (**A**)" was adapted with a new thermal system to enable measurements of bigger structures for space applications. The dimensional stability of a GRACE Follow-On triple mirror assembly breadboard with a length of 0.5 m was investigated. The CFRP tube and its endfittings and the used joint technology is a technology demonstrator for future space missions.

In addition to the main experiments, another CTE metrology set-up and measurements are described in Appendix A "Alternative LISA telescope design investigation". The dimensional stability of a Silicon Carbide telescope structure was investigated at the University of Florida with a completely different optical set-up.

3. CTE metrology system design and realization

The whole CTE metrology system of the dilatometer can be functionally divided into the following subsystems:

1. Optical set-up (see Section 3.1.1)
    - Laser module and frequency reference
    - Heterodyne frequency generation
    - Interferometer
    - Phase and intensity stabilization
2. Signal processing (see Section 3.1.3)
3. Thermal system (**A**) (see Section 3.2.2)
   Thermal system (**B**) (see Section 3.3.2)
4. Sample and sample support, including specially designed sample mirror mount (see Section 3.1.2)
5. Thermal control of system (**A**) (see Section 3.2.3)
   Thermal control of system (**B**) (see Section 3.3.3)

These subsystems are connected to each other with fibers or wires. The functional interaction between them is outlined in Diagram 3.1 and a photograph of the metrology system is shown in Figure 3.2. During the research work of this thesis, two different set-ups were realized and CTE values of

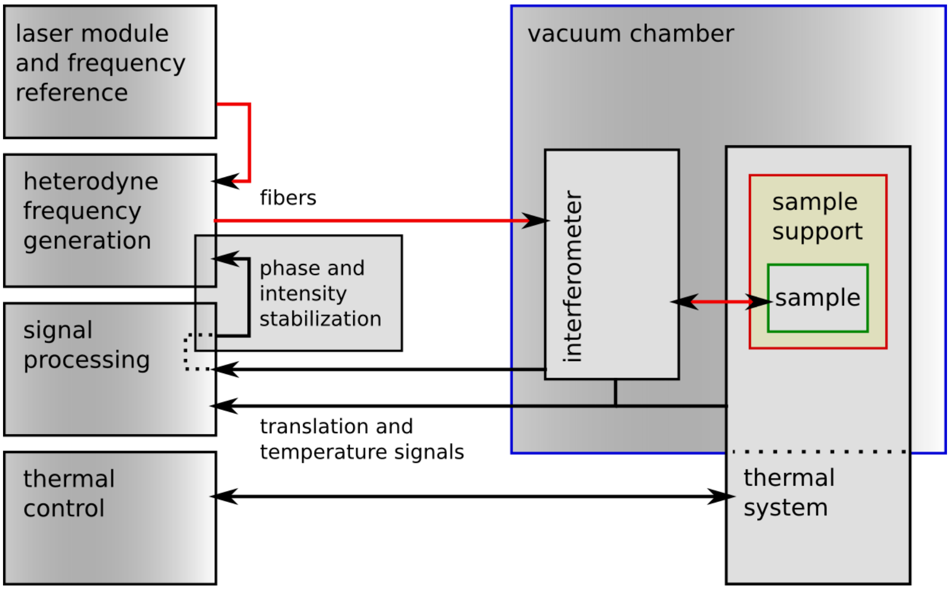

Figure 3.1.: Functional diagram of the dilatometer set-up, black: electronic signals, red: laser beams.

dimensionally stable materials were measured and compared with their manufacturer specifications to verify the metrology system. The first set-up (set-up (**A**)) was built at Airbus DS GmbH in Friedrichshafen, which was able to determine CTEs in a temperature range of 293 K – 333 K using thermal system (**A**) with Peltier elements. Certain subsystems were already available at Airbus DS GmbH and first CTE measurements were done without further design optimizations. Initially, the laser was not frequency stabilized and this was identified to be the main noise source. The laser was then stabilized to an optical resonator for subsequent measurements.

The second part of this thesis describes set-up (**B**), which was designed and built up at the DLR (German Aerospace Center), Institute of Space Systems in Bremen. This set-up was completely new designed with the exception of the sample support mount, which was reused. The optical set-up was adapted such that it would be compatible with the new thermal subsystem to measure at low temperatures. Temperatures down to 140 K are achievable by using a pulse tube cooler. In set-up (**B**) the laser was stabilized to an Iodine reference to minimize the laser frequency noise.

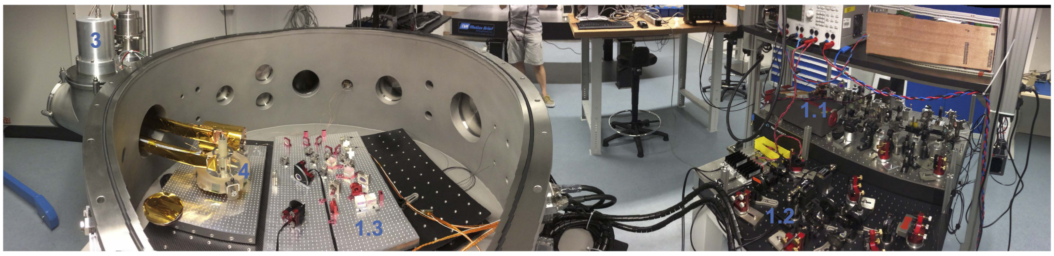

Figure 3.2.: Photograph of the dilatometer set-up: Laser module and frequency reference (1.1), heterodyne frequency generation (1.2), interferometer (1.3) and the sample mounted in the sample support (4) are placed in vacuum chamber, thermal system (3) attached to the vacuum chamber. The electronic subsystems thermal control and phase and intensity stabilization are placed behind or under the vacuum chamber.

3.1. Subsystems used in set-up (A) and set-up (B)

3.1.1. Principle of optical set-ups

The optical set-up consists of a stabilized laser, the heterodyne frequency generator and the interferometer itself with power and phase stabilization control loops (see Figure 3.3). The actual interferometer of set-up (**A**) is shown in Section 3.2.1 and the one of set-up (**B**) is shown in Section 3.3.4.

Laser module with frequency reference Laser frequency noise translates into length noise due to the unequal arm length of the interferometer (distance between M1 and M2 in Figure 3.3 and also referred as 'length' or 'absolute length' in the following), i.e.:

$$\delta\ell = \ell\frac{\delta\nu}{\nu}, \tag{3.1}$$

where $\delta\nu$ is the laser frequency noise, ν is the laser frequency, ℓ is the length of the sample and $\delta\ell$ the length changes due to laser frequency noise. To minimize this effect in set-up (**A**), the λ=1064 nm Nd:YAG laser (Mephisto from Innolight) was locked to an optical resonator and a frequency stability lower than $10^2\,\mathrm{Hz}/\sqrt{\mathrm{Hz}}$ for frequencies higher than 10^{-2} Hz are achieved (see

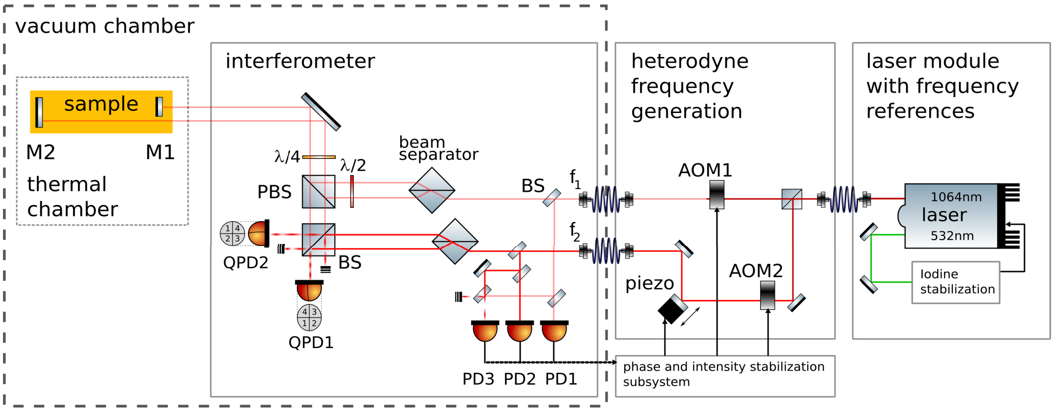

Figure 3.3.: Dilatometer optical set-up: M1 and M2 are mirrors clamped to the sample. QPD1 and QPD2 measure the pathlength of the beam reflected off M1 and M2, respectively. The phase difference is proportional to the length changes in the sample and is measured by a phasemeter at heterodyne frequency (10 kHz). The intensities of the beams are measured by PD1 and PD2 and controlled by the RF-amplitude of the AOM drivers. The piezo is driven by the phase difference of the beams coming out of the optical fibers. This improves the common noise cancellation when subtracting the signals measured at QPD1 and QPD2.

Appendix B.1). In set-up (**B**), the λ=1064 nm Nd:YAG laser (Prometheus from Innolight) with a frequency doubled output of 532 nm was stabilized to a molecular Iodine hyperfine transition (see Appendix B.2) to minimize the noise in the length measurement. For the Iodine stabilized laser a noise level of 10 kHz/$\sqrt{\text{Hz}}$ for frequencies higher 10^{-2} Hz were achieved. In both set-ups the frequency noise, $\delta\nu$, after stabilization is better than 10 kHz/$\sqrt{\text{Hz}}$ in the bandwidth of interest. Due to our periodical signals, just the short-term stability is of interest. The long-term frequency drifts can be minimized in post-processing with first or second order high pass filters. The noise level of 10 kHz/$\sqrt{\text{Hz}}$ is equivalent to $\simeq$2.8 pm for a 0.1 m long sample and ν=281 THz, and does not limit the performance of the CTE measurement.

Heterodyne frequency generation The laser beam is guided from the laser module through an optical fiber to the heterodyne frequency generator where the light is divided into two beams by a 50/50 beam-splitter and sent to two acoustic optical modulators (AOMs) to shift their frequencies (see Figure 3.3). One of the beams is frequency-shifted by 80 MHz and the other by 80 MHz and an offset of 10 kHz, where 10 kHz is the so-called heterodyne frequency. The RF signals are provided by two signal generators (DDS 408A from Novatech Instruments) locked to a Rubidium clock (FS725 from Stanford Research Systems). This same Rubidium clock is used as master of the the FPGA (field-programmable gate array) based phasemeter to ensure the same heterodyne frequency generated by the DDS signal generator and the FPGA. After AOM2 a mirror is mounted on a piezo actuator to change the pathlength of one laser beam for the phase stabilization. The frequency shifted laser beams are collimated each into a fiber and guided to the interferometer in the vacuum chamber. The phase and intensity stabilization are explained in the following paragraphs.

Interferometer The main part of the dilatometer is the interferometer itself, which measures the expansion/contraction, $\Delta\ell$, and the absolute length, ℓ, of the sample [42]. Figure 3.3 shows the measurement principle of the heterodyne interferometer based on the concept of Wu et al. [43, 44]: two laser beams with different frequencies, f_1 and f_2 ($|f_1 - f_2|$=10 kHz), are guided through two beam separator cubes. The beams are reflected and transmitted in a way such that two parallel beams are generated for each frequency, reference beam and measurement beam. The two beams with frequency f_1 are guided to the sample, where one beam is reflected off mirror M1 and the other beam is reflected off mirror M2. Both reflected beams are coherently overlapped with the reference beams by using a quarter-wave plate and polarizing beam-splitter at the quadrant photodetectors (QPDs).

The length change ($\Delta\ell$) of the sample is the phase difference of the heterodyne signals:

$$\begin{aligned} \Delta\ell &= \frac{\lambda}{4\pi}[\phi_{\mathrm{QPD}_1} - \phi_{\mathrm{QPD}_2}] \\ &= \frac{\lambda}{4\pi}[(\phi_{f_1,\mathrm{M1}} - \phi_{f_2}) - (\phi_{f_1,\mathrm{M2}} - \phi_{f_2})] \\ &= \frac{\lambda}{4\pi}[\phi_{f_1,\mathrm{M1}} - \phi_{f_1,\mathrm{M2}}], \end{aligned} \tag{3.2}$$

where ϕ is the phase of the signals. ϕ_{QPD} is measured by a phasemeter based on a single bin discrete Fourier transform (SBDFT) [45] and is explained in Appendix 3.1.3.

The absolute length, ℓ, between the mirrors M1 and M2 is measured by modulating the frequency of the laser:

$$\ell = \nu\frac{\Delta\ell}{\Delta\nu}, \tag{3.3}$$

where $\Delta\ell$ is measured by the interferometer, $\Delta\nu$ is the modulated laser frequency (in the GHz range) and ν is the absolute frequency of the laser. The frequency and its changes are recorded by a wavelength-meter (High-Finesse WS6-600) with a noise level of $\simeq$ 10 MHz. This was done in the later measurements with set-up (**B**) (see Section 4.3.5 Paragraph "Absolute length measurement") at the earlier measurements the length was measured by a caliper.

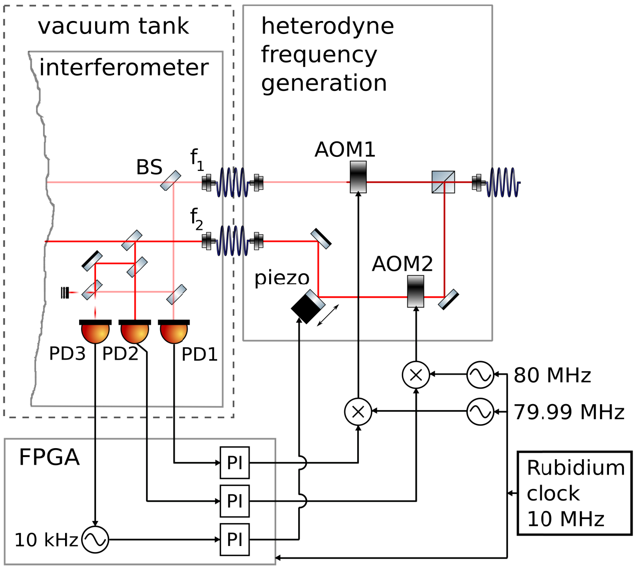

Figure 3.4.: Schematic of the phase and intensity stabilization.

Phase and intensity stabilization Additional actuators and detectors of the frequency generation module and the interferometer are used for the intensity and phase stabilization (see Figure 3.4). The latter is needed to avoid non-linear phase effects of the laser beams caused by the fibers and the AOMs [46] and non-linear effects related to analog-to-digital converters and the phasemeter. The phase stabilization is done by comparing the phases of the two beams after the AOMs and adjusting the optical path of one of them to match the phase of the other in a closed-loop control using a piezo actuator. The two frequencies f_1 and f_2 are overlapped on the interferometer board and the heterodyne frequency is detected by using photodetector PD3. This signal is computed by the FPGA such that the measured signal is compared to a 10 kHz signal generated on the FPGA which is also locked to the same Rubidium clock as the AOM drivers. This error signal, the phase information of the down-mixed 10 kHz signals is provided to the FPGA based PI controller. The output of the controller is amplified and connected to a piezo actuator in the heterodyne frequency generation set-up.

The intensity control is performed by the AOMs drivers. The power levels of the laser beams f_1 and f_2 are measured with the photodiodes PD1 and

PD2. These DC signals are also read in by the FPGA and a FPGA based PI controller is used to keep it constant by multiplying the actuating signal with the RF signal driving the AOMs using an Analog Devices multiplier, ADL5391. The influences of intensity noise to our measurements could not be measured, however, it enables the same laser power level for each measurement campaign.

3.1.2. Sample and sample support, including specially designed sample mirror mount.

The developed dilatometer is able to measure the CTE of tube shaped samples with a maximum length of 120 mm, an inner diameter of 20 mm and a maximum outer diameter of 40 mm (see Figure 3.5). The mechanical set-up is crucial to minimize errors due to thermal gradients, mirror expansion or tilt-to-length (TTL) coupling (for instance, 0.2 µrad sample tilt causes an error of 1 nm in length). [47]

The mirrors M1 and M2 are essential for the measurement quality: their expansion should be kept to negligible levels for the CTE measurement. Invar36 mounts (see Figure 3.6), have been designed to minimize this effect [48]. They have three tips at the end of the springs to hold the mirror in the sample. These tips are at the reflecting surface level of the sample with an accuracy smaller than 0.1 mm. This plane is the so called thermal neutral plane, having the feature that an expansion of the mirror mount (and/or the mirror itself) does not change the position of the reflecting surface in the sample. The upper mirror has a diameter of 12 mm and the lower mirror is a semi-disk (also called D-shaped mirror) to reflect off one laser beam and allow the second laser beam to reach the upper mirror.

The sample support (see Figure 3.5) has been designed such that its tilt and TTL coupling are minimized. The support is based on Zerodur and Invar36 due to their low CTEs, although the effect of the support on the measurement is mainly driven by the Zerodur component. Three legs mounted to the base plate of the support can be adjusted in height, which allows the sample to be aligned to the laser beams, with a margin of 2 mm (±1 mm) on each leg,

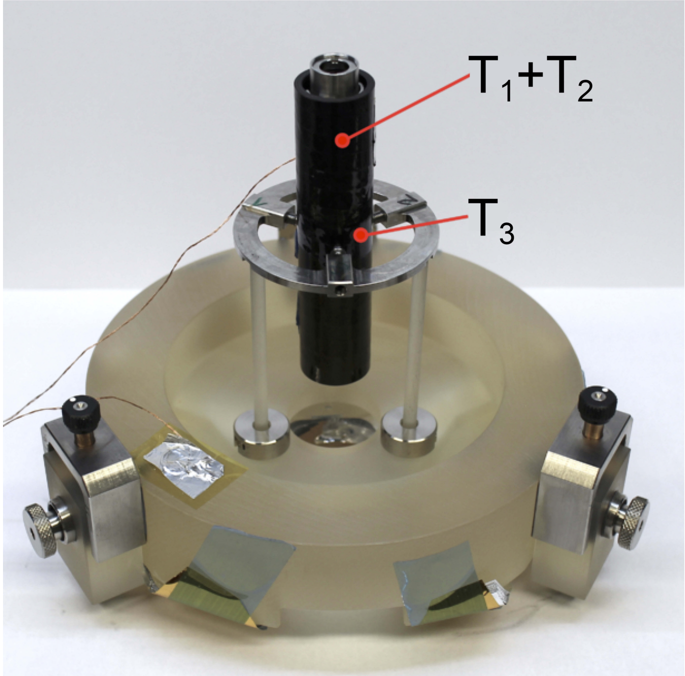

Figure 3.5.: Photograph of the Zerodur support design to minimize the expansion/contraction of the entire dilatometer set-up. All Invar parts (ring and parts of the legs) are designed to minimize thermal couplings to the sample. T_x are temperature sensors (Pt-100). T_1 and T_3 are placed on the outer surface of the tube shaped CFRP sample while T_2 is placed in the inner surface of the tube. An additional sensor is placed at the Zerodur support. A specially designed sample mirror mount can be seen in the upper end of the sample.

resulting in an angle range of 13 mrad (see Figure 3.7). The horizontal screw generates a force over the spring to press the leg to the baseplate. When the friction between the baseplate and the leg is large enough, the leg is fixed to the baseplate and only the Zerodur is responsible for the dimensional stability, which is convenient due to its very low CTE.

Finally, the sample is affixed to the support by a 3-point bearing that fixes the sample with three spring-loaded thrust pads. The contact between the pads and the sample is a thin vertical line to minimize heat transfer. The spring-loaded thrust pads are screwed with fine threads into the ring and pressed against the sample. On each pad, three disk springs are used to protect the samples. The fixing ring is made of Invar36 to minimize thermal

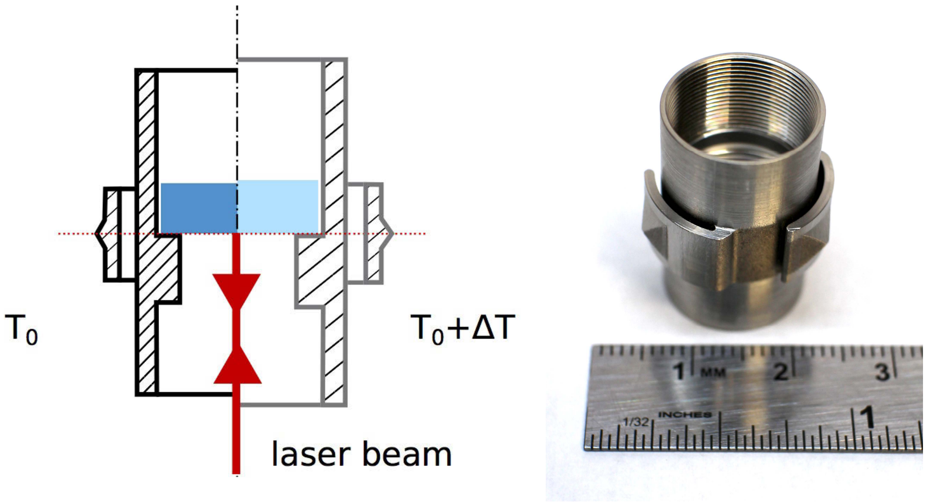

Figure 3.6.: Left: a depiction of the mirror mount at two different temperatures, T_0 and $T_0 + \Delta T$; the red dashed line shows the thermal neutral plane. The tips of the clamps are located in the same plane as the reflecting mirror surface. Consequently, expansion/contraction of the mount and the mirror have minimal impact on the CTE measurement. This is shown in the picture with the mirror position at T_0 and $T_0 + \Delta T$. Right: a photograph of the mirror mount [48].

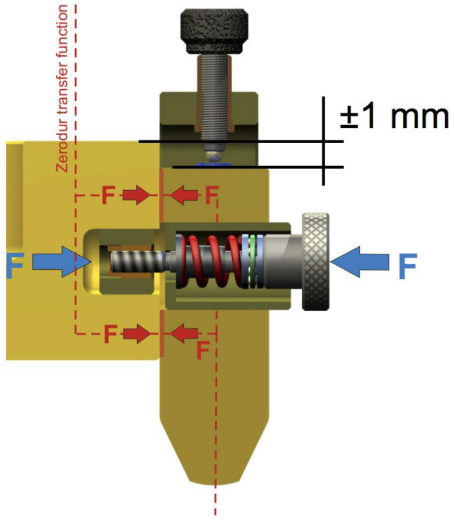

Figure 3.7.: CAD drawing showing the adjustment principle of the Zerodur leg and the baseplate where, after the adjustment, only the Zerodur material has an impact on the dimensional stability. [49]

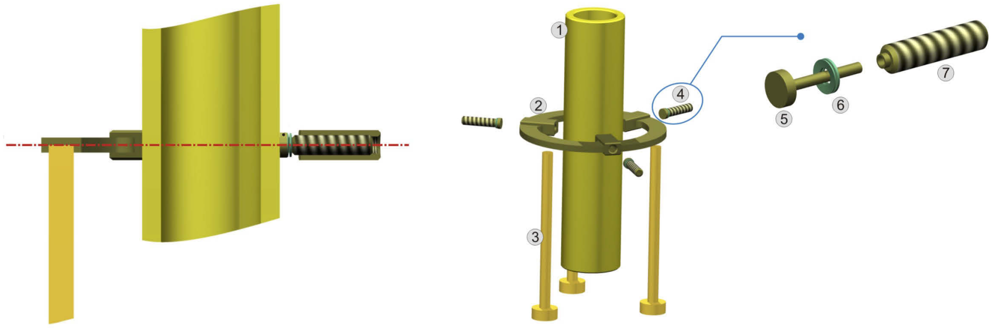

Figure 3.8.: Principle of the thermally neutral plane of the sample fixture. 1: sample, 2: Invar fixing ring, 3: Zerodur strut, 4: spring-loaded thrust pad, 5: thermally neutral plane. [49]

expansion effects. Moreover, the central axis of the spring-loaded thrust pads and the bearing position of the fixing ring define a thermally neutral plane (see Figure 3.8), and ideally a temperature change should not alter the position of the sample. However, this part has been identified as critical and performance limiting due to TTL coupling (see Section 4.1). [47, 49]

3.1.3. Data processing

For data acquisition and data processing a National Instrument PXI system with a Virtex-5 LX110 FPGA chip (Model NI FPGA card: PXI-7854) is used, where the analog inputs are limited to 8 channels. In our set-up we need 8 inputs for the two quadrant photodetectors (QPD), one input for the beat note to control the phase lock and two inputs for the laser power stabilization. The latter three inputs are read in via the analog inputs and the 8 input signals of the QPDs are digitized and read in via 8 of the 96 digital channels of the FPGA.

The circuits and PCB (printed circuit board) designs of the detectors and the ADC-board (analog-to-digital converter) were developed in collaboration with Airbus DS GmbH in Friedrichshafen, HTWG Konstanz, ZARM at University of Bremen and the DLR in Bremen and the results are described in Reference [50].

In Figure 3.9 a schematic of one transmission channel of the detected signal from the photodiode to the FPGA is shown. The photodiode is mounted on a trans-impedance converter PCB where the heterodyne signal (10 kHz) is amplified and low-pass filtered. Between the diode PCB and the ADC PCB, the signal is transmitted through long cables (5 m) from inside the vacuum chamber, through a vacuum flange and several Sub-D connectors where the electromagnetic shielding is not ideal. To minimize the electromagnetic impact in the transmission lines between the two PCBs, a method of differential signaling was implemented.

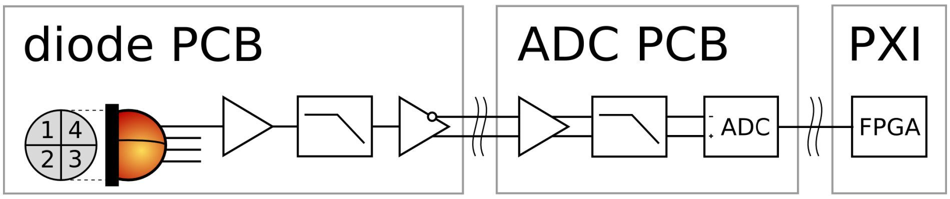

Figure 3.9.: Schematic of the data acquisition, showing one channel of a quadrant photodiode.

The method of differential signaling transmits the measured signal and its inverted counterpart. On the ADC board, the two inverted signals are processed where the excess noise can be minimized at the ADC chip. Prior to the ADC chip, an amplifier and a low-pass filter provide a signal with the correct amplitude for the ADC input range. After the ADC, a National Instrument cable is transferring the digitized signal to the FPGA, mounted in the National Instrument PXI.

The FPGA is programmed using LabVIEW, where the so called phasemeter, based on a single bin discrete Fourier transform (SBDFT) [45] multiplies the measured heterodyne signal by two quadrature (sine and cosine) mixers at a sampling rate of 160 kHz and a 16 bit resolution (see Figure 3.10). The generated sin and cos have the same frequency like the heterodyne frequency (10 kHz). The FPGA and the frequency sources for generating the heterodyne frequency are locked to a Rubidium clock from Stanford Research System model FS725. After the mixer, a filter at 5 Hz passes only the difference frequency, resulting in a DC signal with the phase information. After a data reduction by a factor 8000, the phase information is sent with a first-in-first-out (FIFO) data stack to the computer (PC) located in the PXI chassis next to the FPGA. On the PC, the translation is calculated using the arc tangent (atan) function. Each segment of the QPDs is processed and is saved in a text file individually. The expansion and tilt values are calculated in post-processing in Matlab. [50]

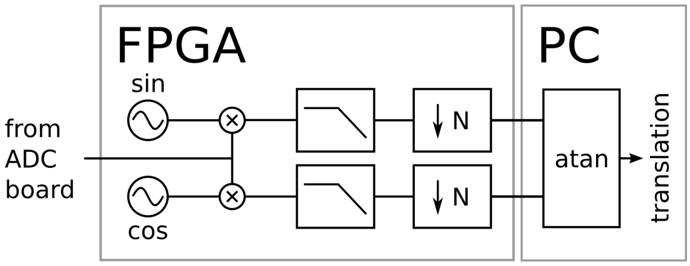

Figure 3.10.: Schematic of the data processing of the FPGA and PC.

To calculate the expansion of the sample in Matlab, the signals of all segments of QPD2 are summed up and subtracted from the summed signals of QPD1:

$$\Delta\ell = \sum \text{QPD1} - \sum \text{QPD2}. \tag{3.4}$$

3.2. Subsystems for set-up (A)

3.2.1. Optical set-up

The experimental set-up of the dilatometer at Airbus DS GmbH in Friedrichshafen is based on a highly symmetric heterodyne interferometer (see Figure 3.11), which was originally designed as a demonstrator for an optical readout for the LISA [1] space mission. This interferometer was built and used for mirror surface investigations and a more detailed description can be found in Reference [51]. For the dilatometer set-up, this interferometer is capable of ultra-precise measurements of small variations in translation between a reference and a measurement mirror which are attached to the sample.

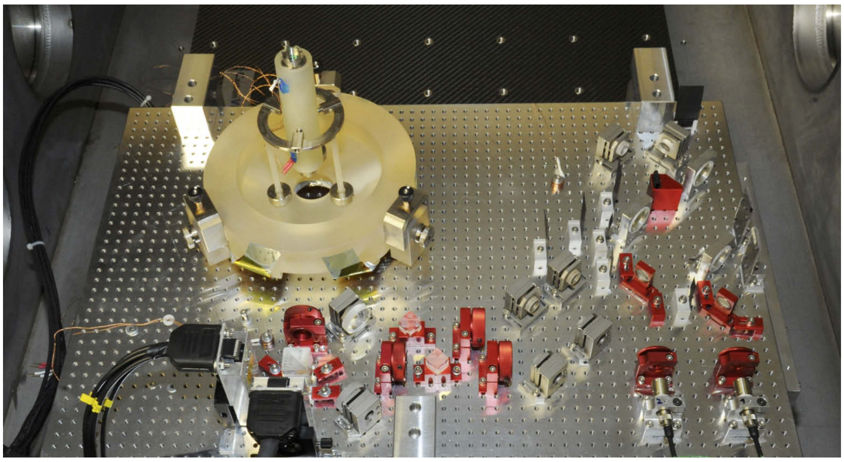

Figure 3.11.: Photograph of the experimental set-up (**A**) showing the interferometer and the device under test with its support located in the vacuum chamber.

The principle of the optical measurement system is described in Section 3.1.1. In particular, set-up (**A**) uses a NPRO-type Nd:YAG laser source with a wavelength of 1064 nm for the generation of the laser frequency (f_0), which is frequency stabilized to an external cavity (see Appendix B.1). The laser beam is split in two by a beamsplitter: one beam is shifted by 79.99 MHz and the other one by 80 MHz by the use of two phase-locked AOMs. Both beams are injected into the vacuum chamber by optical fibers. The two frequency shifted beams are launched into the optical bench at a height of 20 mm and each beam has a diameter of approximately 1.44 mm, and an optical power of 3 mW. A schematic of the interferometer board with its optical components is presented in Figure 3.12.

At the optical bench, each beam is split into three beams at a glass plate. One beam of each frequency is detected at a single element photodiode (SE1 and SE2). This signal is used for the intensity stabilization. The signal on SE3, where the two frequencies are superimposed, provides a heterodyne beat signal of $f_{het} = |f_2 - f_1| = 10\,\mathrm{kHz}$, which is used for a phase stabilization that is implemented to cancel non-common-mode phase-effects. The third pair of the beams is further used for the measurement interferometer. Additional mirrors are necessary to adjust the beams precisely to improve the amplitude of the

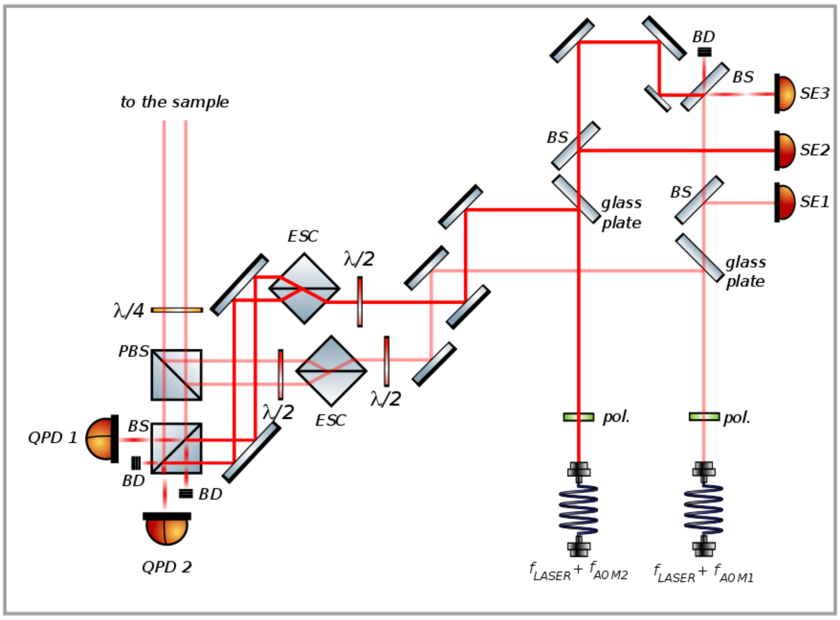

Figure 3.12.: Schematic of the interferometer of set-up (**A**).

heterodyne signals. The energy separator cube (ESC) is used to generate parallel beams of each laser beam. One pair is reflected to the sample by a PBS. The reflected beams from the sample passes twice through a quarter-wave plate where the linear polarization turns by 90 degrees. The two beams get transmitted at the PBS and get superimposed with the other pair of laser beams. The phase signals are detected by the QPDs. [16, 51, 52]

3.2.2. Thermal system (A) – 293 K to 333 K

The top level requirements formulated for this heating system are:

- Homogeneous and defined tempering of the sample under investigation.
- Thermal influence on the surrounding systems (sample support, interferometer) should be minimized.

In the thermal system of the dilatometer the heat transfer is very important to ensure a sufficient temperature variation at the sample and to minimize drifts in the expansion measurements the optical set-up has to be shielded against the thermal system. The heat is transferred in three different ways:

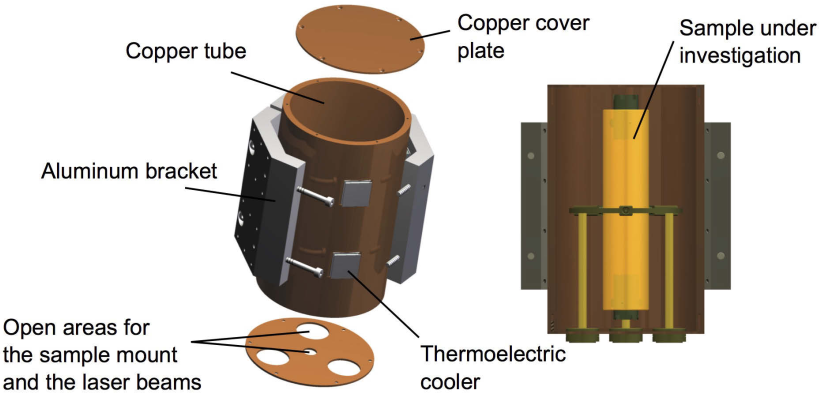

Figure 3.13.: Heating device assembly on the left, sectional view including the sample on the right [49].

- conduction or diffusion,
- convection,
- and radiation.

Conduction is the most relevant heat transfer, it is the mechanism where energy is transferred in physically contacted objects due to moving or vibration atoms interacting with other atoms.

The convection mechanism is the heat transfer when a flow of a fluid occurs. For example, when a fluid absorbs heat, the density changes and due to gravitational effects the warmer molecules start to move and transfer the heat. This mechanism is negligible in our setup where our experiment is in vacuum.

Thermal radiation is the heat transfer mechanism based on electromagnetic waves and occurs in vacuum as well as transparent solids or fluids. All objects above 0 K emits electromagnetic waves. This heat transfer is very important in our set-up, thermal sensitive parts have to be shielded against thermal radiation of parts with different temperature. This mechanism is also used to apply a temperature signal to the sample.

This heating device was specifically designed for the tube shaped samples. Therefore, a cylindrical structure was made of Copper due to its high heat conductivity. The thermal output is generated by eight thermoelectric coolers

(TEC) also known as Peltier elements, which are compressed between the Copper tube and four Aluminum brackets. After the assembly, the Copper tube is enclosed by two Copper cover plates and the sample is completely enclosed. This provides an even exchange of thermal radiation between the sample and the Copper structure. In the lower Copper plate are four holes, three for the sample support and one for the laser beams. In order to improve the emissivity of the Copper, Kapton tape ($\epsilon \sim 0.9$) was applied inside the Copper tube. The heating device assembly is presented in Figure 3.13.

The heating device is mounted on an Aluminum beam that is clamped between the walls of the vacuum chamber. The whole assembly is wrapped by MLI (multilayer insulation) foil in order to reduce the heat transfer to the sample support and the interferometer. The MLI foil consists of seven metal coated plastic layers with a reflectivity of thermal radiation above 95%. The MLI foil filters the radiation such that we were not able to measure temperature variations at the frequency of the temperature signals (period of several hours and an amplitude of several Kelvin) of the thermal system on other places in the vacuum chamber like the interferometer. A photograph of the ready for use assembly is shown in Figure 3.14. [49]

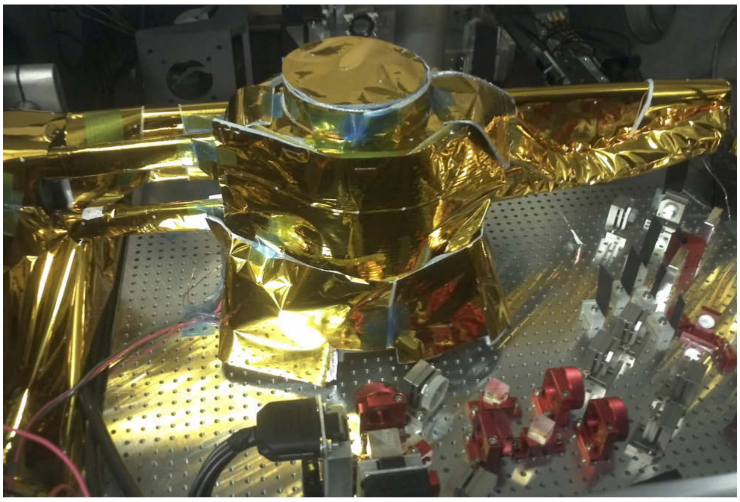

Figure 3.14.: Photograph of the interferometer of set-up (**A**) with the sample support and the thermal system (**A**) covered with MLI.

3.2.3. Thermal control of system (A)

The control of the TEC heating chamber is carried out by a digital PID temperature controller. A schematic of the control loop is shown in Figure 3.15. The controller can be accessed with LabVIEW to apply temperature cycles to the sample, which can be individually programmed. Also the parameters for the PID controller are programmed with the LabVIEW program and they are finely tuned experimentally. Usually a sinusoidal function with a period of several hours is a suitable choice because the heating and cooling occurs smoothly and the analysis of the resulting expansion and contraction is simple. Here, the change in dimension of the sample also shows a sinusoidal profile which follows the temperature cycle, as expected. Another possible temperature profile is a step function. This way, the effect of a strong periodic change of temperature can be investigated.

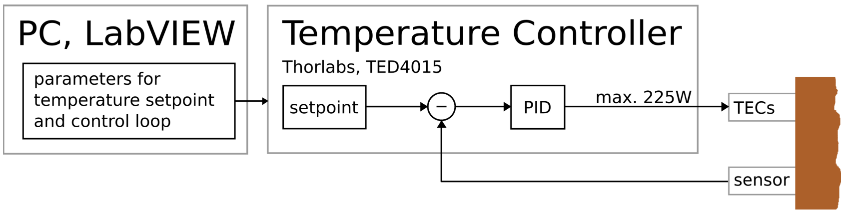

Figure 3.15.: Control loop of the thermal system (**A**). The temperature controller provides maximum 225 W to the TEC elements to cool or heat the copper vessel surrounding the sample.

In set-up (**A**) a temperature controller from Thorlabs TED4015 was used, which provides a good temperature stability of 0.002°C in a period of 24 h with a resolution of 0.001°C. A current range of ±15 A can be supplied resulting in a maximum power output of 225 W at 15 V. To measure the actual temperature in the heating chamber a Pt-100 temperature sensor was used in a 4-wire sensing method with a thermal conducting adhesive. The 4-wire sensing method minimizes the uncertainty of the temperature measurement, the resistance of the wires and the internal resistance of the measurement device are balanced.

3.3. Subsystems for set-up (B)

The main objective of this thesis was to built up a new set-up, set-up (**B**), with the capability to measure at low temperatures, down to 140 K. The principle of set-up (**A**) was adapted and the optical and electrical set-ups were rebuilt with minor changes. The most significant change was the thermal system, which introduced large vibrations that had to be minimized. The thermal gradients in the system had to consider several subsystems. A CAD model of the mechanical and thermal set-up inside the vacuum chamber is shown in Figure 3.16. The support of the sample and the mirror mounts described in Section 3.1.2 are the same as in set-up (**A**) and are used for measurements at room temperature as well as at low temperatures. Parts of this section are published in Reference [53]. The following subsections explain the subsystems of set-up (**B**) as depicted in Figure 3.1.

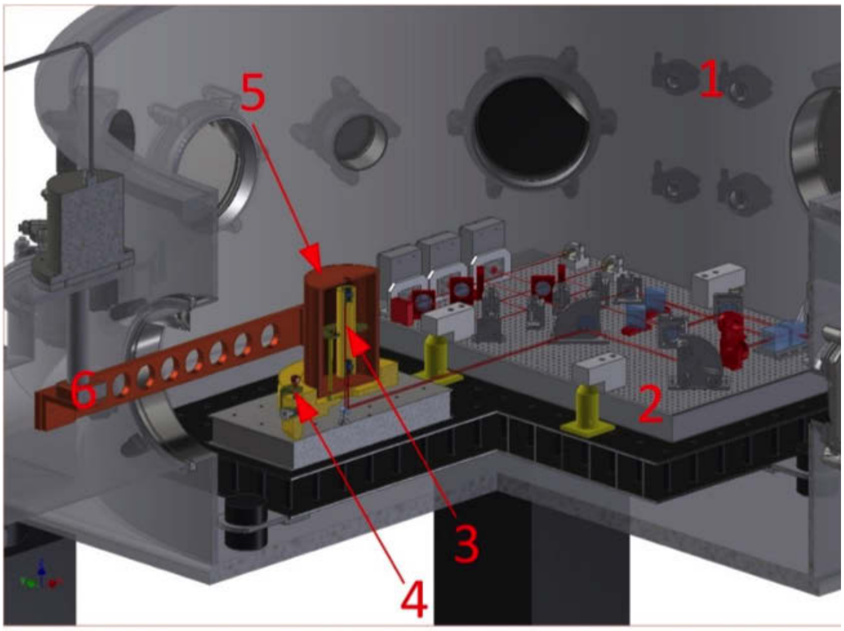

Figure 3.16.: CAD model of: (1) vacuum chamber, (2) interferometer, (3) sample (DUT), (4) support of the sample, (5) Copper radiator connected to the cold head by means of Copper bars (6).

3.3.1. Vacuum chamber

A vacuum chamber is needed to minimize disturbances in the expansion measurement, which are introduced by acoustics, air and refraction index fluctuations. To get a stable refraction index of $n = 1$ a vacuum with pressure lower than 10^{-3} mbar is achieved. The vacuum chamber was designed to have sufficient room for the optical and thermal set-ups and to fit a 900 mm × 600 mm breadboard at the bottom of the chamber. The round chamber (see Figure 3.16) has a diameter of 1200 mm and a height of 525 mm. The round chamber is cheaper and lighter due to the thinner walls than a rectangular chamber. For electrical and optical feed-throughs, vacuum pumps, valves and pressure gauges 26 ISO-K and ISO-KF flanges are placed at the side of the cylinder. For future projects requiring larger structures in the vacuum chamber like telescopes, an additional ring can be mounted on top to get a larger volume. To minimize the seismic vibration the whole vacuum chamber is mounted on four damping systems, OTAL (2000) from Melles Griot at each corner of the rectangular baseplate.

Due to the large temperature gradient between the heating vessel (down to 100 K) and the interferometer (room temperature), the thermal isolation as well as the dimensional stability have to be very high. In order to decouple the heating vessel from the interferometer, the sample support is placed on a separate Aluminum breadboard. Both breadboards are mounted with a three point statically indeterminate mounting by Zerodur feet. The breadboard position is stable by gravity (see Figure 3.17).

A L-shaped aluminum adapter is used as the point of contact between the top surface of the interferometer breadboard and the top of the Zerodur feet. The adapter was designed such that the tip of the Zerodur mount is at the same height as the laser beams. Hence, a thermal influence on the effective length (height of the laser beams) consists just of Zerodur parts. The mounting of the optical fibers and the adapter are made of Aluminum with the same CTE and their respective expansions are balanced, showing no influence on the height of the laser beams. This correlation is illustrated in a sectional view in Figure 3.17. The red arrows mark thermal expansion

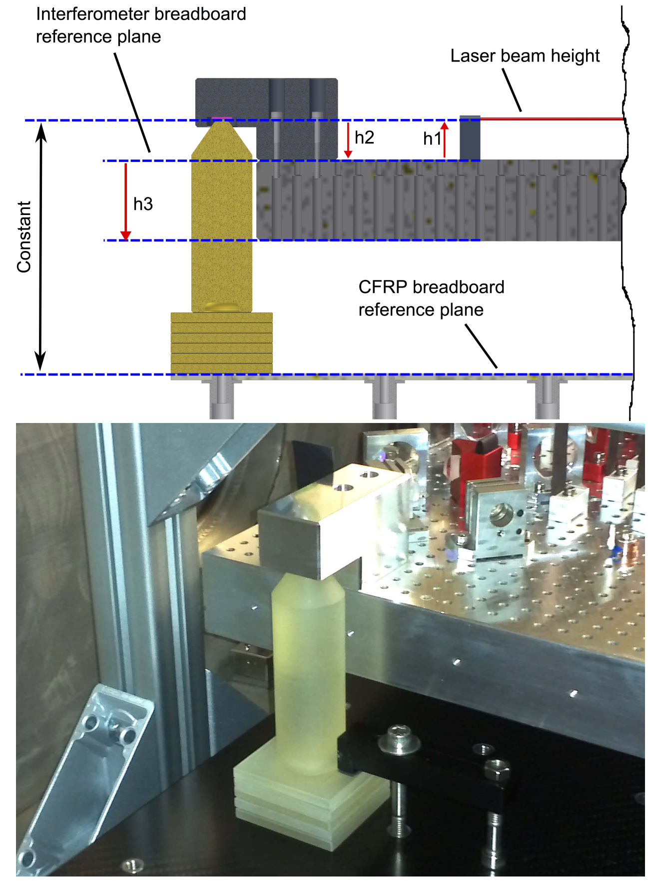

Figure 3.17.: Upper: thermal neutral support of the interferometer breadboard. Lower: photograph of one of three feet of the interferometer support.

axes. The interferometer breadboard has no influence because it is mounted on its top surface and therefore expands downwards (h3 in the schematic). In addition, the expansion of the fiber mounting (h1) equals the one which is caused by the section of the adapter from the top of the Zerodur foot to the interferometer breadboard reference plane (h2), (h1=h2). The CTE of the Zerodur feet compared to the CTE of the aluminum is approximately 1000 times smaller.

In order to prevent a creep of the Aluminum on the point of contact between the Zerodur feet and the adapter, a small plate made of Sapphire (colored pink in Figure 3.17) was bonded where the two materials are compressed. The first shim is bonded to the Zerodur foot. For stability reasons a small cavity on the bottom side of the Zerodur foot was realized. This leads to a circular contact area that provides a circular adhesive surface (better adhesive distribution). The resulting stress due to the vacuum environment (ambient pressure in the cavity) was not critical. A photograph of one Zerodur foot of the support is presented in Figure 3.17.

These components were placed on a mutual surface area in order to realize a high stability between the Aluminum breadboards, interferometer and sample support. Any additional effects should be common-mode to the interferometer and the sample. Therefore it was envisaged to use a vacuum compatible breadboard with high thermal and mechanical stability, with dimensions of 900 mm×600 mm. As a possible solution, a standard optical Stainless Steel breadboard, an optical breadboard made of CFRP and a custom breadboard made of massive Invar were considered. Aluminum was discarded due to its poor thermal stability. The CFRP breadboard from Carbon Vision model CAI was chosen, mainly because of the excellent, thermal and mechanical stability, the excellent damping properties and the low weight. Carbon Vision quoted CTE values of the CFRP breadboard in x and y direction (lateral) of $2.5 \cdot 10^{-6}\,1/\mathrm{K}$ and in z direction of $0.5 \cdot 10^{-6}\,1/\mathrm{K}$ at $T = 273\,\mathrm{K}$. Conventional Aluminum CTE properties are higher by a factor of 10 in lateral direction and by a factor of 50 in z direction.

To minimize vibrations on the interferometer and the sample support coming from the pulse tube cooler and of the turbo pump, the CFRP breadboard is mounted on three mechanical vibration isolators (model VIB320-3775 from Newport) providing both vertical and horizontal isolation from 16.8 kg to 34.1 kg with a vertical resonance frequency of 6.8 Hz, with an amplification factor of approximately 8, and a horizontal resonance frequency of 6.3 Hz with an amplification factor of approximately 6. Unfortunately, the highest vibration source of the pulse tube cooler is at around 1 Hz where the isolators do not have any significant effect. Vibrations of the turbo pump which are introduced by the rotation speed of 1500 Hz are damped with approximately 40 db according to the suppliers specifications.

3.3.2. Thermal system (B) for low temperatures

The goal was to reach temperatures where many satellites and their instruments operate. For example, the LISA telescope will operate at around 203 K [2, 3] and its optical bench near room temperature, 300 K [4]. To cover a temperature range between 140 K and 300 K a cooling set-up was necessary. For this purpose several cooling techniques can be applied. A common method is the bath cryostat, where e.g. liquid Nitrogen is used to cool down the device under test. In our set-up, a controlled temperature was necessary. A closed-cycle cryostat offers a very easy operation, therefore a pulse tube cooler from TransMIT was chosen. The so-called pulse tube cooler model PTS 8030 offers a cooling power of 30 W at 80 K and reaches a minimum temperature around 35 K at its cold head after 25 minutes with very low noise [54]. This cold head works based on the McMahon principle using a Helium compressor. The low noise is necessary for our set-up to reach precise expansion measurements. The only moving part is the rotary valve which is connected to the cold head by a flexible tube.

The pulse tube cooler is mounted with a DN 200 ISO-K T-adapter to the vacuum chamber (see Figure 3.18). Two Copper bars are mounted at the cold head to have a heat transfer from the cooling vessel surrounding the sample. All Copper joints are made such that they are adjustable in one dimension to place the Copper vessel very precisely over the sample support. M6 screws and Helicoils (threaded inserts) are used to mount all highly thermally stressed parts together. The main characteristic of the Helicoils is that they can compensate temperature driven load changes due to materials with different CTE, so that an optimum force transmission from the screw to the thread can be achieved.

To increase the efficiency of the heat diffusion, thin Pyrolytic Graphite interface sheets (PGS EYGA121807A) with high thermal conductivity of 950 W/(m·K) were placed between the screwed parts. This 0.07 mm thick sheet is highly flexible and improves the contact surface of the two parts where the Graphite sheets are attached to. This is used as a clean and efficient alternative to thermal grease.

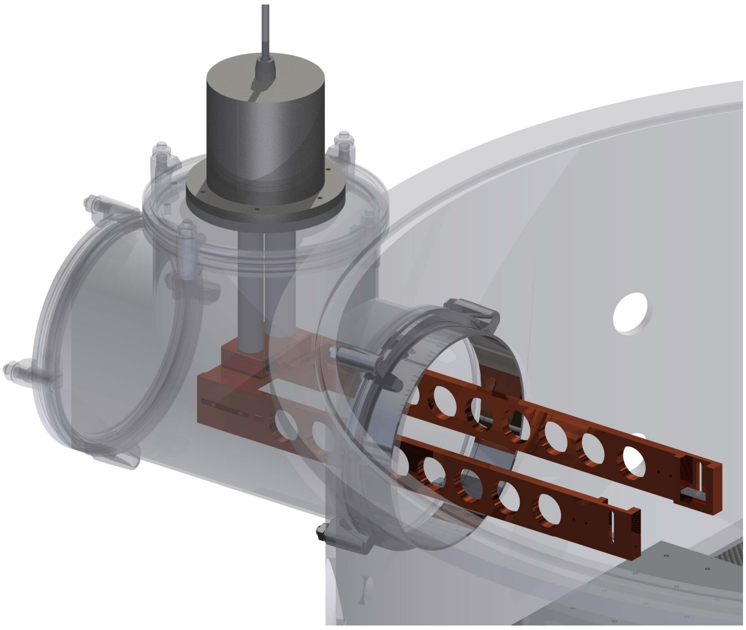

Figure 3.18.: Pulse tube cooler flanged with a T-adapter and heat pipes mounted to the cold head.

On the other end of the two Copper bars, a Copper vessel can be mounted to surround the cylindrical sample (see Figure 3.19). The cylindrical vessel has a diameter of 112 mm and and a inner clearance height of 146 mm. At the top and the bottom, a Copper disk is mounted with 18 screws to the vessel to ensure a large contact area for the heat transfer. The bottom disk also has four holes in the middle where the laser beams go through to the sample and three smaller holes where the sample support holds the device under test without any contact between the Copper vessel and the sample support. The outer side of the vessel is mounted with two M6 screws to the Copper bars and can be adjusted in height with four set screws.

All parts at the pulse tube cooler and all connected parts which are in the vacuum chamber are covered with a MLI (multi layer insulation) foil in order to minimize direct radiation to the interferometer and to keep it at room temperature.

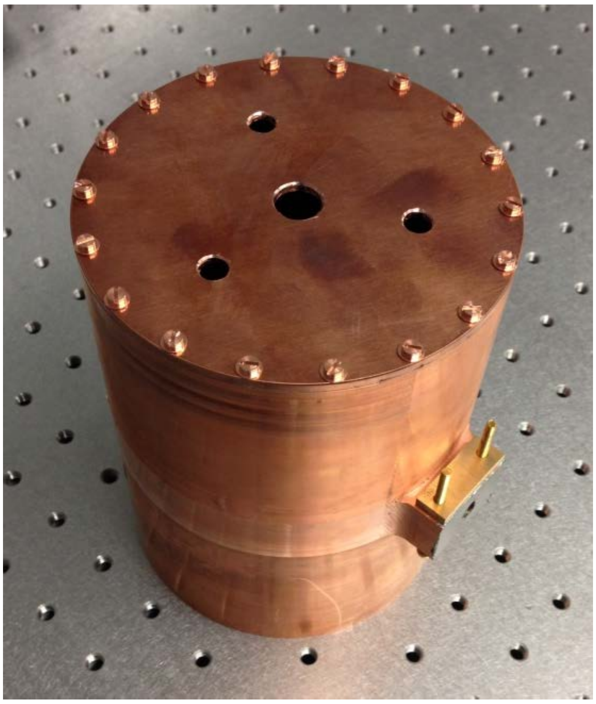

Figure 3.19.: Heating chamber, bottom up where the holes for the laser beam and for the sample support are shown.

3.3.3. Temperature control of system (B)

The temperature control is done by two heating stages: (1) one control loop with a heating resistor at the cold head and (2) a second control loop with two heating resistors at the Copper bars near the Copper vessel surrounding the sample (see Figure 3.20). Pt-100 sensors were placed next to the heating resistors to provide an input signal to the control loop. A two-channel configurable PID controller from Lake Shore Cryotronics, model 335 with a maximum output power of 50 W of channel 1 and 25 W of channel 2, is used and its temperature setpoints are provided by a LabVIEW program. The controller is configured as a PI controller and is tuned experimentally. The cold head cools down with a constant power of $\approx$30 W and the controller heats it up with an electric heater to the set constant temperature, T1. T1 is approximately 10 K lower than the mean temperature of the Copper vessel, T2. At the Copper vessel, the second controller provides a sinusoidal temperature change with an amplitude of several Kelvin with a period between three to five hours. To adjust the period to the sample, the phase difference between the temperature of the sample and the expansion of the sample is considered. The period of the temperature signal is increased as long as the phase difference is minimized. The parameters for the temperature signal depend on the material and sample dimensions.

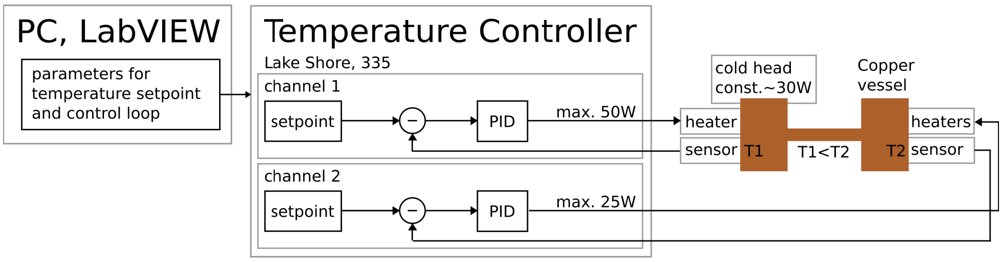

Figure 3.20.: Control loop of the thermal system (**B**). The cold head has a constant cooling power of ≈ 30 W. Channel 1 of the temperature controller controles the temperature directly at the cold head. Channel 2 controls the temperature of the copper vessel covering the sample.

To minimize the heat transfer to the Pt-100 sensor from the wires, Copper anchors were used to wrap approximately 10 cm around the Copper cylinder before mounting it to the measurement point (see Figure 3.21 (a)). At locations where the Copper anchors could not be used, e.g. at the sample, little coils of twisted pair wires were placed (see Figure 3.21 (b)) around the sensor to minimize the heat transfer from outside the thermal system [55]. On the outer side of the sensor, an Aluminum tape reflects the radiation to maximize the heat transfer from the other side of the sample to the sensor.

3.3.4. Optical set-up

A photograph of the the interferometer of set-up (**B**) is shown in Figure 3.22. It shows more complexity in the set-up than the principle in Section 3.1.1. The whole optical set-up was designed and built within this thesis. The additional steering optics were incorporated to enable a better adjustment of the laser beam for the dilatometer application. The piezo mirror mounts in the upper side of the interferometer board enable the external adjustment of the

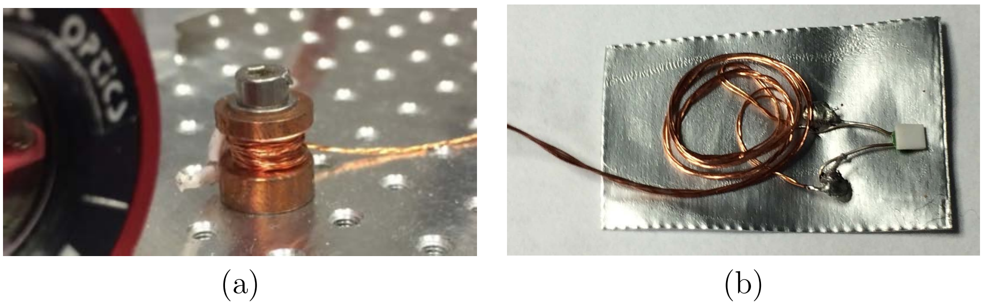

(a) (b)

Figure 3.21.: (a) Copper cylinder and (b) Aluminum tape where a Pt-100 sensor is glued to and the leads are twisted around to minimize the error due to the heat transfer of the Copper wires.

laser beams to the sample from outside the evacuated vacuum chamber (see Figure 3.22). In case the pointing of these beams changes due to temperature changes or pressure changes, the laser beams can be readjusted in four degrees of freedom to improve the interferometer alignment prior to the measurement campaign. Additional mirrors enable better alignment and overlap of the laser beams, f_1 and f_2.

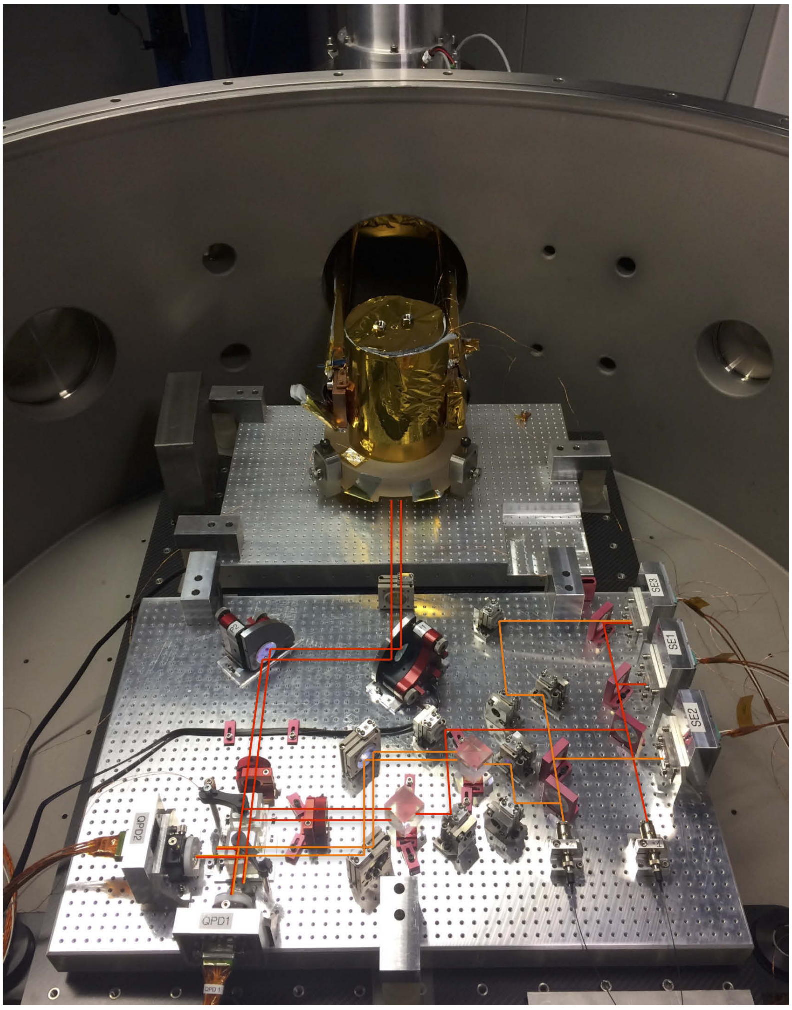

Figure 3.22.: Photograph of the optical set-up (**B**) for CTE measurements at low temperatures and the drawn beam paths.

4. CTE metrology system verification and uncertainty analysis

In this chapter, different measurements concerning tube shaped samples are used to verify the CTE metrology system and develop an uncertainty budget. The main limitation of the measurements has been identified to be the tilt of the sample and was published in Reference [56]. In Section 4.1, the tilt coupling of the sample is investigated. This tilt affects the expansion measurement and is also called tilt-to-length (TTL) coupling.

In Section 4.2, CTE measurements of Zerodur and Clearceram samples with set-up (**A**) at room temperature are presented.

A detailed discussion on the noise sources of set-up (**B**) is provided in Section 4.3. CTE measurements of a Zerodur sample at room temperature and CTE measurements of a CFRP sample from 140 K to 250 K were conducted and a detailed uncertainty analysis was done to verify the CTE metrology system.

4.1. Tilt-to-length error contribution

The same sample support was used for all CTE measurements with set-up (**A**) and set-up (**B**). Therefore, in both cases, the error contribution is the same. If the sample tilts such that one beam has to travel more than the other without any expansion, the measured length change leads to an error. Figure 4.1 summarizes the TTL coupling mechanisms in our set-up.

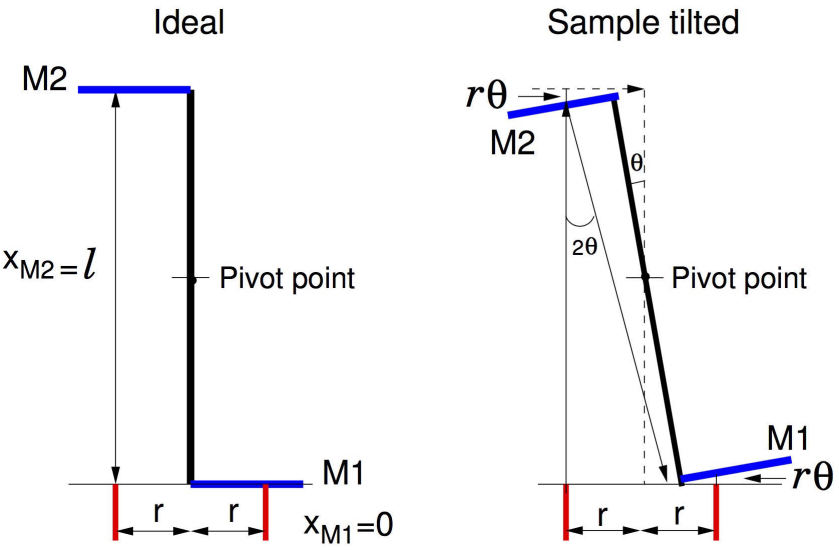

Figure 4.1.: TTL coupling. Left: ideal case. Right: sample holder tilted by θ. As shown in Equation (4.6) the piston effect dominates the error.

In general, the distances are

$$\begin{aligned} x_{\mathrm{M1}} &= \frac{1}{2}\left[r\tan\theta - \frac{\ell}{2}(\tan\theta\sin\theta + \cos\theta - 1)\right] \\ &\quad \cdot \left[1 + \frac{1}{\cos 2\theta}\right] + f(M_1) \qquad (4.1) \\ x_{\mathrm{M2}} &= \frac{1}{2}\left[-r\tan\theta + \frac{\ell}{2}(\tan\theta\sin\theta + \cos\theta + 1)\right] \\ &\quad \cdot \left[1 + \frac{1}{\cos 2\theta}\right] + f(M_2) \qquad (4.2) \end{aligned}$$

where $f(M_1)$ and $f(M_2)$ represent the independent tilt of the mirrors M1 and M2, respectively. These are considered in a general form since their pivot points are unknown. θ is the tilt of the sample around its center and r stands for the distance between the pivot point (point where the sample tilts) and the beams.

The signal of interest is $\Delta x = x_{\mathrm{M2}} - x_{\mathrm{M1}}$, where

$$\begin{aligned}\Delta x_{\mathrm{ideal}} &= \ell && (4.3)\\ \Delta x_{\mathrm{tilt}} &= \left[-r\tan\theta + \frac{\ell}{2}\left(\tan\theta\sin\theta + \cos\theta\right)\right] \\ &\quad\cdot\left(1 + \frac{1}{\cos 2\theta}\right) + f(M_2) - f(M_1), && (4.4)\end{aligned}$$

and the error due to the tilt is given by $\epsilon_{\mathrm{tilt}} = \Delta x_{\mathrm{real}} - \Delta x_{\mathrm{ideal}}$, which can be expressed as follows for small angles to

$$\epsilon_{\mathrm{tilt}} \simeq -2\theta r + f(M_2) - f(M_1). \quad (4.5)$$

Fluctuations of this error term can be expressed by its differential:

$$\delta\epsilon_{\mathrm{tilt}} \simeq 2r\delta\theta + [\delta f(M_2)^2 + \delta f(M_1)^2]^{1/2}, \quad (4.6)$$

where the tilt functions for M1 and M2 are assumed to be uncorrelated.

The uncertainty in the CTE is dominated by the TTL error as detailed in Section 4.3.5 Paragraph "CTE determination and uncertainty analysis". Its effect has also been quantified by measuring the tilt of the mirror M2, which is representative of the total error (see Section 4.3.5 Paragraph "Tilt-to-length coupling"). This assumption is valid as far as the term $2r\delta\theta$ dominates in Equation (4.6). The TTL coupling measurement includes

$$k = \frac{dx}{dT} + \frac{df(M_2)}{dT} = 2r\frac{d\theta}{dT} + \frac{df(M_2)}{dT}, \quad (4.7)$$

and our assumption holds as long as

$$\begin{aligned}2r\frac{d\theta}{dT} &\gg \frac{df(M_2)}{dT} && (4.8)\\ \frac{df(M_1)}{dT} &\simeq \frac{df(M_2)}{dT}. && (4.9)\end{aligned}$$

Four measurements using a Zerodur sample tube have been performed to validate Equation (4.8): (i) mirror M2 was held by the mirror mount shown in

Figure 3.6, i.e., the same way as in the TTL coupling and CTE measurements; (ii) a Zerodur mirror was held by a spring-loaded mount; (iii) M2 was held by the Invar ring holder that usually holds the sample; and (iv) a Fused Silica mirror was placed on the sample holder but without the 3-point Invar ring (see Figure 4.2).

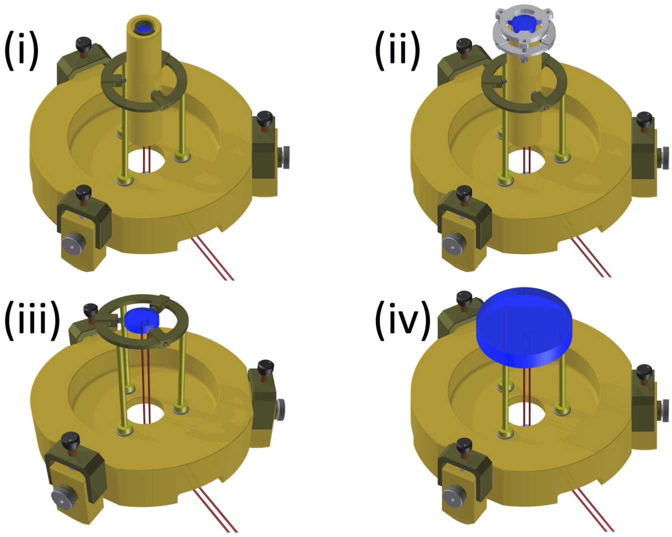

Figure 4.2.: Configurations to test the TTL coupling of the sample holder and mirrors.

The results are summarized in Table 4.1 and show that, regardless the type of mirror mount used, the TTL coefficient is around $5\,\mathrm{nm\,K^{-1}}$. The set-up without the Invar ring (iv) yields $k = 0.1\,\mathrm{nm\,K^{-1}}$. The assumption in Equation (4.8) is met since the Invar ring (sample holder) is responsible for most of the TTL error contribution. The second assumption, Equation (4.9), is considered plausible because M1 and M2 are mounted the same way. The results given in Table 4.1 were taken at 307 K. The coefficients k at low temperatures (140 K to 250 K) are also in same range and denote the same origin. The TTL coupling coefficient k is multiplied by the temperature variation ΔT and contributes an error $\Delta\ell$ to the CTE error budget.

Table 4.1.: TTL coupling coefficients for different configurations at 307 K.

Conf.	k
(i)	$5.9\,\mathrm{nm\,K^{-1}}$
(ii)	$5.3\,\mathrm{nm\,K^{-1}}$
(iii)	$5\,\mathrm{nm\,K^{-1}}$
(iv)	$0.1\,\mathrm{nm\,K^{-1}}$

4.2. Measurements with set-up (A)

In this section, first CTE measurements at room temperature with set-up (**A**), the dilatometer at Airbus DS GmbH in Friedrichshafen, are presented, which were taken to verify the experiment.

4.2.1. CTE measurements of a Zerodur sample and coupling of laser frequency noise

First measurements were done with an existing interferometer at Airbus DS GmbH in Friedrichshafen and were published in Reference [47]. This heterodyne interferometer set-up had a sensitivity below $2\,\mathrm{pm}\sqrt{\mathrm{Hz}}$ in translation and $10\,\mathrm{nrad}/\sqrt{\mathrm{Hz}}$ in tilt at frequencies $> 10^{-1}\,\mathrm{Hz}$ up to approximately 5 Hz [46]. The schematic of the optical set-up is described in Section 3.2.1. For this first measurement the laser source was not frequency stabilized.

The optical pathlengths of both arms are not equal, making the set-up non-symmetric. The distance between the reference mirror and the measurement mirror is 100 mm. In ultra precise measurements, the frequency noise (Δf) of the laser appears in the translation ($\Delta\ell$) measurement of unequal arm-length interferometers (frequency noise to length coupling) as:

$$\Delta\ell = \frac{\lambda}{c} \cdot z \cdot \Delta f\,, \tag{4.10}$$

where λ is the laser wavelength, 1064 nm, c is the speed of light and z the distance between the two mirrors. The laser frequency noise (Δf) is detected by measuring the beat note of the dilatometer laser and a laser which is stabilized to a cavity by the Pound-Drever-Hall technique [57]. The cavity stabilization is explained in Appendix B.1. Due to measurement tolerances of the interferometer geometry a mismatch of <3% was measured between the experimentally obtained value, $\frac{\lambda}{c} \cdot z$ of 0.355 nm/MHz, and the expected on, 0.345 nm/MHz. To validate the dilatometer set-up, we measured the CTE of a Zerodur sample with an ultra low coefficient of thermal expansion.

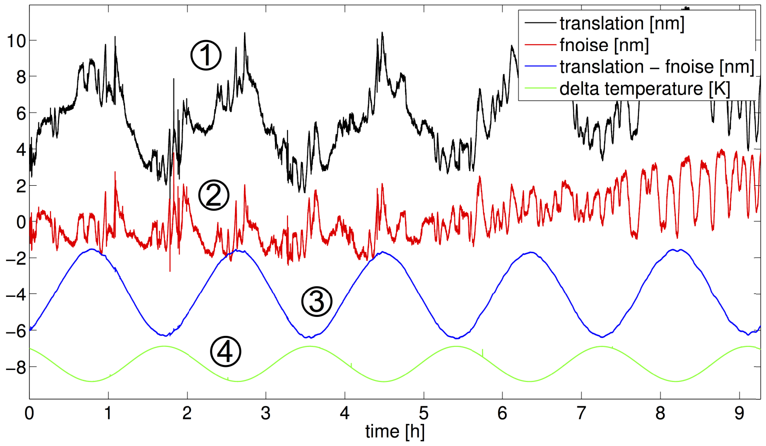

Figure 4.3.: An expansion measurement of a Zerodur sample tube. Upper to lower curve: (1) translation; (2) frequency noise (fnoise) converted to nm; (3) translation − frequency noise; (4) temperature variations around 30°C.

A CTE measurement of a Zerodur sample is shown in Figure 4.3 and was the first attempted to verify the dilatometer set-up. The CTE is calculated with $\alpha = \Delta\ell/\ell \cdot \Delta T^{-1}$ where $\Delta\ell$ is the measured expansion of the material, ℓ the length of the sample, 100 mm and ΔT the measured temperature variation. A sinusoidal temperature variation with a period of 2 h was applied to the sample. Pt-100 platinum resistance temperature sensors, enabling a high accuracy over a wide temperature range, were used to measure the temperature at the sample: 30°C ± 1.34°C. The small and slow temperature variations enable a homogenous temperature over the whole sample. The displacement between the reference mirror and the measurement mirror was measured and is shown in the translation curve (see Figure 4.3 trace (1)). The large noise in the measurement is caused by laser frequency noise (see Figure 4.3 trace (2)) which shows up due to the unequal arm-length interferometer. To measure the laser frequency noise, a beat signal between the measurement laser and a reference laser that was locked to a cavity was recorded simultaneously. The coefficient of 0.355 nm/MHz (see Equation 4.10) was calculated out of the difference in pathlength of the measurement arm and reference arm. After subtracting the laser frequency noise from the measured translation, it is possible to reconstruct the sinusoidal expansion of the sample, as expected (see Figure 4.3 trace (3)). The phase difference of 180° between the expansion of the sample and the temperature was confirmed in an additional systematic test of our measurement set-up, where a positive expansion was simulated, obtaining thus a negative sign to the CTE value. The amplitudes of the two signals, $\Delta\ell$ and ΔT (see Figure 4.3 trace (4)) are results of a sinusoidal fit to the measured signals. The distance between the two mirrors, ℓ, was measured with a caliper in this case. The measured CTE of the Zerodur sample is $-1.74{\cdot}10^{-8}\,\mathrm{K}^{-1}$. The vendor Schott quotes a CTE value of $0 \pm 3 \cdot 10^{-8}\,\mathrm{K}^{-1}$ [58].

The goal of this measurement was to show the functionality of the dilatometer and to verify the CTE value given by the manufacturer.

4.2.2. CTE measurements of a Clearceram sample

For comparison, a sample of Clearceram from Ohara was measured. The same set-up was used, however, in this case the dilatometer laser was locked to a cavity (see Appendix B.1) in order to reduce the frequency noise to length coupling. The CTE measurement of a Clearceram-Z HS sample is shown in Figure 4.4. A CTE value of $-3.205 \cdot 10^{-8}\,\mathrm{K}^{-1}$ with a standard deviation of $0.039 \cdot 10^{-8}\,\mathrm{K}^{-1}$ is obtained with the peak to peak values of a sinusoidal fit to the translation signal (5.32 nm) and the temperature signal (1.6 °C around 29 °C) and with the length of the sample of 104 mm. A CTE of $0 \pm 2 \cdot 10^{-8}\,\mathrm{K}^{-1}$ is mentioned by the manufacturer Ohara. [59]

The systematic error of the tilt-to-length coupling of 0.55 nm/K was determined from TTL measurements in Section 4.1. This error dominates the uncertainty budget and raises the error to $(-3.205 \pm 0.57) \cdot 10^{-8}\,\mathrm{K}^{-1}$. Therefore, the resulting disagreement between the CTE value given by the manufacturer and our measurements is approximately $0.6 \cdot 10^{-8}\,\mathrm{K}^{-1}$.

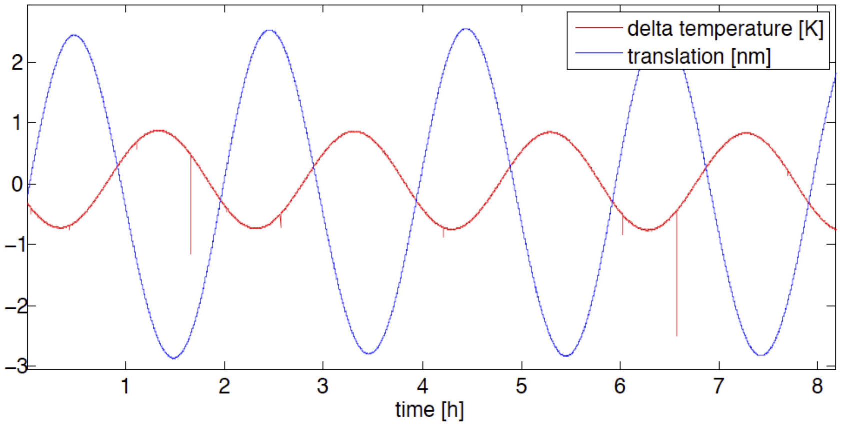

Figure 4.4.: An expansion measurement of a Clearceram-Z HS sample tube. The blue curve (with larger amplitude) shows the measured expansion in nm of the sample and the red curve (with smaller amplitude) the corresponding temperature around 29°C. The measured CTE is $-3.205 \cdot 10^{-8}\,\mathrm{K}^{-1}$ with a standard deviation of $0.039 \cdot 10^{-8}\,\mathrm{K}^{-1}$.

4.3. Measurements with set-up (B)

4.3.1. Noise floor of the optical system

Measurements were conducted to characterize the noise floor of this set-up. Figure 4.5 shows LSDs (linear spectral density) measurements of the interferometer with different set-ups. The purple curve is measured with a free-running interferometer, where the two beams are reflected off one single mirror on the optical bench. The green curve shows a measurement with exactly the same optical set-up, but having the laser frequency stabilized to a molecular Iodine transition. The Iodine reference is described in Appendix B.2. The blue trace shows a measurement with active stabilizations for the laser power and the optical pathlength difference. Power and phase of the two beams are measured at the optical bench and controlled by a FPGA, using the applied input power to the AOMs, and a piezo actuator, respectively. The detailed optical set-up is described in Section 3.1.1. The noise floor drops slightly between $4 \cdot 10^{-4}\,\mathrm{Hz}$ and $1\,\mathrm{Hz}$ where the phase stabilization is the main improvement. The red trace shows almost the same noise than the blue trace. Here, the optical set-up is changed to test the dimensional stability of the interferometer board compared to the sample support. Therefore a mirror with a three inch diameter was put on the Zerodur sample support to measure the noise contribution of the sample support, which does not change significantly.

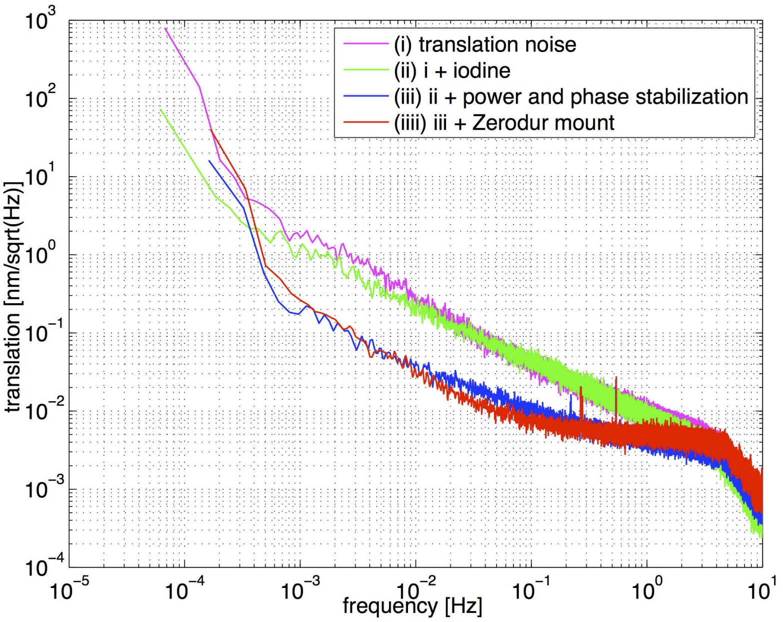

Figure 4.5.: Different noise floors of the translation measurements. For the purple, green and blue trace, the two laser beams of the interferometer are reflected off at one single mirror on the optical bench with different control set-ups. The red trace is measured with all stabilization set-ups and the additional optical path to sample support.

This measurements show that the noise floor of the optical system is good enough to measure below the nm-range at frequencies above $4 \cdot 10^{-4}$ Hz, enabling an accuracy of $\approx 10\%$ for a $0.1\,\mathrm{m}$ long ultra low expansion material (CTE in the $10^{-8}\,\mathrm{K}^{-1}$ range, like Zerodur) with temperature variations of $1\,\mathrm{K}$. In post-processing, a straight line should be obtained when the temperature is plotted against the expansion. The residual of the measurement gives the uncertainty of the measurements $\Delta\ell$ and ΔT.

4.3.2. Sign calibration of expansion measurement

Materials can have the property of positive or negative CTE values. This property of the expansion measurement is calibrated in this section. The sample and the mirror mounts are prepared such that always the same beam is reflected at the same mirror in the sample, one beam is reflected at the upper mirror (M2) and the second beam at the lower mirror (M1) (see Figure 4.6 left). A calibration was done to check if the measured signal shows the correct sign of the translation, contraction or expansion of the sample. To this end, a glass plate was mounted at a 45° angle such that only one beam would go through.

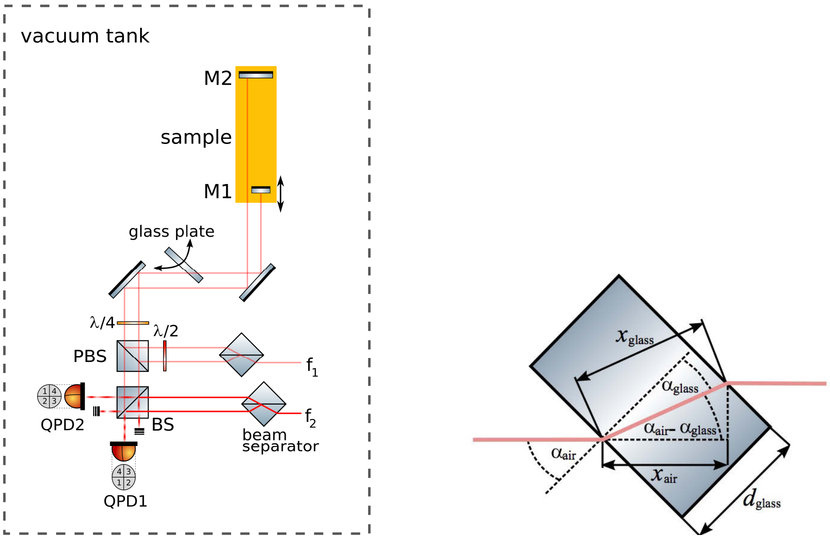

Figure 4.6.: Left: Schematic of the interferometer set-up with additional tilting glass plate for sign calibration, right: schematic and detailed beam trace in the glass plate due to the different refraction index of glass and air.

If the glass plate is turned slightly and the light sent to M1 travels a longer path in the glass plate due to the different refraction index of glass and air a contraction of the sample is simulated by longer distance in the glass plate. In Figure 4.6 a schematic outlines the beam paths in the glass plate. The change in pathlength (Δ_l) can be described as

$$\Delta_l = d_{glass}(n_{glass} - \cos(\alpha_{air} - \alpha_{glass}))/\cos(\alpha_{glass}), \tag{4.11}$$

where α_{glass} is

$$\alpha_{glass} = \arcsin\left(\frac{n_{air} \cdot \sin(\alpha_{air})}{n_{glass}}\right). \tag{4.12}$$

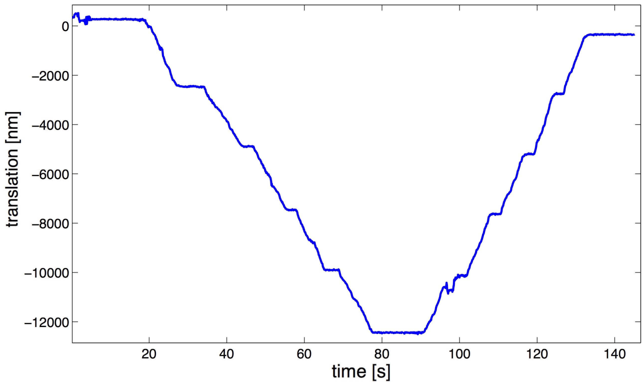

Figure 4.7.: Measurement of the sign calibration, first the angle of the glass plate was changed in one direction resulting in 2.045° (five steps) followed by a five steps back.

A measurement is shown in Figure 4.7 where the glass plate was mounted to a mirror holder and turned stepwise starting in an angle of $\alpha_{air} = 45°$. The screw at the mirror mount for the horizontal adjustment was turned five times, as evidenced in the measurement graph by five steps. First, the angle α_{air} was increased resulting in a negative translation or in a simulated contraction which is the correct sign, because the optical path in the glass plate was increased. This corresponds to a movement of M1 towards M2. The five turns of the mirror mount screws (Thorlabs, Polaris Ø1 inch) result in a 2.045° tilt, according to the fine thread properties and the dimensions of the mount. The calculated Δ_l for a starting angle of 45° is 13 351 nm and the measured translation in 12 752 nm. The difference of <5% leads to a misalignment of the original 45° position of the glass plate.

4.3.3. Temperature measurements

Up to 12 temperature measurement points are recorded simultaneously during a CTE measurement. The most important ones are three measured directly at the sample. In Section 3.1.2 Figure 3.5 a photograph of the sample support and the sample with these three positions is shown. In addition, several temperatures are recorded inside and outside of the vacuum chamber (e.g. Zerodur sample support, interferometer, thermal chamber, room temperature).

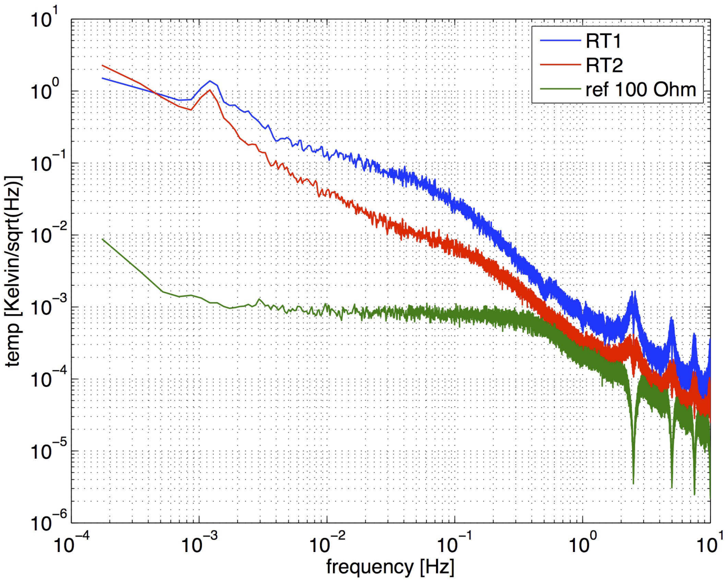

Figure 4.8.: 16 hour LSD measurement of the noise floor of the Lake Shore 224 temperature monitor. Green: the noise measured with a 100 Ω resistor at the input; blue and red are Pt-100 sensor connected to the temperature monitor at two different spots in the lab with running air condition.

A temperature monitor system from Lake Shore Cryotronics model 224 was used for these measurements. This system has 12 temperature sensor inputs for 4-wire sensing with a measurement resolution of 2 mΩ. In combination with Pt-100 sensors an electronic accuracy of ±0.004 Ω ± 0.01%, is achieved between 0 Ω and 300 Ω at 25°C ambient temperature, as quoted by the vendor. This means that at 273 K (0°C) an error of ±0.04 K can be expected. In addition, the noise level of the temperature monitor was measured connecting a 100 Ω resistor, which has a minimal temperature dependency compared to the Pt-100 sensor. A LSD of this 16 hour measurement is shown in Figure 4.8. The green trace shows the temperature monitor at frequencies above 10^{-3} Hz, reaching a level of 1 mK. The blue and red curves show the behavior of a temperature measurement.

All temperature sensors are platinum (Pt-100) sensors from Innovative Sensor Technology model P0K1.161.6W.Y.010. This sensors meet the requirements of DIN EN 60751 Klasse F0.1, meaning that the sensor has an uncertainty of $\epsilon_{T_{abs}} = 0.1 + 0.0017 \cdot |T - 273.15\,\mathrm{K}|$. Relative errors are observed as noise in the temperature measurement and the absolute error has to be considered in the CTE measurement (see Section 4.3.5 Paragraph "$\Delta\ell$ and ΔT measurements").

To eliminate the lead and contact resistance, all temperature sensors are monitored by the 4-wire sensing method. In air, regular twisted pair cables are used. Self-made twisted pair cables made of 0.15 mm diameter Copper wires with a polyurethane insulating varnish (model: Block CUL 200/0,15) are used in vacuum.

4.3.4. CTE measurements of Zerodur at room temperature

This measurement was done to compare our measurements with data provided by the vendor Schott of a Zerodur sample. Schott is measuring the CTE of its materials using a push-rod dilatometer. For our tests, they provided a sample which was made of the same piece of material as the one they characterized. Their measurement procedure is different than ours, as they start at a constant temperature of 0°C and rise the temperature in three plateaus up to 50°C. The plateaus are, as far as they can determine, at a static temperature in the sample before they continue with a constant temperature rate to the next temperature plateau. For the CTE determination, the expansion between the plateaus is measured. For the temperature values between those plateaus, Schott uses an empirical model, where they adjust the parameters to the manufactured material and they calculate the CTE values from this model (see Table 4.2).

Table 4.2.: Comparing the vendors ($\mathrm{CTE_{Schott}}$) and our ($\mathrm{CTE_{DLR}}$) CTE results of a Zerodur sample.

T [K]	$\mathrm{CTE_{Schott}}$ [$\mathrm{K^{-1}}$]	$\mathrm{CTE_{DLR}}$ [$\mathrm{K^{-1}}$]	CTE difference [$\mathrm{K^{-1}}$]
297	$-5.4 \cdot 10^{-9}$	$13.91 \cdot 10^{-9}$	$19.13 \cdot 10^{-9}$
301	$-9.7 \cdot 10^{-9}$	$13.88 \cdot 10^{-9}$	$23.58 \cdot 10^{-9}$
305	$-15.0 \cdot 10^{-9}$	$12.26 \cdot 10^{-9}$	$27.26 \cdot 10^{-9}$
310	$-20.0 \cdot 10^{-9}$	$10.01 \cdot 10^{-9}$	$30.11 \cdot 10^{-9}$
315	$-25.2 \cdot 10^{-9}$	$6.29 \cdot 10^{-9}$	$31.29 \cdot 10^{-9}$
321	$-29.9 \cdot 10^{-9}$	$-5.49 \cdot 10^{-9}$	$24.41 \cdot 10^{-9}$

The CTE measurement values are determined by our set-up (**B**) with the heating device using Peltier elements (TECs) for controlling the temperature around room temperature (see Section 3.2.2). The measurements where done by cycling the temperature around a nominal measurement point T (see Table 4.2 first column). As an example, a sinusoidal temperature variation ΔT of 1.6 K around 305 K, and 3.7 K around 321 K with a period of approximately 4 hours was applied to the sample.

For these measurements, the CTE is obtained by a least squares method as follows:

$$\alpha = \frac{1}{\ell} \cdot \frac{\sum \Delta T(t) \cdot \Delta\ell(t)}{\sum \Delta T(t)^2}, \tag{4.13}$$

where ℓ is the length of the sample, $\Delta T(t)$ is the temperature and $\Delta\ell(t)$ is the expansion of the measurements. This least squares method is equivalent to a regression analysis, plotting $\Delta\ell(t)$ as a function of $\Delta T(t)$, where the slope represents the CTE. The 1-sigma error of the fit ϵ_{ls} can be calculated from its residual. In this example, $\epsilon_{ls} = 49 \cdot 10^{-12}\,\mathrm{K}^{-1}$.

The total error bar can be calculated as

$$\begin{aligned}
\epsilon_\alpha &= \alpha \cdot \left(\frac{\epsilon_\ell}{\ell} + \frac{\Delta T \cdot k}{\Delta\ell}\right) + \epsilon_{ls} && (4.14)\\
\epsilon_\alpha &= 12.26 \cdot 10^{-9}\frac{1}{\mathrm{K}} \cdot \left(\frac{20\,\mu\mathrm{m}}{106.5\,\mathrm{mm}} + \frac{1.636\,\mathrm{K} \cdot 0.55\,\frac{\mathrm{nm}}{\mathrm{K}}}{2.198\,\mathrm{nm}}\right) + \epsilon_{ls} && (4.15)\\
\epsilon_\alpha &= 5.07 \cdot 10^{-9}\frac{1}{\mathrm{K}}, && (4.16)
\end{aligned}$$

where ϵ_ℓ is the error in the length measurement, ℓ is the length of the sample, and k is the tilt-to-length (TTL) coupling coefficient. The TTL error is the main contributor to the error budget and it is almost two orders of magnitude higher than the other contributions. At lower CTEs, the error bars increase due to the experimentally determined TTL error coefficient.

By comparing the model values and the measurements, an offset between $19.13 \cdot 10^{-9}\,\mathrm{K}^{-1}$ and $30.11 \cdot 10^{-9}\,\mathrm{K}^{-1}$ can be seen, which leads to an additional systematic error in one of the dilatometer set-ups.

4.3.5. CTE measurements of a CFRP sample from 140 K to 250 K

In this section the CTE of a CFRP sample is determined to show the performance of our dilatometer in the temperature range of 140 K to 250 K [56]. For all measurements we use sinusoidal signals as main modulation since they are easy to generate and they are relatively simple to analyze in the time and frequency domains, because they do not have discontinuities or high energy at higher harmonics like square-wave type signals.

Absolute length measurement Applying the method explained in Section 3.1.1 the absolute length, ℓ, is measured. To this end, the temperature is kept constant within 10 mK over the whole measurement time ($\approx$ 1 hour). The laser frequency, $\nu_0 = 281.630\,\mathrm{THz}$, is modulated by a sinusoidal signal with an amplitude $\Delta\nu_{\text{0-pk}} = 1.7\,\mathrm{GHz}$, and a period of $\tau = 100\,\mathrm{s}$, over a total time of 700 s, i.e.,

$$\nu(t) = \nu_0 + \Delta\nu \sin(2\pi t/\tau). \tag{4.17}$$

These parameters are the results of a trade-off between generating a large signal to maximize the signal-to-noise ratio, while maintaining small enough errors in $\Delta\nu/\nu_0$, and avoid laser mode-hops. Figure 4.9 shows the measurement at 223.48 K where $\Delta\ell\nu_0$, is plotted as a function of $\Delta\nu$. The slope corresponds to the absolute length ℓ. The linear fit to the data yields $\ell = 0.0873946\,\mathrm{m}$

and $\sigma_{\ell,\,\mathrm{fit}} = 4.2 \cdot 10^{-6}\,\mathrm{m}$. The total uncertainty is given by

$$\sigma_\ell \simeq [\sigma^2_{\ell,\,\mathrm{fit}} + \frac{\ell^2}{\nu_0^2}(\Delta\nu^2 + \epsilon_\nu^2)]^{1/2} \simeq \sigma_{\ell,\,\mathrm{fit}} = 4.2 \cdot 10^{-6}\,\mathrm{m}, \tag{4.18}$$

where $\epsilon_\nu = 600\,\mathrm{MHz}$ is the accuracy of the wavelength-meter (High-Finesse WS6-600). The term $\sigma_{\ell,\,\mathrm{fit}}$ dominates the error and results from the interferometer noise ($\simeq 1\,\mathrm{nm}$) and wavelength-meter noise ($\simeq 10\,\mathrm{MHz}$), totaling $\simeq 2.5\,\mathrm{nm}$. Finally, the effect of the temperature variations is estimated as $\ell\alpha\delta T$, since they cause expansions/contractions of the sample. Anticipating the results given in Section 4.3.5 Paragraph "CTE determination and uncertainty analysis", that $\alpha \simeq 7 \cdot 10^{-7}\,\mathrm{K}^{-1}$, $\ell = 0.087\,\mathrm{m}$ and $\delta T = 10\,\mathrm{mK}$. This yields an uncertainty of 0.6 nm, which is well below the limiting noise of 2.5 nm.

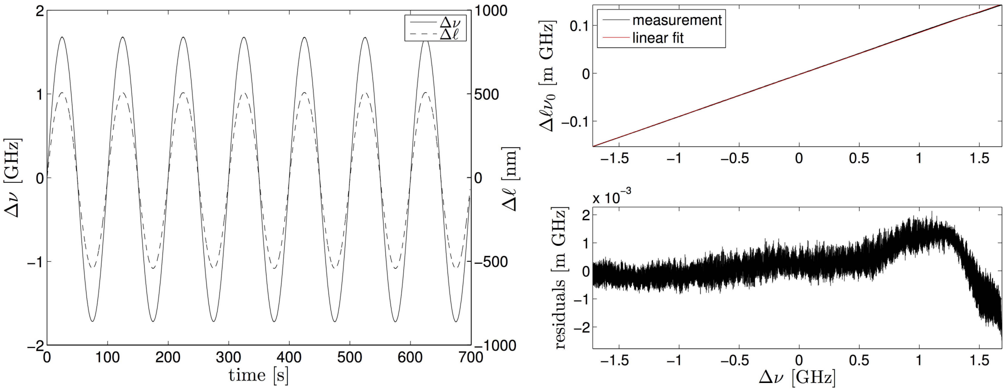

Figure 4.9.: Absolute length measurement. Left: signals in the time domain. Right top: $\Delta\ell\nu_0$ as a function of $\Delta\nu$. $\Delta\ell$ is the interferometer output signal while the frequency is measured with a wavelength-meter (High-Finesse WS6-600). The red trace is the linear fit where the slope is the length of the sample. Right bottom: fit residuals in units of m GHz, which are equivalent to $\sigma = 2.5\,\mathrm{nm}$.

$\Delta\ell$ and ΔT measurements The most critical parameter when designing the experiment is the period of the temperature signal. The period is chosen such that the phase shift between the temperature and the length measurements is minimized and does not change by increasing the period. Once this condition is met, the period is doubled to have enough margin. In this manner we ensure that temperature and length are measured in a steady-state condition. The period of the applied signal has to be defined for every material of interest because it depends on its thermal properties (heat capacity, emissivity, conductivity and density) and the geometry (area, thickness, etc.) of the sample. For our CFRP sample, a period of five hours was determined.

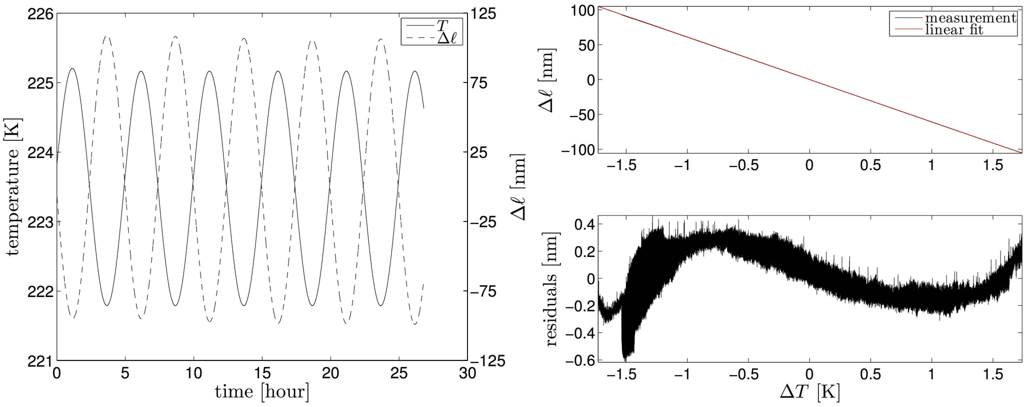

Figure 4.10.: Expansion measurement. Left: $\Delta\ell$ and ΔT in time domain. Right top: $\Delta\ell$ as a function of ΔT and the linear fit to the experimental data. The slope of the fit gives $\alpha\ell$. The absolute temperature here is 223 K. Right bottom: fit residuals ($\sigma \simeq 0.2$ nm).

Figure 4.10 (left) shows the recorded time series when applying a temperature excitation (solid line) consisting of a five-cycle sine wave with a period of 5 hours and $\Delta T_{\text{0-pk}} = 1.687$ K. This is large enough to minimize temperature read-out errors and induce a high signal-to-noise ratio in the interferometer. The noise of the temperature read-out is $\delta T = 1$ mK. The length changes of the sample are $\Delta\ell_{\text{0-pk}} = 102.23$ nm with noise levels of $\delta\Delta\ell \simeq 0.2$ nm (see Figure 4.10). The temperature was measured using three Pt-100 sensors. Two sensors were placed at the upper part of the tube, one in the inner surface and the other on the outer surface, and the third sensor on the exterior at the middle of the tube (see Figure 3.5 in Section 3.1.2). This configuration measures the largest temperature differences in the sample. The temperature gradient, ΔT_{grad}, increases at lower temperatures due to heat transfer from the support to the sample. At 223.48 K, ΔT_{grad} is 0.104 K. The third source of uncertainty in the temperature measurement is the absolute temperature value, which is given by the manufacturer (see Section 4.3.3) as 0.184 K for 223.48 K .

The right panel in Figure. 4.10 shows the linear fit to the data and the residuals. The slope of the fit is $\alpha\ell = (-60.7337 \pm 0.00025)\,\mathrm{nm\,K^{-1}}$, which considering $\ell = 0.0873946\,\mathrm{m}$ (see Section 4.3.5 Paragraph "Absolute length measurement"), leads to $\alpha = (-6.9494 \pm 0.00003) \cdot 10^{-7}\,\mathrm{K^{-1}}$. A detailed analysis of the total CTE uncertainty is given in Section 4.3.5 Paragraph "CTE determination and uncertainty analysis".

Tilt-to-length coupling As explained in Section 3.1.2, a dimensionally stable set-up is crucial to minimize errors in CTE metrology. One of the most dominant sources of error in our set-up is the TTL coupling, which occurs when the sample or the mirrors are tilted with respect to the optical beams, introducing an expansion which is not part of the CTE value. This happens due to asymmetric temperatures, different time delays, and mechanical tolerances, among other effects. The set-up is optimized for room temperature. In order to quantify this effect, the tilt of the M2 mirror was measured for each temperature. In the following, we focus on temperatures near 223.48 K. This measurement uses a slightly different optical set-up: instead of reflecting the beams off mirrors M1 and M2, they are both reflected off M2. The temperature modulation is very similar to the one shown in Figure 4.10, with an amplitude of 1.065 K, corresponding to a measured translation of 3.1705 nm (see Figure 4.11 (left)). This results in a TTL coefficient of $k = (2.8907 \pm 0.0001)\,\mathrm{nm\,K^{-1}}$ (slope of the linear fit in Figure 4.11 (right)) and indicates the effect of the M2 mirror tilt.

However, it does not provide information about the other mirror or the whole sample behavior. Different scenarios are possible: (a) the mirrors M1 and M2 have uncorrelated tilts, or (b) M1 and M2 tilts are the same since the whole sample is tilting. This effect dominates the uncertainty budget on the CTE estimation as shown in Section 4.3.5 Paragraph "CTE determination and uncertainty analysis", where we assume the tilt in M2 is representative of the tilt error (the M1 mirror tilt could not be measured due to its small size, half the diameter of M2). The validity of such assumption has been determined experimentally and is discussed in Section 4.1. The values for k vary from $7.29\,\mathrm{nm\,K^{-1}}$ at 120 K to $5.14\,\mathrm{nm\,K^{-1}}$ at 250 K in a parabolic way with a minimum at 200 K of $1.61\,\mathrm{nm\,K^{-1}}$.

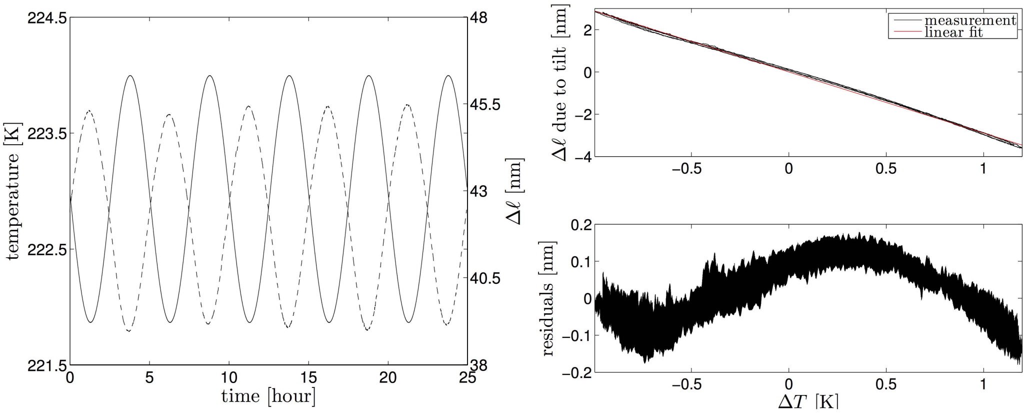

Figure 4.11.: TTL coupling measurement. Left: time domain series. Right: $\Delta\ell$ as function of ΔT and the linear fit and residuals. The coefficient (slope of the fit) is $k = (2.8907 \pm 0.0001)\,\mathrm{nm\,K^{-1}}$.

CTE determination and uncertainty analysis The CFRP CTE is calculated from the three measurements described in the previous sections: ℓ, $\alpha\ell$ and the TTL coupling coefficient, k:

$$\hat{\alpha} = \frac{\widehat{\alpha\ell}}{\hat{\ell}}, \tag{4.19}$$

which can be written as

$$\hat{\alpha} = \overline{\alpha} \pm \sigma_\alpha = \frac{\overline{\alpha\ell}}{\overline{\ell}} \pm \frac{1}{\overline{\ell}}[\sigma_{\alpha\ell}^2 + \overline{\alpha}^2\sigma_\ell^2 + k^2]^{1/2}. \tag{4.20}$$

The values at 223.48 K are $\overline{\ell} = 0.0873946\,\mathrm{m}$ and $\sigma_\ell = 4.2 \cdot 10^{-6}\,\mathrm{m}$ (see Section 4.3.5 Paragraph "Absolute length measurement"); $\overline{\alpha\ell} = -60.7337\,\mathrm{nm\,K^{-1}}$ and $\sigma_{\alpha\ell} = 0.00025\,\mathrm{nm\,K^{-1}}$ (see Section 4.3.5 Paragraph "$\Delta\ell$ and ΔT measurements"); and, $k = (2.8907 \pm 0.0001)\,\mathrm{nm\,K^{-1}}$ (see Section 4.3.5 Paragraph "Tilt-to-length coupling"). Consequently,

$$\begin{aligned}\overline{\alpha} &= \frac{-60.7337\cdot 10^{-9}}{0.0873946} = -6.95\cdot 10^{-7}\,\mathrm{K}^{-1} \qquad (4.21)\\ \sigma_\alpha &= \frac{1}{0.087}[(2.5\cdot 10^{-13})^2 + (2.9\cdot 10^{-12})^2 + (2.89\cdot 10^{-9})^2]^{1/2}\\ &\simeq \frac{2.89\cdot 10^{-9}}{0.087} = 3.32\cdot 10^{-8}\,\mathrm{K}^{-1}, \qquad (4.22)\end{aligned}$$

where clearly the TTL dominates the uncertainty budget. The two other terms, $\sigma_{\alpha\ell}$ and σ_ℓ, can be further reduced, to some extent, by increasing the measurement time since they are of statistical nature, even though they are currently not limiting factors. The TTL error could be further reduced if the mirror tilts were measured together with $\Delta\ell$ and their tilts were the same. This would indicate that the entire sample has tilted. In such a case, the TTL error in $\Delta\ell$ is $2\theta r$, with θ being the tilt and r the distance between the beams and the pivot point (see Section 4.1). Consequently, $\Delta\ell$ could be corrected by subtracting $2\theta r$ and the uncertainty would depend on the quality of the tilt measurement, the knowledge of r, and the uncorrelated mirror tilts. This could be done by using QPDs, a differential wavefront sensor (DWS) [45].

The absolute temperature error is briefly discussed in the following and included in the CTE uncertainty budget. The temperature error is

$$\epsilon_T = (\Delta T_{\mathrm{grad}}^2 + \epsilon_{T\,\mathrm{abs}}^2)^{1/2} = 0.211\,\mathrm{K}, \qquad (4.23)$$

where ΔT_{grad} is the temperature gradient of the sample and represents its non-homogeneous temperature distribution. $\epsilon_{T\,\mathrm{abs}}$ is the error in the temperature measurement after calibration (see Section 4.3.5 Paragraph "$\Delta\ell$ and ΔT measurements"). The temperature error impact for slowly changing CTEs is small. The effect can be quantified as $\frac{d\alpha}{dT}\epsilon_T$, which in our case is about $10^{-9}\,\mathrm{K}^{-1}$ in the worst case and well below the TTL error. Alternatively, the absolute temperature errors can be shown as horizontal error bars in the CTE-temperature plot. However, the estimated CTE is already a mean value in a temperature range of $\pm\Delta T = 1.6875\,\mathrm{K}$ around the absolute value. The error shown in Equation (4.23) thus applies to the mean temperature.

Table 4.3 shows the CTEs and their uncertainties for temperatures between 140 K and 250 K. The values are in the $10^{-7}\,\mathrm{K}^{-1}$ range and their uncertainties are in the order of $10^{-8}\,\mathrm{K}^{-1}$ with the TTL error as the most important contributor. The uncertainty increases at low temperatures due to stronger thermal effects. The CTE values are plotted in Figure 4.12.

Table 4.3.: CTEs and their uncertainties of the CFRP sample for temperatures between 140 K and 250 K.

T [K]	ϵ_T [K]	α [K^{-1}]	σ_α [K^{-1}]
140.75	0.93	$-3.76 \cdot 10^{-7}$	$0.8 \cdot 10^{-7}$
163.54	0.62	$-4.57 \cdot 10^{-7}$	$0.8 \cdot 10^{-7}$
188.05	0.44	$-5.81 \cdot 10^{-7}$	$0.6 \cdot 10^{-7}$
205.37	0.31	$-6.52 \cdot 10^{-7}$	$0.2 \cdot 10^{-7}$
223.48	0.21	$-6.95 \cdot 10^{-7}$	$0.3 \cdot 10^{-7}$
251.71	0.14	$-6.80 \cdot 10^{-7}$	$0.6 \cdot 10^{-7}$

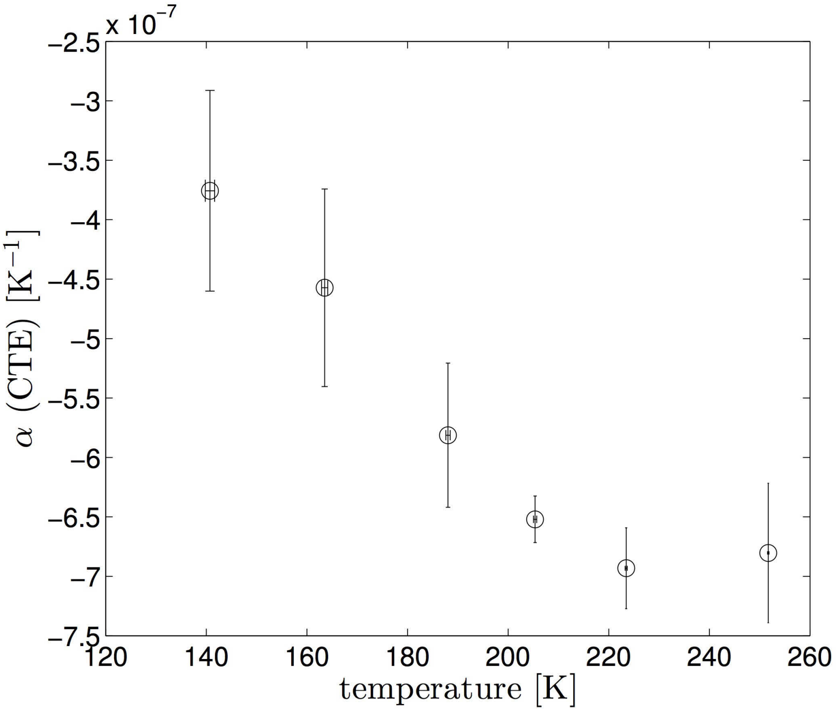

Figure 4.12.: Estimated CTE of the CFRP sample from 140 K to 250 K (see Table 4.3).

5. Application for space structures

More and more dimensional stable structures made of different materials to minimize the weight in a satellite are needed. The dimensional stability of each material is usually well known. The performance of the structure, with all the materials assembled using different joint technologies, have to be determined altogether.

In this chapter, investigations conducted on a structure made of Zerodur, CFRP and Titanium are presented. This 0.5 m long structure is a technology demonstration breadboard for the triple mirror assembly (TMA) in the laser ranging instrument (LRI) for the GRACE (Gravity Recovery and Climate Experiment) Follow-On (GRACE FO) mission [5].

The verified CTE metrology system described in Chapter 3 was adapted to determine the dimensional stability of the TMA structure. This representative structure was conducted in collaboration with the University of Bremen, German Aerospace Center (DLR) in Bremen and Airbus DS GmbH in Friedrichshafen in the Laboratory for Enabling Technologies (LET). The main set-up is the same as described in Section 3.2.1, set-up (**A**), with a different thermal system. Parts of this chapter are published in Reference [60].

5.1. Dimensionally stable spacer breadboard

The structure investigated in this chapter is a dimensionally stable spacer TMA breadboard for the GRACE FO mission [5, 61]. Airbus DS GmbH was not selected to built the flight model of the TMA, however, it shows the technology and the know-how to build such a complex opto-mechanical structure.

The GRACE FO mission will be launched in early 2018 and, as GRACE, continue mapping the gravitational field of the earth. Two satellites on the same orbit, one following the other, measuring the changes in their distance of $\approx 220\,\mathrm{km}$. This distance changes are measured by a microwave ranging with a noise level of $\mu\mathrm{m}/\sqrt{\mathrm{Hz}}$ around $10\,\mathrm{mHz}$. GRACE FO will include a second instrument, the LRI, as a technology demonstrator that should have 20 times better performance.

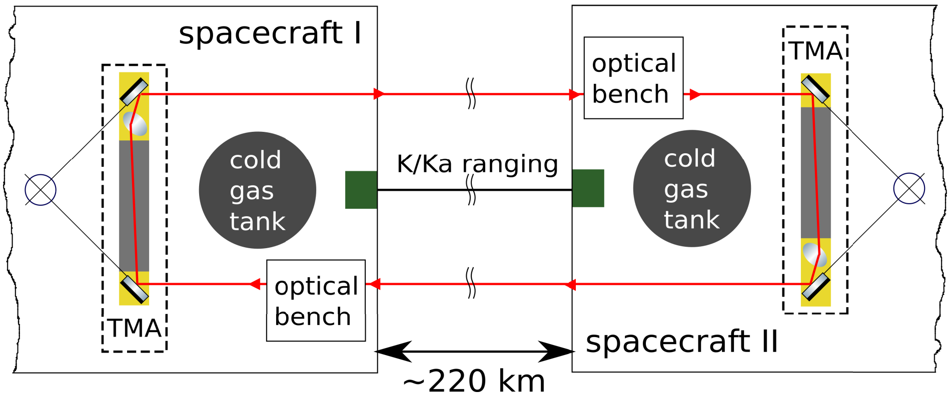

Figure 5.1.: Schematic of the LRI. The optical layout in and between the two almost identical spacecraft is shown. The microwave ranging system (K/Ka ranging) can be seen in the middle and the optical links guided around the cold gas tank using two distributed corner cube retro-reflector (TMA).

The LRI is a joint US and German project between NASA, JPL in USA, and GFZ, AEI, DLR, SpaceTech GmbH, and Airbus DS GmbH in Germany. This new instrument is an add-on to the satellites using the available space without changing the main configuration of the original GRACE satellites. In Figure 5.1 a schematic of the LRI and the two almost identical spacecraft is shown. The microwave ranging system (K/Ka ranging) is located at the middle as a link between the spacecraft. The optical links from the optical benches have to be routed around the microwave ranging system and the cold gas tank by the use of a distributed corner cube retro-reflector, the so called TMA. The TMA has a length of about 0.6 m and consists of a CFRP structural frame and Zerodur mirror assemblies on each side. The mirror assembly is made of three orthogonal mirrors forming a corner cube reflector, two mirrors on one side and the third on the other. The CFRP frame serves as a high-stability mount.

The length stability requirements of $< 25\,\mathrm{nm}/\sqrt{\mathrm{Hz}}$ in translation (expansion along the $\approx 0.5\,\mathrm{m}$ long structure) and $< 1\,\mu\mathrm{rad/K}$ in tilt in two dimensions must be guaranteed. This stability requirements of the TMA are mentioned in Reference [6]. The worst case thermal environment of $0.3\,\mathrm{K}/\sqrt{\mathrm{Hz}}$ is assumed on the basis of GRACE measurement data without any thermal isolation [62]. In GRACE FO the thermal control system should be improved and with additional thermal shielding of the LRI/TMA a much better (up to 10 times better) thermal environment can be expected. The worst case requirement for the pathlength coefficient is

$$\frac{\Delta\ell}{\Delta T} = \frac{25\,\mathrm{nm}/\sqrt{\mathrm{Hz}}}{0.3\,\mathrm{K}/\sqrt{\mathrm{Hz}}} = 83.3\,\mathrm{nm/K}. \tag{5.1}$$

The TMA spacer breadboard design from Airbus DS GmbH, is a hexagonal CFRP tube with a length of 499 mm, a width of 64 mm, and a wall thickness of 2 mm resulting in a total mass of 300 g. A CAD model can be seen in Figure 5.2 and a photograph in Figure 5.3. As it can be seen in these pictures, the tube shows several elongated slots which serve as springs to compensate forces due to different CTEs of the the spacer and the mounting bracket that holds the tube in position inside the satellite.

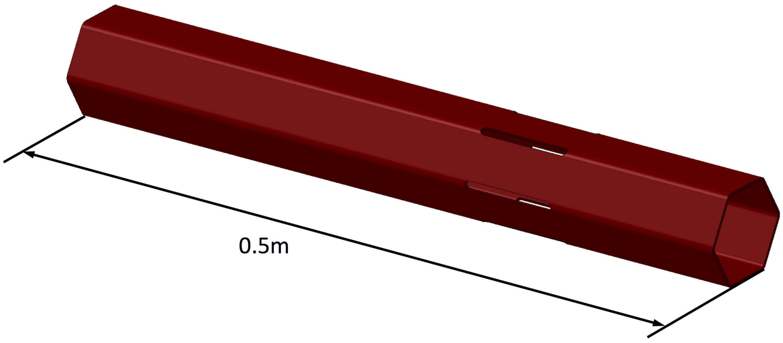

Figure 5.2.: CAD model of the 0.5 m long TMA spacer.

Figure 5.3.: Photograph of the TMA spacer and a one Euro coin for size comparison.

The TMA CFRP frame was manufactured by wrapping the single Carbon fiber layers around a metal core in order to realize the hexagonal shape. In terms of thermal stability it was not designed to have a zero expansion along its longitudinal axis. It is more important that the angle between the individual mirrors stays as constant as possible to ensure parallel laser beams. If the TMA frame changes its length due to thermal expansion the separation between the incoming and outgoing laser beams changes, but their axis remain parallel. The CFRP used for the TMA consists of a M60J high modulus Carbon fiber with a CTE of $-1.1 \cdot 10^{-6}\,\mathrm{K}^{-1}$ along the fiber axis and is cured with a L 20 SL series epoxy resin. The epoxy resin is specified with a moisture pickup of 0.03 % (24 h at 22 °C and standard pressure and humidity). [63, 64]

5.1.1. Preparations for the TMA measurements

In order to characterize interferometrically the TMA frame with representative Zerodur endfittings and their joint technology, two parallel mirrors were mounted on the TMA. The mirror mounts were made of Zerodur and were bonded into the TMA frame the same way it would be in a flight unit, however, without the retroreflector mirrors. The bonding was performed by Airbus DS GmbH.

The same bonding procedure was applied to the Titanium ring bracket holding the CFRP frame. The Titanium bracket was clamped to the sample support. Here, the requirements on thermal and mechanical stability are less critical because any instability of the mount influences both mirrors the same way (common mode). A picture of the CAD model is presented in Figure 5.4.

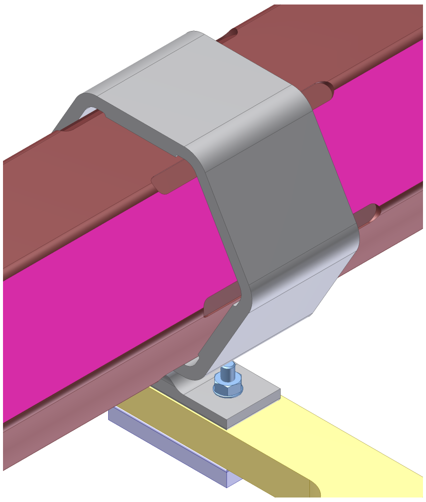

Figure 5.4.: Titanium mounting ring bonded to the TMA.

The Zerodur endfitting bonded on the end of the TMA CFRP frame, is shown in Figure 5.5. The endfittings are inserted in each end and bonded on six sides (bonding surfaces). This results in radially acting adhesive layers which minimize the motion of the mirror mounts under thermal fluctuations. Each endfitting provides four attachment pads, three are used to clamp the mirror that reflects the measurement beam. These three pads define the position of the contact surface of the mirror and therefore they need to be flat with machining tolerances of 20 µm. In addition, the two planes defined by the pads on each side of the TMA have to show a close tolerance in parallelism of the clamped mirrors. This is crucial for a proper reflection of the laser beams to achieve good interference signals.

The maximum stationary tilt allowed between the two mirrors at the TMA is determined by the adjustment range of the kinematic mirror mount, which is used for realizing a proper reflection of the laser beams (see Section 5.2.4). In this case, a maximum misalignment of 2 mrad can be tolerated which leads to a tolerance in parallelism of 0.066 mm, considering a distance of approximately 33 mm between the attachment pads.

In order to reach this requirement the endfittings are attached to the TMA frame following a defined adhesive process. The error in the inner geometry of the TMA requires high tolerances of the bonding pouches. Therefore, the

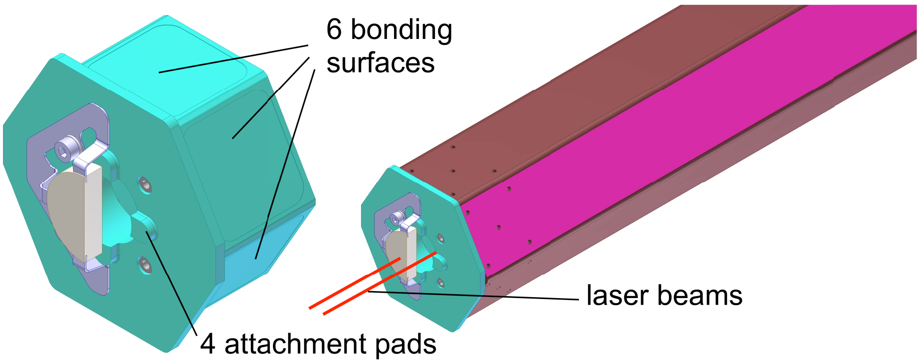

Figure 5.5.: The Zerodur endfittings are bonded to the TMA and the mirrors are clamped on the Zerodur endfittings to reflect the laser beam to investigate its dimensional stability. One endfitting is bonded to the CFRP frame on each side.

final position of the endfittings will differ from the initial state. For this reason, it was decided to machine the attachment pads in a precise (realtime interferometric measurement) lapping process after the bonding. This way, the required parallelism of the attachment pads can be realized.

D-shaped mirrors are clamped at the Zerodur endfittings to enable a three point mounting with a bracket (see Figure 5.5). The only difference between the first and second mirror is that the first mirror is mounted at its backside and the second mirror on its frontside. This includes the thermal expansion of the first 6 mm thick mirror in the measurement, which is the reason for choosing Zerodur (CTE of $\approx 10^{-8}\,\mathrm{K}^{-1}$) mirrors to minimize the impact to the dimensional stability of the whole structure.

5.2. CTE metrology set-up

The set-up to measure the CTE of the CFRP spacer (TMA) is described here. Most of the subsystems of set-up (**A**) described in Section 3.2 are used. The main differences are the new thermal chamber, the sample support and the additional kinematic mirror mount in the optical set-up (see Figure 5.6).

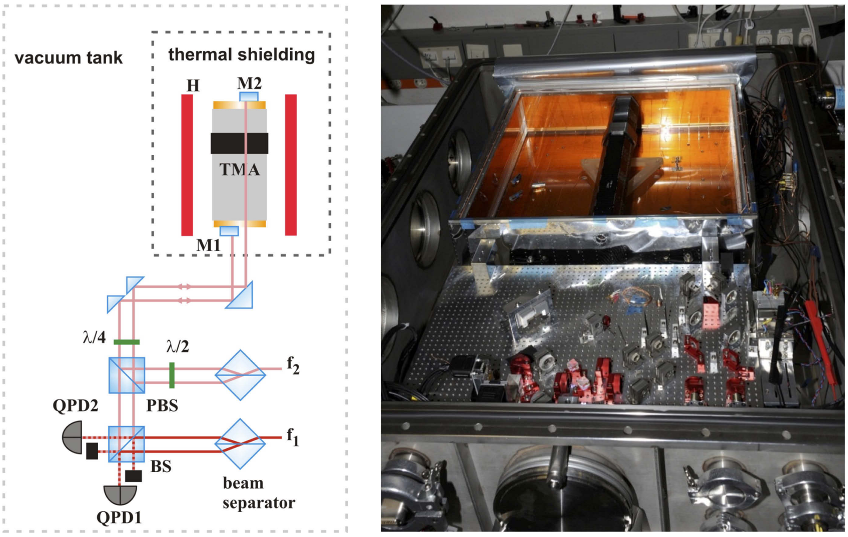

(a) (b)

Figure 5.6.: (a) schematics of the CTE measurement of a CFRP spacer; (b) photograph of the vacuum chamber, interferometer (front) and thermal chamber with sample structure, TMA (back).

5.2.1. Requirements for the metrology set-up

The characterization of the samples requires, besides the adapted optical set-up, additional new subsystems, such as a new thermal chamber for a controlled temperature cycling and a thermal stable support of the structure. The schematic of the interferometer, including a kinematic mirror mount is shown in Figure 5.6 (a). The thermal chamber is located next to the interferometer in the vacuum chamber where the samples are placed inside and are completely enclosed by metal plates (see Figure 5.6 (b)). Mounts have been designed which are placed on a CFRP breadboard to connect the sample and the interferometer. Basic requirements on the thermal and mechanical systems were defined, based on the experience accrued from the set-up with tube shaped samples:

- Impact of thermal fluctuations on the interferometer must be as low as possible in order to maintain measurement performance (ideal situation $T =$ constant).

- Stable mechanical connection between interferometer and sample to maintain the relative position.
- Sufficient coverage of sample by the thermal chamber and a flexible and easy integration of different samples.
- Controlled temperature cycling of the sample (e. g. periodic function) with the thermal chamber to allow a warm up rate of the samples of $\Delta T \approx 3\,\mathrm{K}$ within a period of ≈ 1 hour at approximately 30°C.

These requirements are considered in the design phase and the realized system design is described in the following sections.

5.2.2. Thermal chamber

The new thermal chamber was designed to heat and cool structures radiatively with a maximum size of $503\,\mathrm{mm}\times 503\,\mathrm{mm}\times 95\,\mathrm{mm}$ from 20°C to 40°C (see Figure 5.7). The size of the thermal chamber was chosen to fit into the vacuum chamber and to have as much space in the thermal chamber as possible for big structures. A set of 18 Peltier elements, also known as thermoelectric coolers (TEC), are placed between two metal sheets and used to produce a given temperature variation. Every TEC element was pressed between both sheets, using heat transfer paste and four M3 screws to improve thermal contact. Underneath the screws head, thermal washers minimize the heat transfer between the two sheets on both sides of the TECs. These washers are made of Polyvinylidenfluorid (PVDF) which is a vacuum compatible polymer with low thermal conductivity of $0.17\,\mathrm{W/(m\cdot K)}$. At the inner side of the chamber, a 2 mm thick Copper sheet with high thermal conductivity of $394\,\mathrm{W/(m\cdot K)}$ is mounted [65]. To improve the emissivity of the Copper, Kapton was used to laminate the Copper surface, which has a specified emissivity in the range of 0.8. An emissivity of 0.83 was measured with a TIR 100-2 by INGLAS GmbH & Co. KG. In comparison, for the untaped Copper sheet an emissivity of 0.08 was measured.

The outer sheet is used to buffer the heat dissipation of the TEC elements. Therefore a 8 mm thick Aluminum sheet is used. Additionally the Aluminum

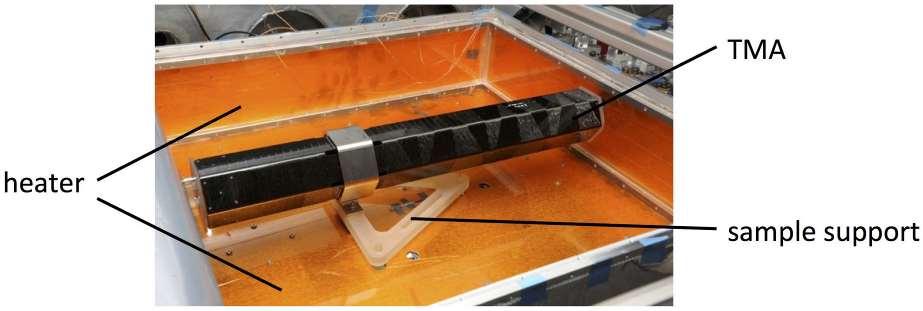

Figure 5.7.: Assembled TMA mounted in the thermal chamber. The thermal chamber is suitable for samples with a maximum size of 503 mm×503 mm×95 mm. The Kapton taped Copper sheets (heater) radiate the heat to change the temperature of the TMA.

is connected with Copper rods to the vacuum chamber to transfer the dissipated heat to the chamber. The two sheets are separated with the TEC elements and at the area where no TEC elements are placed, MLI foil minimizes the radiative heat transfer. The whole thermal chamber is also wrapped by MLI to shield the interferometer from radiative heat transfers.

5.2.3. Sample support

The sample support is required for a stable mounting of the TMA to minimize the movement of the structure relatively to the laser beam due to the applied temperature variations. During the design process, the following aspects were considered:

- mechanical and thermal stability,
- TMA compatibility and, if possible, potential future projects,
- vacuum compatibility,
- angular adjustability for alignment between the laser beams and the mirrors, and
- defined contact points for a mechanical stable mount of the sample.

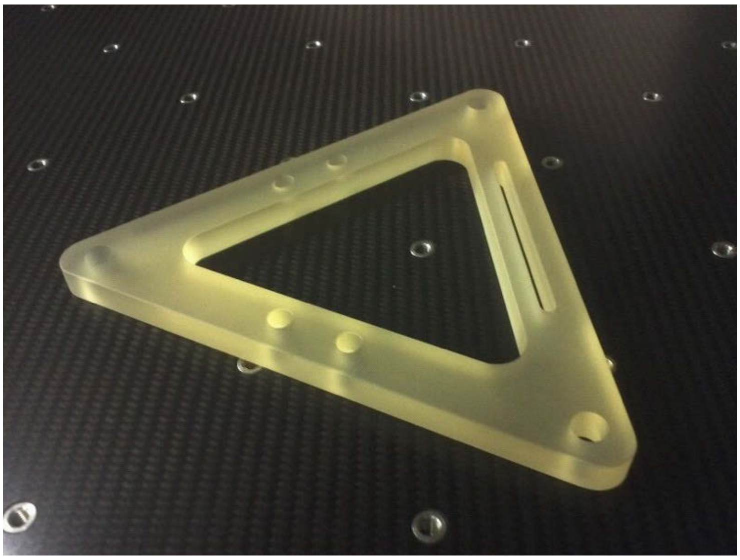

Figure 5.8.: Photograph of the Zerodur triangle mount without the feet.

To provide the necessary thermal stability the choice of materials was limited to low expansion glass ceramics, Invar or CFRP. Due to a complex design process and costly manufacturing, CFRP was not further considered as an option. The baseline approach was to realize the sample support using Clearceram. It is highly dimensionally stable, and it is possible to manufacture complex geometries by milling process.

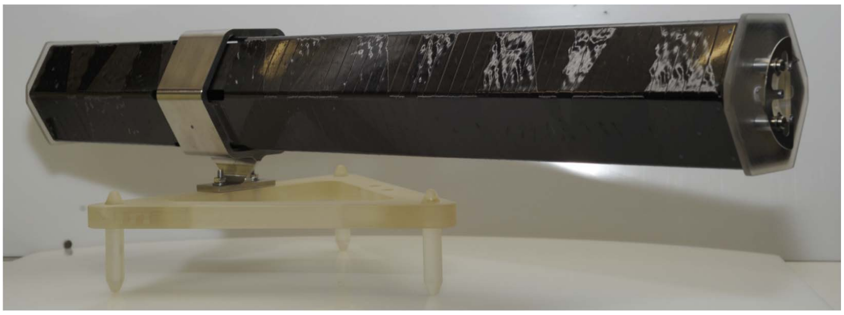

Figure 5.9.: Photograph of the assembled TMA on the triangle mount.

The sample support consists of an equilateral triangle (see Figure 5.8) and three feet for a statically indeterminate mounting. The feet also serve as pick-up pads for potential future larger structures. The TMA frame was mounted with a Titanium ring bracket at one side of the triangle mount (see Figure 5.9). The three feet, which are manufactured by a grinding process, are bonded into the clearance holes in the milled triangular structure. Therefore, the adhesive surface has a radial direction of action which reduces the thermal influence on the mounting structure. The feet have a diameter of 10 mm and have rounded tips on the ends. A 5 mm thick quadratic shim is placed under each feet to ensure a defined contact point to the CFRP breadboard, thus reducing the risk of placing the feet directly on an thread insert. The shims are simply put below the thermal chamber on the CFRP breadboard. The sample support is put top down through three holes in the bottom sheets of the thermal chamber (see Figure 5.7).

5.2.4. Kinematic mirror mount

The parallelism of the TMA mirrors (M1 and M2, see Figure 5.6 left) is not accurate enough, thus it is necessary to align each laser beam individually. Therefore one double mirror mount with two different mirror mounts for each beam (independently adjustable) was designed and built (see Figure 5.10). It was essential that the mount could be realized with a very small gap between the mirrors (< 1 mm) to enable a reflection of both beams and avoid clipping. The beams have a diameter of 1.44 mm and are separated by 5 mm. The connection between the two mirror mounts and the adjustment mechanism had to be mechanically and thermally stable to minimize any angular misalignment of the laser beams. Generally, in interferometric distance measurements the standard mirror mounts used for beam guidance do not have to be extremely stable, because the two beams are reflected off the same mirror. In case of a dimensional change of the mirror, both beams are affected the same way (common mode behavior), which does not lead to a difference in the optical paths.

However, in this case, each laser beam is affected differently, which makes the assembly critical. For the mirror mounting, two highly stable Radiant Dyes MNI mirror mounts with a translation of 125 µm per turn were chosen. In terms of thermal stability the front plates holding the mirrors, were designed

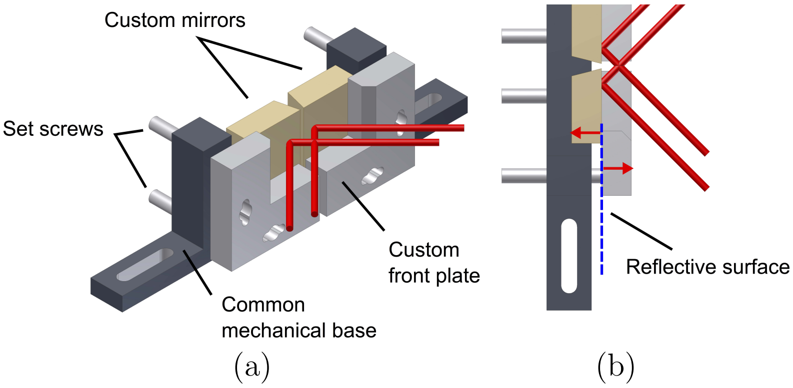

Figure 5.10.: CAD drawing and principle of the double mirror mount. The reflecting surface of the mirrors are at the back of the of the front plate of the mirror mount, thus the thermal expansion of the front plates has no influence to the stability.

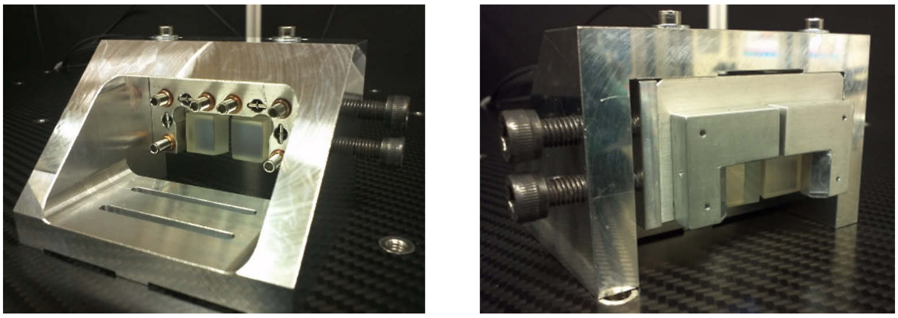

Figure 5.11.: New double mirror mount. Photograph left: from behind; right: front view.

in a way that they would allow mounting on the reflective surface. This way the expansion of the mirror and the front plate do not affect the position of the reflective surface. The mirrors were bonded to the front plates using the high viscosity Hysol EA 9361 to absorb tensions caused by the bonding of two different materials, Aluminum and Zerodur. A CAD model of the double mirror mount with the laser beams is presented in Figure 5.10 showing: (a) isometric view, (b) top view with the red arrows marking the thermal expansion and the reflecting surface of the mirrors (blue dashed line).

Due to a manufacturing error, the front plate was positioned too far up, so that the laser beams hit the front plates instead of the mirrors. To solve this issue the assembly was turned over and fit into a new mount. A photograph of

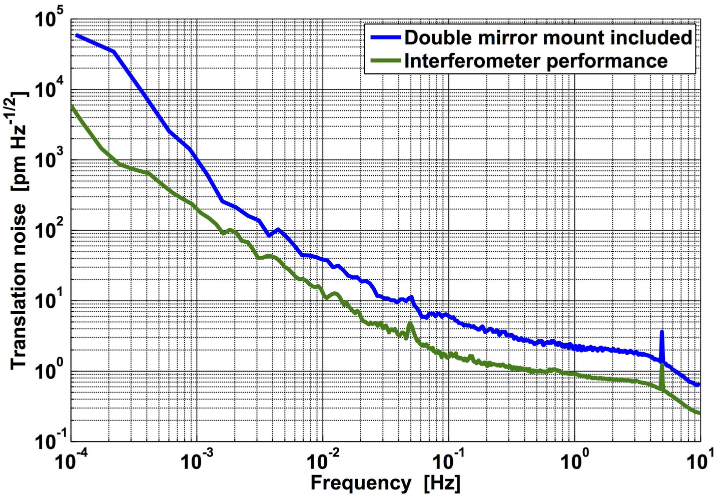

Figure 5.12.: Interferometer noise with and without the new mirror mount.

the new double mirror mount can be seen in Figure 5.11 showing the view from behind on the left side, and front view on the right side. The attachment was conducted by screwing two M6 screws from the sides which provide sufficient mechanical stability.

With the double mirror mount, a new component was introduced into the measurement set-up. Hence, it had to be investigated how the measurement performance would be affected. Two scenarios were compared: a LSD was calculated with a) one mirror as measurement and reference mirror, b) the double mirror mount was inserted and each of the adjustable mirrors served as measurement and reference mirror, respectively. Through this method, the relative movement between the two mirrors can be investigated. The two LSD curves are plotted in Figure 5.12 translation noise on the x-axis, and frequency on the y-axis. The green line indicates the interferometer performance with the single mirror set-up and the blue line indicates the characterization of the double mirror mount. It can be seen that the noise increased approximately by the factor 2 to 5 depending on the frequency, however, it is still good enough for CTE measurements. This can be seen in the uncertainty budget of the expansion measurement of 0.1 nm, which is presented in the following section.

5.3. Tilt and CTE metrology of the TMA breadboard

In this section the length changes $\Delta\ell$ and tilt changes of M1 and M2 as a function of temperature around 29°C are presented. The measurements were done within the expected temperature in orbit of 10°C to 30°C [6]. Firstly, the tilt of the two mirrors mounted on both ends of the TMA were determined to measure the TTL coupling error (ϵ_{TTL}). Secondly, the expansion as a result of the applied temperature variation was determined and compared to the requirements. The requirements of the TMA breadboard are formulated in a pathlength coefficient $\Delta\ell/\Delta T$ and the tilt coefficients as the difference between M1 and M2 in horizontal and vertical direction, $\gamma_{\mathrm{lr}} = (tilt_{\mathrm{M1,lr}} - tilt_{\mathrm{M2,lr}})/\Delta T$, and $\gamma_{\mathrm{ud}} = (tilt_{\mathrm{M1,ud}} - tilt_{\mathrm{M2,ud}})/\Delta T$ showing the bending of the structure as a function of temperature. A schematic of the TMA mirror tilts are shown in Figure 5.13.

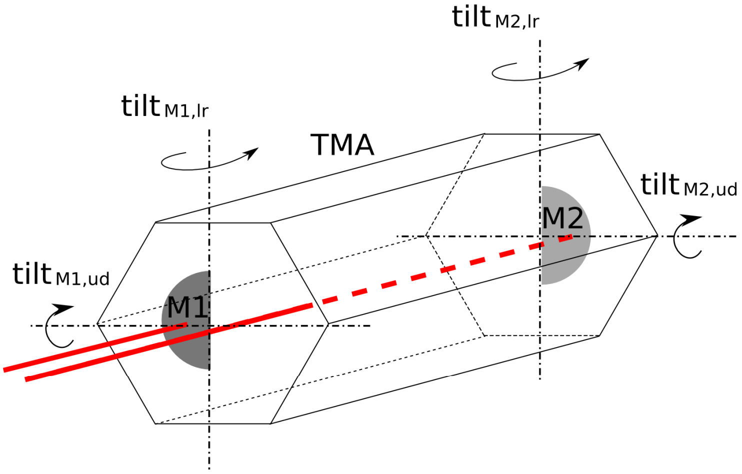

Figure 5.13.: Schematic of the TMA and the tilts according to the measurements.

5.3.1. Tilt and TTL coupling

The tilts of the TMA mirrors are measured using a DWS method described in Section 1.3.2. The most important tilt is $tilt_{lr}$ (tilt from left to right), which is the plane where the tilt couples into the expansion signal. Figure 5.14 shows the $tilt_{lr}$ of the mirrors M1, M2 and the difference between the two mirrors (M1-M2). This measurement was done simultaneously to the expansion measurement with a sinusoidal temperature variation. A sinusoidal tilt signal was expected, but the additional higher frequencies in the measurement indicate that we hit the limitations of the interferometer. Therefore a correction of the expansion signal is not possible and an additional error contribution need to be considered. The worst case error assumption for the TTL coupling, ϵ_{TTL}, is that the whole structure tilts by an amplitude (peak to peak value of M1 tilt left-right) of 4.5 µrad (see Figure 5.14) and with a beam distance of 5 mm the TTL coupling can be calculated as:

$$\epsilon_{\mathrm{TTL}} = \tan(4.5\,\mu\mathrm{rad}) \cdot 5\,\mathrm{mm} = 22.5\,\mathrm{nm}. \tag{5.2}$$

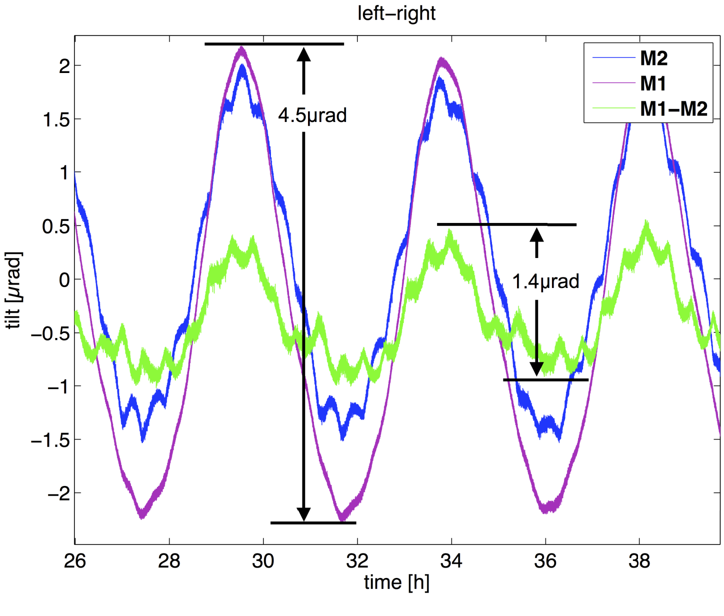

Figure 5.14.: Left to right tilt of the TMA mirrors. The measurement has been performed simultaneous to the expansion measurement.

The left-right bending of the whole structure is described in the difference of the mirror tilts, M1-M2 (left-right), where the peak-to-peak value of 1.4 µm (see Figure 5.14) was assumed as a worst case estimation. With temperature variation of 3.52 K the tilt coefficient for left-right can be calculated, resulting $\gamma_{\mathrm{lr}} = \Delta tilt_{\text{left-right}}/\Delta T \approx 0.4\,\mu\mathrm{rad/K}$.

In Figure 5.15 up-down tilt of the mirrors M1, M2 and their difference, M1-M2, are shown. The difference of M1-M2 shows the up-down bending of the structure. A tilt coefficient for up-down can be calculated, $\gamma_{\mathrm{ud}} = \Delta tilt_{\text{up-down}}/\Delta T \approx 0.6\,\mu\mathrm{rad/K}$, assuming a peak-to-peak value of 2 µrad (see Figure 5.15) of $\Delta tilt_{\text{up-down}}$ in a worst case estimation with a temperature variation of 3.52 K.

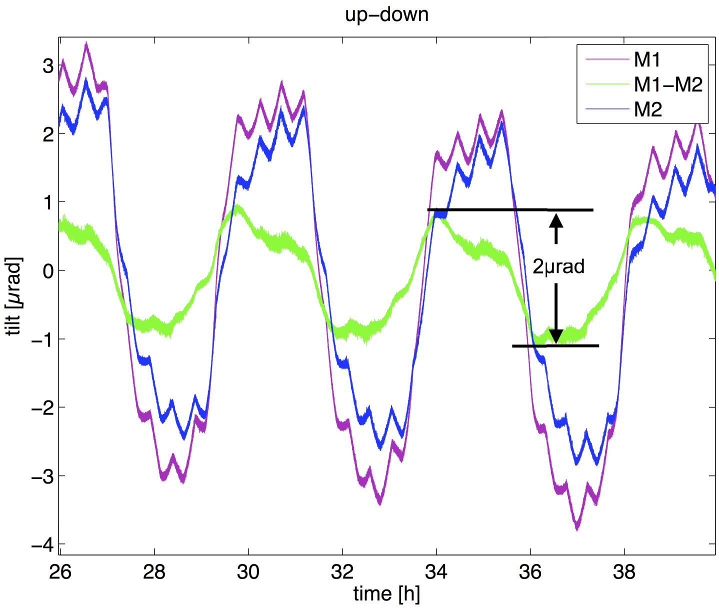

Figure 5.15.: Up to down tilt of the TMA mirrors. The measurement has been performed simultaneous to the expansion measurement.

5.3.2. CTE measurement and pathlength coefficient determination

Several CTE measurements are done with different temperature profiles: waveform, period and amplitude. Figure 5.16 shows a sinusoidal waveform temperature signal applied to the sample showed the lowest error of the expansion measurement. The sinusoidal temperature variation with a period of 4.2 h and amplitude (peak to peak) of $\Delta T = (3.52 \pm 0.01)\,\mathrm{K}$ centered around 29°C as well as the resulting expansion of the long TMA in a 70 hour measurement. The expansion of the TMA is $\Delta\ell = (242.0 \pm 0.1)\,\mathrm{nm}$ and the TTL coupling error contribution of $\epsilon_{\mathrm{TTL}} = 22.5\,\mathrm{nm}$, yielding a TMA pathlength coefficient $\Delta\ell/\Delta T = (-68.75 \pm 6.389)\,\mathrm{nm/K}$. The length of the TMA, from the reflective mirror surface of M1 to the reflective surface of M2, is $\ell = (518.0 \pm 0.1)\,\mathrm{mm}$. The linear CTE including the propagation of uncertainty is calculated by:

$$\alpha_{TMA} = \frac{\Delta\ell}{\ell} \cdot \frac{1}{\Delta T} = (-1.327 \pm 0.123) \cdot 10^{-7}\,\frac{1}{\mathrm{K}}, \tag{5.3}$$

where the error budget is mainly driven by the TTL coupling, which accounts for 90% of it.

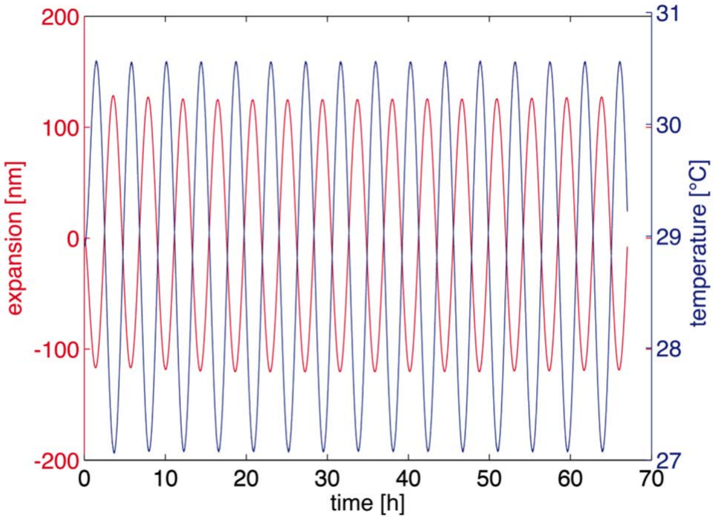

Figure 5.16.: Measurement of the expansion (red curve) of the TMA with sinusoidal temperature variation (blue curve).

5.3.3. Final results of TMA investigations

To finalize this chapter, the results of the measurement at 29°C are shown in Table 5.1. The measured values are compared with the requirements of the TMA structure.

For the CTE value, a normalized value for comparison with other structures or materials is provided. The three requirements ($\Delta\ell/\Delta T$, γ_{lr}, and γ_{ud})

Table 5.1.: Requirements and results of the TMA investigation.

	CTE $[10^{-7}\,1/\mathrm{K}]$	$\Delta\ell/\Delta T$ [nm/K]	γ_{lr} [µrad/K]	γ_{ud} [µrad/K]
requirements	–	83.33	1	1
measurements	-1.327 ± 0.123	-68.75 ± 6.389	≈ 0.4	≈ 0.6

formulated as requirements (see Section 5.1) are met by the here presented TMA prototype at the temperature of 29°C.

6. Summary

Throughout the research work described in this thesis, measurements of the thermal properties, in particular the CTE of materials were conducted. To this end, a first CTE metrology system (set-up (**A**)) was realized to determine tube shaped material samples and initial measurements were taken at Airbus DS GmbH at room temperature, and slightly higher temperatures. The system was verified measuring ultra stable materials. Measurements of glass ceramics from two different manufacturer are shown and compared to the corresponding vendor values.

At the German Aerospace Center (DLR) in Bremen, a completely new CTE metrology system (set-up (**B**)) was designed, realized and verified with a detailed error budget to investigate samples in a wider temperature range. A CFRP sample has been used to demonstrate the performance of our dilatometer over a wide temperature range (140 K to 250 K). Measured CTE levels of 10^{-8} K^{-1} have been shown, where our measurement capabilities were limited by tilt-to-length coupling due to sample tilt. The CTEs and a detailed uncertainty analysis was developed, indicating the sources of uncertainty.

As an application, the verified metrology system was adapted to measure a representative space structure. A 0.5 m long triple mirror assembly breadboard, a distributed corner cube retro-reflector with representative joint technologies for the GRACE FO space mission was investigated. The structure was built from a CFRP tube, Titanium bracket and Zerodur endfittings and tested in our CTE metrology system at Airbus DS GmbH in Friedrichshafen.

7. Outlook

A main result of this thesis is the identification of the TTL coupling as the major error contributor for CTE measurements. This needs to be minimized in order to improve the measurement accuracy. A possibility for this is to modify the sample support to reduce the tilt of the sample. A first CAD drawing of a new sample support is suggested in Figure 7.1. The newly designed Zerodur sample support should have a better dimensional stability than the Invar ring used for measurements shown in this thesis. The uncertainty can also be reduced by actually measuring the tilt, for example, by using differential wavefront sensing (DWS), and translation simultaneously and correcting for it in post-processing. The former solution is not convenient when a wide temperature range is needed. For this reason, the second approach is considered to be more promising. The set-up is now being upgraded to incorporate these improvements and reduce the uncertainty to the 10^{-9} K^{-1} range.

Measurements with a sample made of a high-purity dislocation-free float-zone (FZ) Silicon crystal cut in <100> orientation from the 0 zone where the CTE is well known should help identify more systematic errors and validate the measurement accuracy.

Comparing CTE measurements with other institutes (e.g. National Metrology Labs) is also a big goal for the project. Such a comparison is crucial to calibrate the CTE metrology set-up by measuring a well calibrated sample. First actions are done to find a sample geometry which is compatible with our set-up and a set-up of other laboratories.

Investigations of the dimensional stability of complex structures for future space application, as demonstrated for the GRACE FO TMA, is a future goal. The metrology system shown here can be adapted to other structures.

A suggestion for an alternative optical set-up is based on resonant optical cavities that can be compared with the results of the two-beam interferometry demonstrated in this thesis. The main interest in the new optical design is that the offset of the two beams does not exist anymore and the TTL coupling behavior could be much smaller. Also, by using optical cavities and locking two lasers to adjacent cavity modes the absolute length of the sample can be measured by tracking the change in frequency between the two lasers while the temperature of the sample is changed.

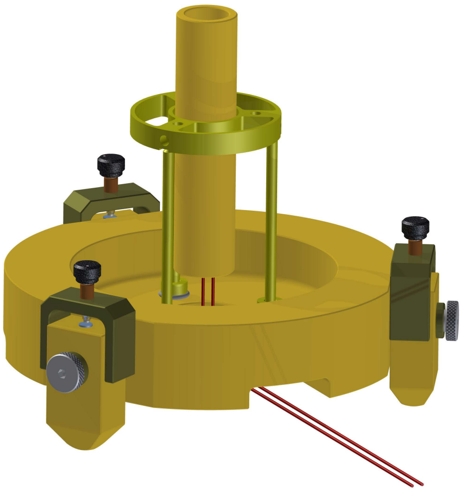

Figure 7.1.: CAD drawing of a new design of a more dimensionally stable Zerodur ring sample holder to minimize the tilt of the sample.

A. Alternative LISA telescope design investigation

The investigation of the telescope structure described in this chapter was carried out at the University of Florida in the group of Professor Guido Mueller. This structure is an alternative design of the LISA telescope. The main goal of this experiment was to demonstrate the dimensional stability of a mock-up telescope structure in the LISA measurement bandwidth and at the expected operating temperatures. The main results are published in Reference [2].

A.1. LISA telescope

In the LISA mission [1, 66] a critical element is the telescope, which receives and transmits the light over a few million kilometers to a far spacecraft. The aperture of the LISA telescope is approximately 0.4 m in diameter and the primary and secondary mirror are about 0.6 m apart. The expected operating temperature is −65°C. The telescope dimensions have changed slightly for the latest proposed LISA space mission. The dimensions and requirements mentioned here, are related to the former LISA concept, where the spacecraft were 5 million km apart.

The dimensional stability requirements for the telescope are very challenging, since distance changes between the two mirrors are in the direct path of the interferometer science measurements, which has to perform at the $10\,\mathrm{pm}/\sqrt{\mathrm{Hz}}$ level. Consequently, the contribution of telescope spacer length has to be significantly less than that. The requirement has been set to $1\,\mathrm{pm}/\sqrt{\mathrm{Hz}}$ in the LISA measurement bandwidth. In addition, the absolute distance cannot change more than $2.5\,\mu\mathrm{m}$, otherwise the laser beam defocusses and decreases the measurement signal quality [67, 68].

One promising telescope candidate for LISA is an off-axis (Schiefspiegler) telescope which was built for investigations by Airbus DS GmbH. The mirrors are made of Zerodur and the spacer and support are made of CFRP and metal, such that the positive CTE of the metal components is compensated by the CFRP struts, designed and manufactured to have the property of a negative CTE. Another possible design is a cylinder shaped CFRP spacer which covers both, primary and secondary mirror. The biggest challenge for those designs is the chosen material: CFRP, which can defocus the telescope due to the moisture release in vacuum. This causes dimensional changes in the telescope. [69]

An alternative design, which was investigated as a part of this thesis, is a quadpod on-axis telescope (Cassegrain telescope) made of SiC (see Figure A.1). The interesting material properties of SiC are: (i) low CTE, (ii) relatively high thermal conductivity, and (iii) the relatively low outgassing compared to the CFRP structures. The optical benefit of an on-axis design is the smaller sensitivity to defocusing. However, stray light can be a problem [70].

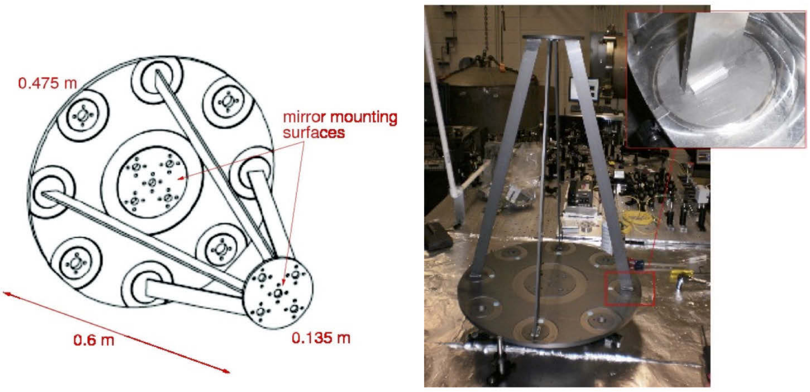

Figure A.1.: Left: CAD model of the telescope spacer. Right: photograph of the spacer mounted to primary and secondary plates with sister blocks to increase the mechanical stability. [2]

A.2. Experimental set-up

For the approach to measure the dimensional stability of the mock-up telescope structure a particular experimental set-up was realized. In Figure A.2 the schematic of the SiC telescope measurement set-up is shown. The telescope is mounted inside a vacuum tank and cooled with liquid Nitrogen (LN_2) to the expected operation temperature where the dimensional stability was determined, using an optical cavity set-up.

The SiC telescope structure was made such that mirrors for the stability measurement could be mounted to the primary and secondary plate (see Figure A.1). High reflective mirrors were installed to enable a Fabry-Pérot cavity set-up. The optical cavity control set-up was based on the Pound-Drever-Hall (PDH) technique [57, 68]. This technique is crucial to lock a laser from outside the vacuum chamber to the telescope cavity. A beat-note frequency of the laser locked to the telescope cavity and another laser locked to a reference Zerodur cavity was measured to calculate the dimensional stability. The beat-note frequency was measured by using a frequency counter, HP53132A, with a sampling frequency of approximately 1 Hz.

To minimize the coupling of the ground vibrations into the telescope structure, a two stage isolation system was built. Without the isolation system the stability measurements of the telescope were limited by ground vibrations. The main vibration frequencies were higher than the measurement bandwidth between 5 Hz and 100 Hz (see Figure A.5), however, they limited the measurement at low frequencies due to aliasing in the beat note measurement and pointing issues in the optical set-up.

The big tank (see Figure A.2) had a total mass of approximately 1650 kg. To achieve vibration isolation at low frequencies, the whole tank was mounted on three commercial springs from Mason Industries, Inc.. The spring constant of each of them was K=50 kN/m. The vacuum tank mass was $m = 550$ kg. Thus the resonance frequency is

$$f_{res} = \frac{1}{2\pi}\sqrt{\frac{K}{m}} = 1.52\,\mathrm{Hz}. \tag{A.1}$$

To reach a better attenuation of the vibrations, a second isolation stage was designed. Therefore, a set of four blades with a spring-like behavior where placed inside the vacuum tank holding the telescope spacer mounted on an Aluminum breadboard (see Figure A.2). The design of the blades and its resonance frequency are derived from Reference [71]. In Figure A.2 (right), the telescope in the vacuum chamber is shown. The Aluminum breadboard where the telescope is mounted to, is suspended by four Stainless Steel blades on each corner (see Figure A.3). The blades are mounted to a rigid Aluminum frame holding the liquid nitrogen tank at the top. The blades were made of 3.3 mm thick Stainless Steel and in a triangular shape with a length of 15 cm and a width of 10 cm. Those dimensions were calculated to achieve a resonant frequency $f_{res} = 8\,\mathrm{Hz}$, considering the Young's modulus of E=186 MPa and the weight of the suspended set-up of 50 kg. Underneath the suspension blade a 1 mm thin and 7 cm long secondary blade was installed with a clearance of 5 mm to lower the amplification at the resonance frequency. A Viton O-ring between the two blades was used for damping.

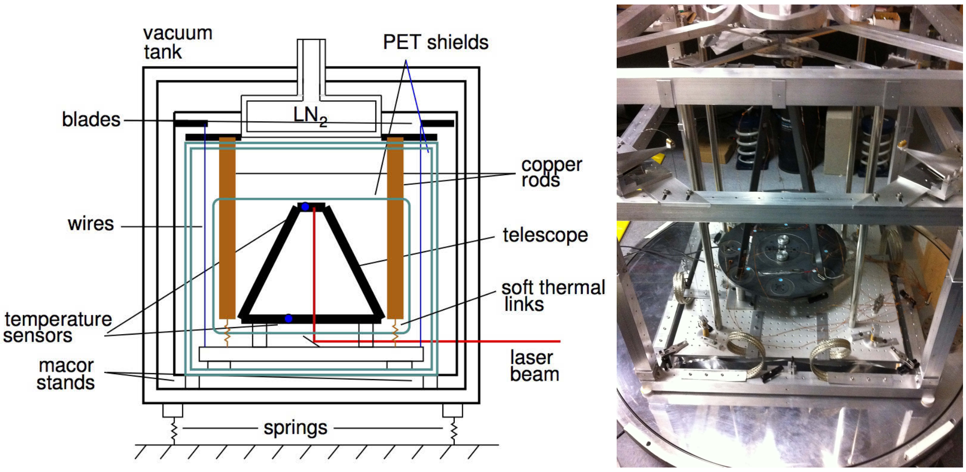

Figure A.2.: Left: Schematic of the mechanical set-up of the SiC telescope test set-up [2]. Right: Photograph of the suspended SiC telescope in the vacuum chamber.

The telescope and the breadboard was hanging on the blades with steel strings with a diameter of 1 mm. At the breadboard, the strings were attached to a 1/2 inch fine thread such that the length of the wire, the distance

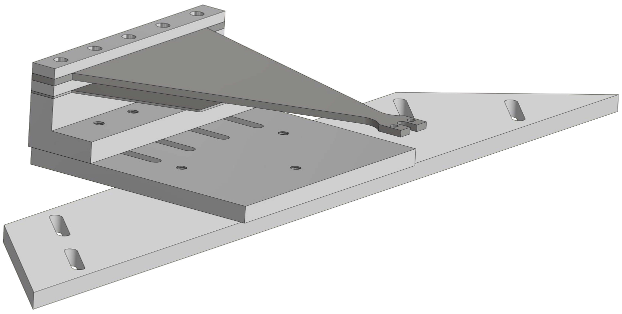

Figure A.3.: CAD model of the suspension blades.

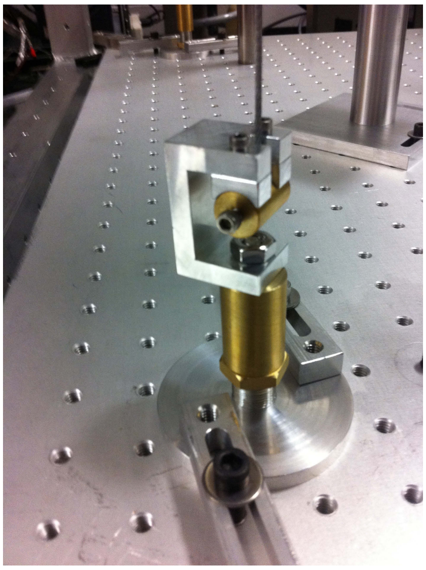

Figure A.4.: Photograph of the leveling part of the telescope suspension.

between the blade and the breadboard could be adjusted (see Figure A.4). The breadboard was also linked to a 25 liter liquid Nitrogen (LN_2) reservoir by means of eight big Copper leads to the telescope in order to cool the telescope to approximately −65°C. The LN_2 tank could be refilled from outside the vacuum tank. Two Polyethylene Terephthalate (PET) sheets were mounted to every side of the Aluminum frame to thermally insulate the set-up from the thermal radiation of the vacuum chamber.

A.3. Results of the suspension system

The ground vibrations where measured by accelerometers mounted on the set-up. In Figure A.5 (left) two time domain measurements are shown: one without vibration isolation (red), and another one with the vibration isolation (black). Figure A.5 (right) shows the corresponding measurements in the frequency domain, where an additional blue trace shows the isolation performance after damping the springs to decrease the resonance peak. The vibration isolation attenuates the ground vibrations noise significantly for frequencies between 5 Hz and 100 Hz as expected. The resonance frequency at about 2 Hz is shifted slightly to a higher frequency due to the damping of the springs.

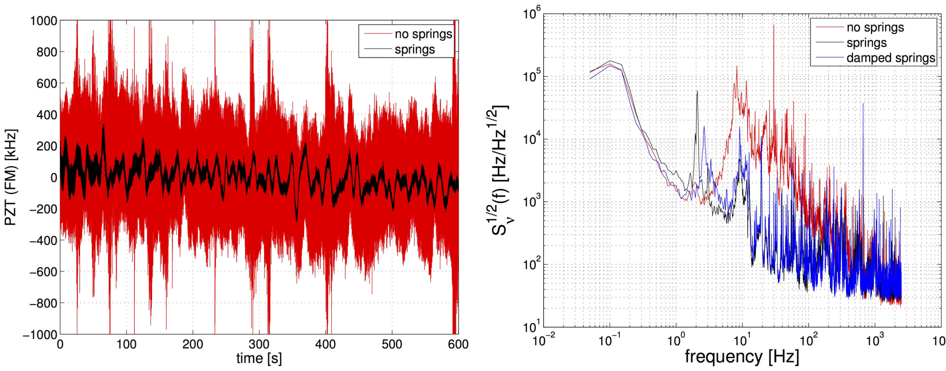

Figure A.5.: Vibrations measured with a PZT sensor at the telescope. Left: in time domain; right: in frequency domain.

A.4. Results of the dimensional stability

The dimensional stability measurements at room temperature were done in a different set-up than for low temperatures. The LN_2 was not needed, the Copper rods were removed, and an additional PET insulation was installed. Such set-up improved significantly the telescope temperature stability. Figure A.6 shows the results of the dimensional stability, $S_X^{1/2}$, at 25°C (left) and at -62°C (right).

At room temperatures (see Figure A.6 left), the measured dimensional stability (red trace) meets the requirement for frequencies higher than 0.5 mHz. At lower frequencies, the dimensional stability follows the temperature fluctuations (green trace), which are converted from δT in [°C], to length values, $\delta\ell$ in [m], as:

$$\delta\ell = \alpha \cdot \ell \cdot \delta T, \tag{A.2}$$

where $\alpha = 2.34 \cdot 10^{-6}\,\mathrm{K}^{-1}$ is the SiC CTE and $\ell = 0.619\,\mathrm{m}$ is the length of the telescope.

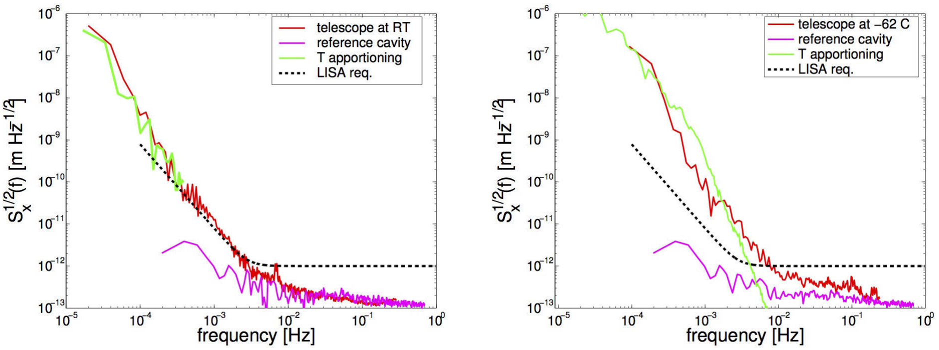

Figure A.6.: Dimensional stability results of the SiC telescope structure at 25°C (left) and at -62°C (right) [2].

The length fluctuations <0.3 mHz are driven by the temperature, both traces follow the same trend. However, for higher frequencies, the length fluctuations might have the same origin but the temperature fluctuations could not be measured due to the noise of the temperature sensor. The magenta trace shows the noise floor of the measurement system, which is the noise level of the reference cavity.

The results at low temperatures (see Figure A.6 right) show that the LISA requirements are met at frequencies higher than 10 mHz. The temperature fluctuations at lower frequencies were too high to meet the requirements.

As a summary of the dimensional stability results, the SiC on-axis telescope structure met the requirements at room temperature for frequencies higher than 0.5 mHz and also at low temperatures ($-60°$C), for frequencies higher than 10 mHz. For both dimensional stability measurements, the temperature stability of the set-up was the limiting factor at lower frequencies. The temperature stability for the LISA mission is about 1000 times better in space than in the laboratories, where the SiC structure should meet the requirements.

B. Frequency references: cavities and Iodine standard

An unequal arm length interferometer is used in our optical set-up to measure the expansion of the sample. This asymmetry introduces noise to the expansion due to laser frequency noise, which can be described by:

$$\delta\ell = \delta\nu \cdot \frac{\Delta\ell}{\nu},$$

where the introduced laser frequency noise $\delta\nu$ is multiplied by the ratio of the difference of the two laser arms ($\Delta\ell$) and the frequency of the laser (ν). To minimize this effect, the laser source has to be very stable. In set-up (**A**), a cavity is used as a frequency reference, and in set-up (**B**) an Iodine cell reference was used. A picometer measurement of a 0.1 m long sample can be achieved by a stabilized laser with a frequency of 281 THz and a frequency noise of 10 kHz.

B.1. Length reference: cavity

An optical cavity consists of two high reflective mirrors, in most cases one flat mirror and one spherical to ensure a stable resonator. A dimensionally stable spacer is used to separate the mirrors and keep the distance as constant as possible. If this distance corresponds to an integer multiple of the laser wavelength, the resonance condition is achieved. To obtain this resonance, a controller is used to change the laser frequency according to the detected error signal. [10]

Two cavities were built up at Airbus DS GmbH in Friedrichshafen in the

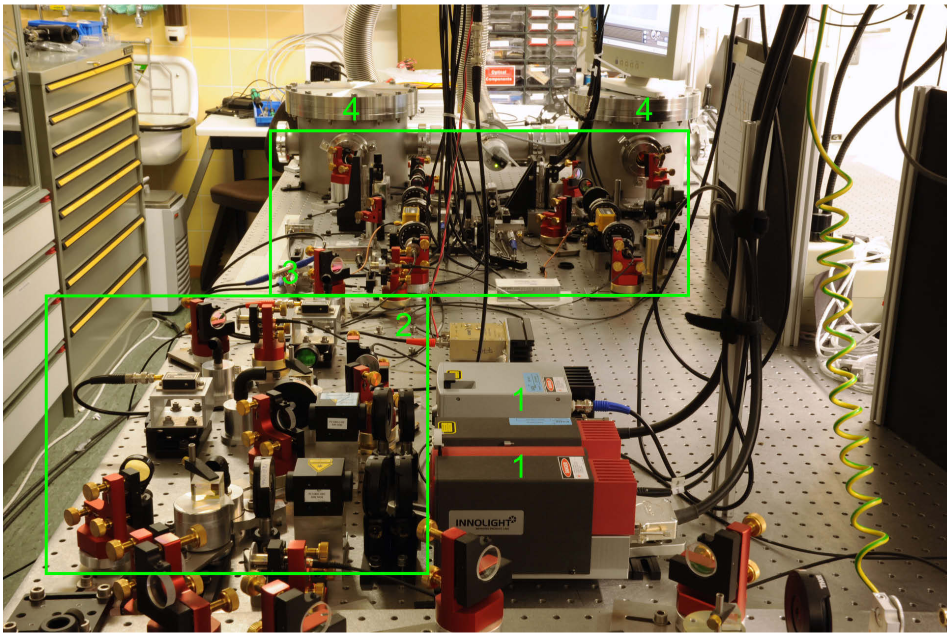

Figure B.1.: Photograph of the cavity set-up [72]. (1) two Nd:YAG laser sources, (2) optical set-up for beam preparation and intensity stabilization, (3) optical set-up for Pound-Drever-Hall locking technique, (4) two vacuum chambers with the optical cavities.

context of the LISA-Mission, to enable high precision optical measurements of interferometers and inertial sensors. A photograph of the experimental set-up is shown in Figure B.1. Therefore two Nd:YAG lasers with a wavelength of 1064 nm were locked to very high finesse ($\mathcal{F} \approx 370000 - 400000$) cavities using the Pound-Drever-Hall technique. [57, 72]

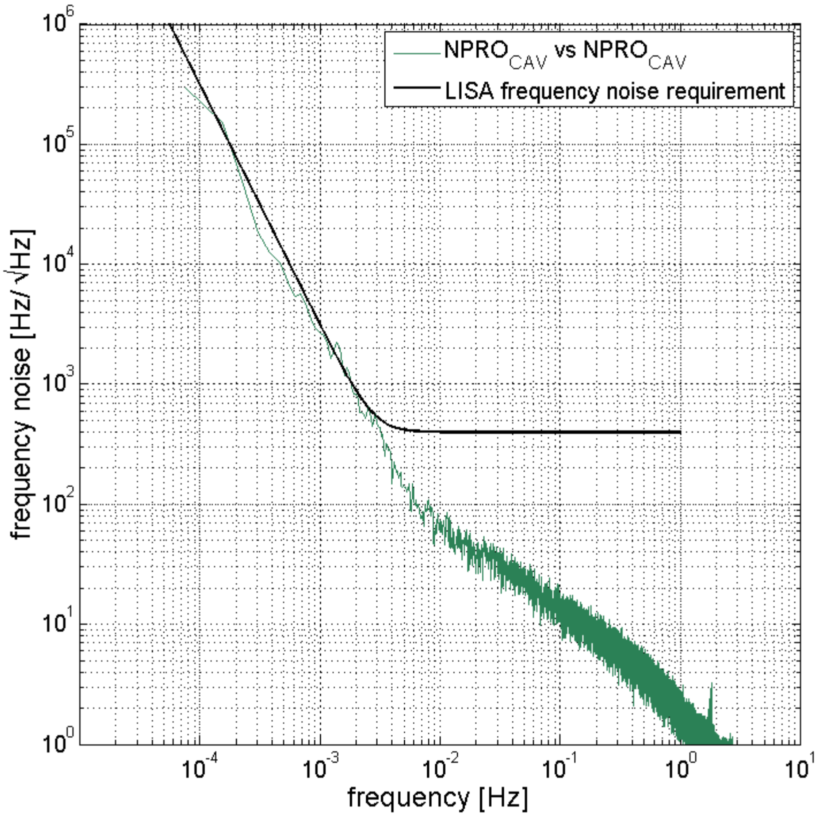

Figure B.2.: LSD of the beat note of two optical resonators and the LISA frequency band [72].

In Figure B.2 a LSD of a beat note of the two stabilized lasers and the LISA frequency band are shown. At frequencies higher than 10^{-2} Hz, frequency noise lower than the $100\,\mathrm{Hz}/\sqrt{\mathrm{Hz}}$ is achieved. At lower frequencies, a $1/f^2$ slope is shown which is most likely dominated by the temperature dependency of the whole system.

B.2. Molecular reference: Iodine standard

In set-up (**B**) for low temperatures an Iodine standard was used as highly stable laser source. The set-up was available but had to be recommissioned. To measure the frequency stability of the Iodine, a second Iodine standard was used to measure a beat note. The second Iodine system (see Figure B.3) was provided by ESA (European Space Agency) and the set-up is described in [73]. Both Iodine set-ups minimize frequency noise by using a 1064 nm Nd:YAG laser (Innolight, Prometheus) with a doubled frequency output of 532 nm stabilized to a hyperfine transition in molecular Iodine using the modulation-transfer-spectroscopy method [74].

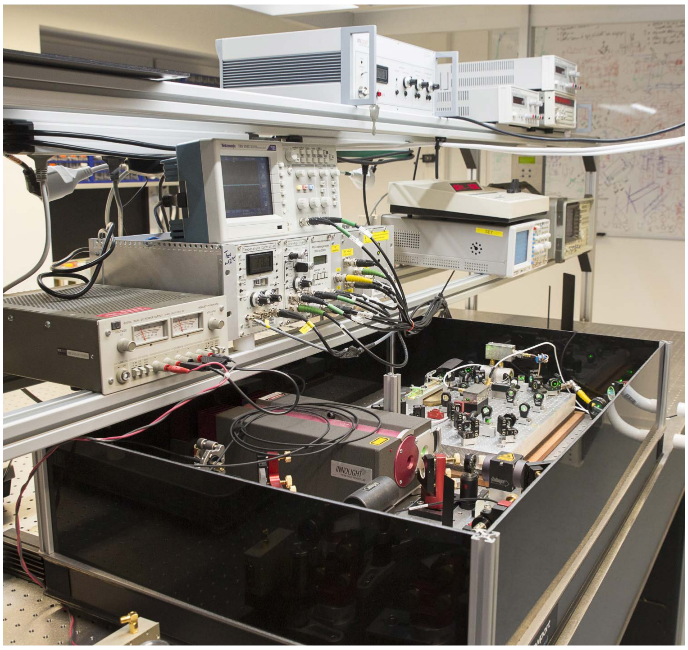

Figure B.3.: Photograph of the Iodine frequency reference.

In Figure B.4 the LSD of the beat note of the two Iodine standards is shown. The blue trace shows the frequency noise of the locked laser systems showing a noise level of $1000\,\mathrm{Hz}/\sqrt{\mathrm{Hz}}$ at frequencies higher than 10^{-2} Hz and the red trace shows the frequency noise of the beat note while the laser systems are free running. With the Iodine reference the noise level of the laser could be reduced four orders of magnitude at lower frequencies.

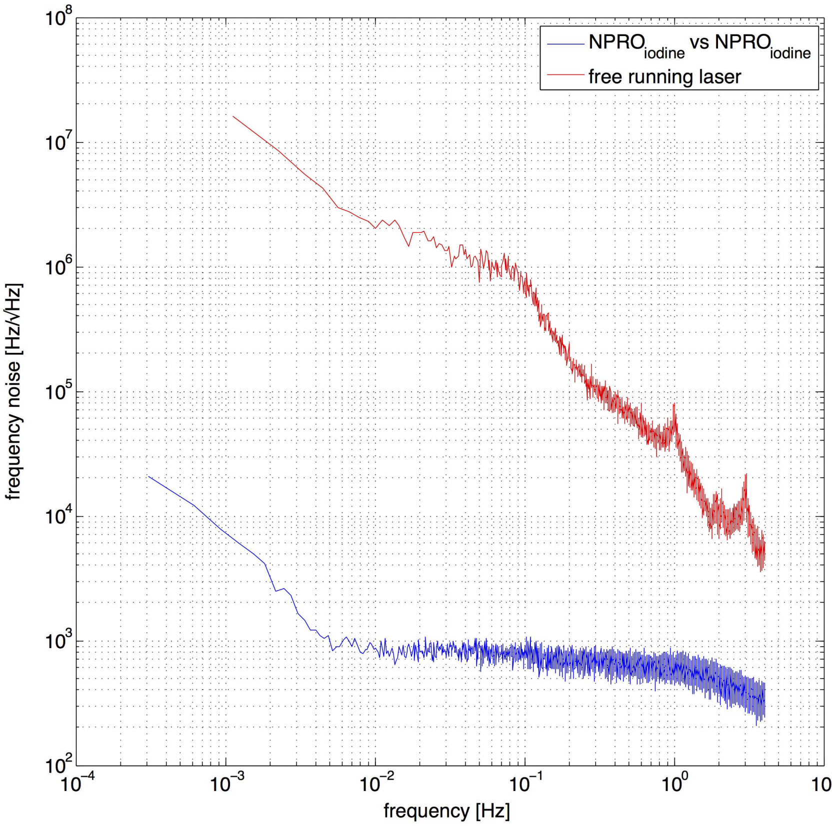

Figure B.4.: LSD of the beat note of two Iodine standards (blue trace) and the free running NPRO laser (red trace).

List of Figures

List of Tables

Bibliography

[1] K. Danzmann, T. A. Prince, P. Binetruy, P. Bender, S. Buchman, J. Centrella, M. Cerdonio, N. Cornish, M. Cruise, C. J. Cutler, et al. "LISA: Unveiling a hidden Universe". In: *Assessment Study Report ESA/SRE* 3 (2011), p. 2.

[2] J. Sanjuán, D. Korytov, G. Mueller, R. Spannagel, C. Braxmaier, A. Preston, and J. Livas. "Note: Silicon carbide telescope dimensional stability for space-based gravitational wave detectors". In: *Review of Scientific Instruments* 83.11, 116107 (2012). DOI: `10.1063/1.4767247`.

[3] A. L. Verlaan, H. Hogenhuis, J. Pijnenburg, M. Lemmen, S. Lucarelli, D. Scheulen, and D. Ende. "LISA telescope assembly optical stability characterization for ESA". In: *Proc. SPIE* 8450 (2012), pp. 845003–845003–7. DOI: `10.1117/12.925112`.

[4] M. Tröbs, L. d'Arcio, S. Barke, J. Bogenstahl, C. Diekmann, E. Fitzsimons, O. Gerberding, J. Hennig, F. Hey, H. Hogenhuis, et al. "LISA Optical Bench Testing". In: *ASP Conf. Ser.* 467 (2013), p. 233.

[5] B. Sheard, G. Heinzel, K. Danzmann, D. Shaddock, W. M. Klipstein, and W. Folkner. "Intersatellite laser ranging instrument for the GRACE follow-on mission". In: *Journal of Geodesy* 86.12 (2012), pp. 1083–1095. ISSN: 1432-1394. DOI: `10.1007/s00190-012-0566-3`.

[6] R. Fleddermann, R. Ward, M. Elliot, D. Wuchenich, F. Gilles, M. Herding, K. Nicklaus, J. Brown, J. Burke, S. Dligatch, D. Farrant, K. Green, J. Seckold, M. Blundell, R. Brister, C. Smith, B. Sheard, G. Heinzel, K. Danzmann, B. Klipstein, D. McClelland, and D. Shaddock. "Testing the GRACE follow-on triple mirror assembly". In: *Classical and Quantum Gravity* 31.19 (2014), p. 195004. DOI: `10.1088/0264-9381/31/19/195004`.

[7] A. Milke, D. Aguilera, N. Gürlebeck, T. Schuldt, S. Herrmann, K. Döringshoff, R. Spannagel, C. Lämmerzahl, A. Peters, B. Biering, H. Dittus, and C. Braxmaier. "A space-based optical Kennedy-Thorndike experiment testing special relativity". In: *Joint European Frequency and Time Forum & International Frequency Control Symposium (EFTF/IFC)*. 2013, pp. 912–914. DOI: `10.1109/EFTF-IFC.2013.6702260`.

[8] J. Sanjuan, N. Gürlebeck, and C. Braxmaier. "Mathematical model of thermal shields for long-term stability optical resonators". In: *Opt. Express* 23.14 (2015), pp. 17892–17908. DOI: `10.1364/OE.23.017892`.

[9] C. Braxmaier, R. Spannagel, T. Schuldt, D. Aguilera, S. Herrmann, C. Lämmerzahl, A. Peters, B. Biering, and H. Dittus. "Satellite test of the special and general relativity theory: a proposal". In: *IAC-13 64th International Astronautical Congress Symposium*. 2013.

[10] S. Webster, M. Oxborrow, S. Pugla, J. Millo, and P. Gill. "Thermal-noise-limited optical cavity". In: *Physical Review A* 77.3 (2008), p. 033847.

[11] S. T. Gulati and M. J. Edwards. "ULE-Zero expansion, low density, and dimensionally stable material for lightweight optical systems". In: *Advanced Materials for Optics and Precision Structures*. Vol. 1. 1997, pp. 107–136.

[12] H. Müller, S. Herrmann, C. Braxmaier, S. Schiller, and A. Peters. "Modern Michelson-Morley experiment using cryogenic optical resonators". In: *Physical review letters* 91.2 (2003), p. 020401.

[13] W. Gorski. *Dilatometrie: Grundlagen und Messverfahren*. Abteilung Wärme: PTB-Bericht. Wirtschaftsverl. NW, Verlag für Neue Wiss., 1996. ISBN: 9783894297510.

[14] J. James, J. Spittle, S. Brown, and R. Evans. "A review of measurement techniques for the thermal expansion coefficient of metals and alloys at elevated temperatures". In: *Measurement Science and Technology* 12.3 (2001), R1.

[15] J. Neumeier, R. Bollinger, G. Timmins, C. Lane, R. Krogstad, and J. Macaluso. "Capacitive-based dilatometer cell constructed of fused quartz for measuring the thermal expansion of solids". In: *Review of Scientific Instruments* 79.3 (2008), p. 033903. DOI: `10.1063/1.2884193`.

[16] T. Schuldt. "An Optical Readout for the LISA Gravitational Reference Sensor". PhD thesis. Humboldt-Universität zu Berlin, 2010.

[17] M. Gohlke. "Ein hochsymmetrisches Heterodyninterferometer zur Demonstration einer optischen Auslesung der Inertialsensoren des weltraumbasierten Gravitationswellendetektors LISA". Diplomarbeit. Humboldt-Universität zu Berlin, 2007.

[18] W. Demtröder. *Laserspektroskopie: Grundlagen und Techniken*. Springer-Verlag, 2007.

[19] E. Morrison, B. J. Meers, D. I. Robertson, and H. Ward. “Automatic alignment of optical interferometers”. In: *Appl. Opt.* 33.22 (1994), pp. 5041–5049.

[20] E. Morrison, B. J. Meers, D. I. Robertson, and H. Ward. “Experimental demonstration of an automatic alignment system for optical interferometers”. In: *Appl. Opt.* 33.22 (1994), pp. 5037–5040.

[21] H. Müller, S.-W. Chiow, Q. Long, C. Vo, and S. Chu. “Active sub-Rayleigh alignment of parallel or antiparallel laser beams”. In: *Opt. Lett.* 30 (2005), pp. 3323–3325.

[22] J. P. Richard. “Cryogenic Fabry-Perot interferometer for time, gravity and material property experiments”. In: *Conference on Precision Electromagnetic Measurements.* 1990, pp. 254–. DOI: `10.1109/CPEM.1990.110012`.

[23] A. McFarlane. “A Fizeau dilatometer for irradiated specimens”. In: *Journal of scientific instruments* 42.1 (1965), p. 24.

[24] R. Schödel, A. Walkov, M. Zenker, G. Bartl, R. Meeß, D. Hagedorn, C. Gaiser, G. Thummes, and S. Heltzel. “A new Ultra Precision Interferometer for absolute length measurements down to cryogenic temperatures”. In: *Measurement Science and Technology* 23.9 (2012), p. 094004. DOI: `10.1088/0957-0233/23/9/094004`.

[25] T. Middelmann, A. Walkov, G. Bartl, and R. Schödel. “Thermal expansion coefficient of single-crystal silicon from 7 K to 293 K”. In: *Phys. Rev. B* 92 (17 2015), p. 174113. DOI: `10.1103/PhysRevB.92.174113`.

[26] M. Okaji, N. Yamada, H. Kato, and K. Nara. “Measurements of linear thermal expansion coefficients of copper SRM 736 and some commercially available coppers in the temperature range 20 - 300 K by means of an absolute interferometric dilatometer”. In: *Cryogenics* 37.5 (1997), pp. 251 –254. ISSN: 0011-2275. DOI: `10.1016/S0011-2275(97)00010-6`.

[27] M. Okaji, N. Yamada, K. Nara, and H. Kato. “Laser interferometric dilatometer at low temperatures: application to fused silica SRM 739”. In: *Cryogenics* 35.12 (1995), pp. 887 –891. ISSN: 0011-2275. DOI: `10.1016/0011-2275(95)96887-R`.

[28] S. Roose and S. Heltzel. *High-precision measurements of thermal expansion at cryogenic temperature on stable materials.* MacroScale 2011 ”Recent developments in traceable dimensional measurements”. 2011.

[29] C. A. Steeves, S. L. d. S. e Lucato, M. He, E. Antinucci, J. W. Hutchinson, and A. G. Evans. "Concepts for structurally robust materials that combine low thermal expansion with high stiffness". In: *Journal of the Mechanics and Physics of Solids* 55.9 (2007), pp. 1803–1822.

[30] F. Bayer-Helms, H. Darnedde, and G. Exner. "Längenstabilität bei Raumtemperatur von Proben der Glaskeramik 'Zerodur'". In: *Metrologia* 21.2 (1985), p. 49.

[31] Schott. "Thermal Expansion of Zerodur". In: *Schott Technical Information publication TIE-37* (2006).

[32] G. L. Harris. *Properties of silicon carbide.* Vol. 13. Iet press, 1995.

[33] A. Preston. "Stability of materials for use in space-based interferometric missions". PhD thesis. University of Florida, 2010.

[34] ECM. *Cesic Material Properties, Type MF.* [2017-03-18]. 2011. URL: `http://www.cesic.de/PDF/Datasheet_Cesic_MF_engl_06_2011.pdf`.

[35] K. Enya, N. Yamada, T. Imai, Y. Tange, H. Kaneda, H. Katayama, M. Kotani, K. Maruyama, M. Naitoh, T. Nakagawa, et al. "High-precision CTE measurement of hybrid C/SiC composite for cryogenic space telescopes". In: *Cryogenics* 52.1 (2012), pp. 86–89.

[36] E. G. Wolff. *Introduction to the dimensional stability of composite materials.* DEStech Publications, Inc, 2004.

[37] H. Schürmann. *Konstruieren mit Faser-Kunststoff-Verbunden.* Springer, 2005.

[38] H. Chen, D. W. Oakes, and E. G. Wolff. "Thermal Expansion of Honeycomb Sandwich Panels". In: *THERMAL CONDUCTIVITY* 25 (2000), pp. 41–48.

[39] W. M. Sokolowski, S. F. Jacobs, M. S. Lane, T. P. O'Donnell, and C. Hsieh. "Dimensional stability of high-purity Invar 36". In: *SPIE's International Symposium on Optics, Imaging, and Instrumentation.* International Society for Optics and Photonics. 1993, pp. 115–126.

[40] P. Hidnert. "Thermal expansion of titanium". In: *Journal of research of the National Bureau of Standards* 30 (1943), pp. 101–105.

[41] H. Philipp. "Optical properties of non-crystalline Si, SiO, SiOx and SiO2". In: *Journal of Physics and Chemistry of Solids* 32.8 (1971), pp. 1935 –1945. ISSN: 0022-3697.

[42] T. Schuldt, M. Gohlke, R. Spannagel, S. Ressel, D. Weise, U. Johann, and C. Braxmaier. “Sub-Nanometer Heterodyne Interferometry and Its Application in Dilatometry and Industrial Metrology”. In: *International Journal of Optomechatronics* 3.3 (2009), pp. 187–200. DOI: `10.1080/15599610903144153`.

[43] C. Wu, S. Lin, and J. Fu. “Heterodyne interferometer with two spatial-separated polarization beams for nanometrology”. In: *Opt. Quantum Electron.* 34.12 (2002), pp. 1267–1276.

[44] C. Wu. “Periodic nonlinearity resulting from ghost reflections in heterodyne interferometry”. In: *Opt. Commun.* 215.13 (2003), pp. 17–23.

[45] G. Heinzel, V. Wand, A. García, O. Jennrich, C. Braxmaier, D. Robertson, K. Middleton, D. Hoyland, A. Rüdiger, R. Schilling, U. Johann, and K. Danzmann. “The LTP interferometer and phasemeter”. In: *Classical and Quantum Gravity* 21.5 (2004), S581. DOI: `10.1088/0264-9381/21/5/029`.

[46] T. Schuldt, M. Gohlke, D. Weise, U. Johann, A. Peters, and C. Braxmaier. “Picometer and nanoradiant optical heterodyne interferometry for translation and tilt metrology of the LISA gravitational reference sensor”. In: *Classical and Quantum Gravity* 26.8 (2009), p. 085008. URL: `10.1088/0264-9381/26/8/085008`.

[47] R. Spannagel, M. Gohlke, T. Schuldt, U. Johann, D. Weise, and C. Braxmaier. “CTE measurement setup with 10 ppb/K sensitivity for characterizing lightweight and highly stable materials for space applications”. In: *Proc. SPIE.* Vol. 8450. 2012, 84500Q–84500Q–7. DOI: `10.1117/12.926061`.

[48] T. Schuldt, M. Gohlke, H. Kögel, R. Spannagel, A. Peters, U. Johann, D. Weise, and C. Braxmaier. “Picometre and nanoradian heterodyne interferometry and its application in dilatometry and surface metrology”. In: *Measurement Science and Technology* 23.5 (2012), p. 054008. DOI: `10.1088/0957-0233/23/5/054008`.

[49] E. Stoppel. “Precision Dilatometry on low CTE Samples”. MA thesis. University of Applied Sciences Konstanz, 2010.

[50] D. Möhrle. “Development and testing of quadrant photo diodes for heterodyne interferometry”. MA thesis. HTWG Konstanz, 2014.

[51] H. Kögel, D. Gerardi, J. Pijnenburg, M. Gohlke, T. Schuldt, U. Johann, C. Braxmaier, and D. Weise. “Interferometric characterization and modeling of pathlength errors resulting from beamwalk across mirror surfaces in LISA”. In: *Applied optics* 52.15 (2013), pp. 3516–3525.

[52] J. Cordero Machado, T. Heinrich, T. Schuldt, M. Gohlke, S. Lucarelli, D. Weise, U. Johann, and C. Braxmaier. “Interferometry based high-precision dilatometry for dimensional characterization of highly stable materials”. In: *Measurement Science and Technology* 20.9 (2009), p. 095301. DOI: `10.1088/0957-0233/20/9/095301`.

[53] R. Spannagel, T. Schuldt, J. Sanjuan, M. Gohlke, R. Burow, E. Fitzsimons, U. Johann, D. Weise, and C. Braxmaier. “Measurement Setup to Determine Thermal Expansions from 100 K to 300 K of Ultra Stable Materials Used in Space Applications”. In: *International Symposium on Optomechatronic Technologies.* 2014, pp. 239–241. DOI: `10.1109/ISOT.2014.64`.

[54] N. Jiang, U. Lindemann, F. Giebeler, and G. Thummes. “A 3 He pulse tube cooler operating down to 1.3 K”. In: *Cryogenics* 44.11 (2004), pp. 809–816.

[55] Lake Shore Cryotronics. *Appendix C: Sensor Packaging and Installation.* [2016-06-13]. 2016. URL: `http://www.lakeshore.com/Documents/LSTC_appendixC_l.pdf`.

[56] R. Spannagel, I. Hamann, J. Sanjuan, T. Schuldt, M. Gohlke, U. Johann, D. Weise, and C. Braxmaier. “Dilatometer setup for low coefficient of thermal expansion materials measurements in the 140 K-250 K temperature range”. In: *Review of Scientific Instruments* 87.10 (2016), p. 103112.

[57] R. Drever, J. L. Hall, F. Kowalski, J. Hough, G. Ford, A. Munley, and H. Ward. “Laser phase and frequency stabilization using an optical resonator”. In: *Applied Physics B* 31.2 (1983), pp. 97–105.

[58] K. P. Birch and P. T. Wilton. “Thermal expansion of Zerodur from 247 to 373 K”. In: *Applied Optics.* 27 (1988), pp. 2813–2814.

[59] R. Spannagel, T. Schuldt, M. Gohlke, J. Delion, U. Johann, D. Weise, and C. Braxmaier. “Optical metrology to determine thermal expansions of ultra stable materials used in space applications”. In: *International Symposium on Optomechatronic Technologies (ISOT).* IEEE. 2012, pp. 1–2.

[60] R. Spannagel, T. Schuldt, M. Gohlke, J. Sanjuan, B. Messerschmidtt, S. Lucarelli, U. Johann, D. Weise, and C. Braxmaier. “Characterizing lightweight and dimensionally ultra stable structures for space applications”. In: *IAC-13 64th International Astronautical Congress Symposium.* 2013.

[61] R. Spero. *Orbiting laser interferometer to measure Earths gravity.* Website. Available online at `http://spie.org/documents/Newsroom/Imported/004321/004321_10.pdf`. Accessed on September 11th 2012. 2012.

[62] K Nicklaus, M Herding, A Baatzsch, M Dehne, C Diekmann, K Voss, F Gilles, B Guenther, B Zender, S Boehme, et al. "OPTICAL BENCH OF THE LASER RANGING INTERFEROMETER ON GRACE FOLLOW-ON". In: *International Conference on Space Optics.* Vol. 7. 2014, p. 10.

[63] TORAYCA. *M60J data sheet.* Website. Available online at `http://www.toraycfa.com/pdfs/M60JDataSheet.pdf`. Accessed on September 9th 2012. 2012.

[64] Suter Kunststoffe AG. *Technische Information EP Epoxidharze S 20 - Sl Reihe.* Website. Available online at `www.swiss-composite.ch/pdf/t-L20-und-Haerter.pdf`. Accessed on September 9th. 2012.

[65] P. Von Böckh and T. Wetzel. *Wärmeübertragung.* Springer, 2013.

[66] K. Danzmann and L. S. Team. "LISA – an ESA cornerstone mission for the detection and observation of gravitational waves". In: *Advances in Space Research* 32.7 (2003), pp. 1233–1242.

[67] O. Jennrich. "LISA technology and instrumentation". In: *Classical and Quantum Gravity* 26.15 (2009), p. 153001.

[68] J. Sanjuan, A. Preston, D. Korytov, A. Spector, A. Freise, G. Dixon, J. Livas, and G. Mueller. "Carbon fiber reinforced polymer dimensional stability investigations for use on the laser interferometer space antenna mission telescope". In: *Review of Scientific Instruments* 82.12 (2011), p. 124501.

[69] S. Lucarelli, D. Scheulen, D. Kemper, R. Sippel, and D. Ende. "The breadboard model of the LISA telescope assembly". In: *Procedings of the International Conference on Space Optics (ICSO).* 2012.

[70] A. D. Spector. "Investigation of the Back-Reflection from an On-Axis Telescope for Space Based Interferometric Gravitational Wave Detectors". PhD thesis. University of Florida, 2015.

[71] B. J. Slagmolen, A. J. Mullavey, J. Miller, D. E. McClelland, and P. Fritschel. "Tip-tilt mirror suspension: Beam steering for advanced laser interferometer gravitational wave observatory sensing and control signals". In: *Review of Scientific Instruments* 82.12, 125108 (2011). DOI: `10.1063/1.3669532`.

[72] G. Holz. “Laser-Frequenzstabilisierung zweier Nd:YAG-Lasersysteme auf optische Hoch-Finesse Resonatoren für die Präzisionsinterferometrie”. MA thesis. HTWG Konstanz, 2011.

[73] T. Schuldt. “Frequenzstabilisierter Nd:YAG-Laser für Weltraumanwendungen”. Diplomarbeit. Universität Hamburg, 2003.

[74] T. Schuldt, J. Stühler, K. Döringshoff, J. Pahl, E. V. Kovalchuk, M. Franz, U. Johann, A. Peters, and C. Braxmaier. “An iodine-based ultra-stable optical frequency reference and its application in fundamental physics space missions”. In: *European Frequency and Time Forum (EFTF), 2014*. 2014, pp. 535–538. DOI: `10.1109/EFTF.2014.7331556`.

List of publications

Journals

R. Spannagel, I. Hamann, J. Sanjuan, T. Schuldt, M. Gohlke, U. Johann, D. Weise, and C. Braxmaier. "Dilatometer setup for low coefficient of thermal expansion materials measurements in the 140K – 250K temperature range", Rev. Sci. Instrum. 87 103112, 2016.

T. Schuldt, M. Gohlke, H. Kögel, R. Spannagel, A. Peters, U. Johann, D. Weise, and C. Braxmaier. "Picometre and nanoradian heterodyne interferometry and its application in dilatometry and surface metrology", Meas. Sci. Technol. 23 054008, 2012.

J. Sanjuan, D. Korytov, G. Mueller, R. Spannagel, C. Braxmaier, A. Preston, and J. Livas. "Note: silicon carbide telescope dimensional stability for space-based gravitational wave detectors", Rev. Sci. Instrum. 83 116107, 2012.

Proceedings

R. Spannagel, T. Schuldt, J. Sanjuan, M. Gohlke, R. Burow, E. Fitzsimons, U. Johann, D. Weise, and C. Braxmaier. "Measurement Setup to Determine Thermal Expansions from 100 K to 300 K of Ultra Stable Materials Used in Space Applications", Proc. of the International Symposium on Optomechtronic Technologies (ISOT), 2014, Seattle, USA.

C. Braxmaier, R. Spannagel, T. Schuldt, D. Aguilera, S. Herrmann, C. Lämmerzahl, A. Peters, B. Biering, and H. Dittus. "Satellite Test of the Special Relativity: a Proposal", 64th International Astronautical Congress Symposium (IAC), 2013, Beijing, China.

R. Spannagel, T. Schuldt, M. Gohlke, J. Sanjuan, B. Messerschmidt, S. Lucarelli, U. Johann, D. Weise, and C. Braxmaier. "Characterizing Lightweight and Dimensionally Ultra Stable Structures for Space Application", 64th International Astronautical Congress Symposium (IAC), 2013, Beijing, China.

A. Milke, D. N. Aguilera, N. Gürlebeck, T. Schuldt, S. Herrmann, K. Döringshoff, R. Spannagel, C. Lämmerzahl, A. Peters, B. Biering, H. Dittus, and C. Braxmaier. "A Space-Based Optical Kennedy-Thorndike Experiment Testing Special Relativity", Proceedings of the Joint UFFC, EFTF and PFM Symposium, 2013, Prague, Czech Republic.

R. Spannagel, J. Delion, M. Gohlke, T. Schuldt, U. Johann, D. Weise, and C. Braxmaier. "Optical Metrology to Determine Thermal Expansions of Ultra Stable Materials Used in Space Applications", Proc. of the International Symposium on Optomechtronic Technologies (ISOT), 2012, Paris, France.

R. Spannagel, M. Gohlke, T. Schuldt, U. Johann, D. Weise, and C. Braxmaier. "CTE measurement setup with 10 ppb/K sensitivity for characterizing lightweight and highly stable materials for space applications", Proc. of SPIE Astronomical Telescopes and Instrumentation, 2012, Amsterdam, Netherlands.

T. Schuldt, M. Gohlke, H. Kögel, R. Spannagel, A. Peters, U. Johann, D. Weise, and C. Braxmaier. "Picometer Interferometry and its Application in Dilatometry and Surface Metrology", The 10th International Symposium of Measurement Technology and Intelligent Instruments, 2011.

Talks and Posters

I. Hamann, R. Spannagel, T. Schuldt, J. Sanjuan, M. Gohlke, U. Johann, D. Weise, and C. Braxmaier. "Dilatometer Setup to Characterize Dimensionally Stable Materials by the Coefficient of Thermal Expansion at a Temperature Range from 100 K to 325 K", DPG-Frühjahrstagung, 2016, Hanover, Germany.

R. Burow, R. Spannagel, T. Schuldt, J. Sanjuan, M. Gohlke, E. Fitzsimons, U. Johann, D. Weise, and C. Braxmaier. "Setup to Measure the Coefficient of Thermal Expansion (CTE) of Ultra Stable Materials at Temperature Range from 100 K to 300 K", DPG-Frühjahrstagung, 2015, Heidelberg, Germany.

J. Sanjuan, R. Spannagel, C. Braxmaier, D. Korytov, G. Mueller, A. Preston, and J. Livas. "Silicon Carbide Telescope Investigations for the LISA Mission", American Astronautical Society (AAS) Meeting, 221st, 2013, Long Beach, USA.

R. Spannagel, M. Gohlke, T. Schuldt, U. Johann, D. Weise, and C. Braxmaier. "Interferometry-Based CTE Measurement Facility with Demonstrated 10 ppb/K Accuracy", DPG-Frühjahrstagung, 2012, Stuttgart, Germany.

T. Schuldt, Martin Gohlke, R. Spannagel, H. Koegel, U. Johann, D. Weise, and C. Braxmaier. "Picometer-interferometry as a key enabling technology for future space missions", 39th COSPAR Scientic Assembly, 2012, Mysore, India.

D. Korytov, J. Sanjuan, G. Mueller, J. Livas, A. Preston, P. Arsenovic, and R. Spannagel. "Telescope Spacer Design Investigations", 78th Annual Meeting of the Southeastern Section of the APS, Volume 56, 2011, Virginia, USA.

A. Cordes, J. Sanjuan, J. Eichholz, A. Spector, J. Livas, A. Preston, P. Arsenovic, S. Mitryk, D. Korytov, R. Spannagel, D. Tanner, J. I. Thorpe, R. Stebbins, and G. Mueller. "Laser stabilization and material studies for the Laser Interferometer Space Antenna (LISA)", AAS Meeting. 2011, Boston, USA.

Supervision

In this thesis are included the results coming from the supervision of the following students:

- Johannes Delion. "High Resolution CTE Determination of a Clearceram Sample by Precision Interferometry", Student Project, University of Applied Sciences Konstanz (HTWG), 2012.
- Johannes Delion. "High Resolution Characterization of Deformations in Ultrastable Compound Structures by Precision Interferometry", Bachelor Thesis, University of Applied Sciences Konstanz (HTWG), 2012.
- Eugen Mikulz. "Konstruktion und Entwicklung der Thermaleinheit eines Dilatometers zur Charakterisierung von dimensional stabilen Werkstoffen im Temperaturbereich von 80K bis 340K im Vakuum", Master Thesis, University of Bremen, 2013.
- Rick Burow. "Design und Aufbau der Heterodynfrequenzerzeugung für ein Laserdilatometer zur Messung der Wärmeausdehnungskoeffizienten hochstabiler Materialien unter kryogenen Temperaturen im Vakuum", Student Project, University of Applied Sciences Bremen, 2014.
- Rick Burow. "Design und Aufbau eines hochsymmetrischen Heterodyn-Interferometers", Bachelor Thesis, University of Applied Sciences Bremen, 2014.
- Fabian Hufgard. "Erläuterungen zum Phasenlock", Student Project, University of Stuttgart, 2015.
- Ines Hamann. "Charakterisierung und Teilsystem-Entwicklung für ein Dilatometer zur Messung von CTEs von hochstabilen Materialien", Master Thesis, University of Applied Sciences Konstanz (HTWG), 2015.